A Statistical Approach to Equivalent Linearization with Application to Performance-Based Engineering

Thesis by

Andrew C. Guyader

In Partial Fulfillment of the Requirements

for the Degree of

Doctor of Philosophy

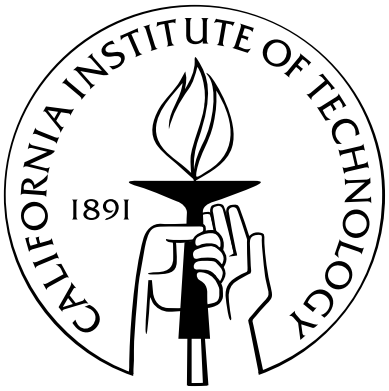

California Institute of Technology

Pasadena, California

2003

(Submitted 9 June 2003)

Acknowledgements

The incredible opportunity to attend Caltech has led me to many different people and events, some outstanding and memorable and others just memorable. I consider myself extremely fortunate to have gotten the opportunity to study at Caltech with such incredibly intelligent and gifted professors and fellow students. My advisor, Prof. Bill Iwan, has helped direct me down the path toward work that advances the design of structures subjected to seismic events. Hopefully, in part through our efforts, buildings will be more safe for occupants during earthquakes. The technical aspects of computer modeling and nonlinear time history analyses could not have been successful without the advisement from Prof. John Hall who is always patient and extremely generous with his time.

Without the support and encouragement of all other graduate students in Thomas over the years, I definitely would not be writing this today. When I arrived at Caltech, two senior level graduate students, Brad Aagaard and Anders Carlson, were extremely generous with their time showing me the ropes of the computer lab and these things called Unix and Matlab. To all the current CE students, the "colorful banter" in the computer lab over the years has been extremely enjoyable. For fear of forgetting someone, I will resist the urge to name all the people but my office mate of six years, John Clinton, has been with me for most everything good and not so good that I have experienced here at Caltech.

I am sure that when my parents, Henri and Susan, drove me off to college eleven years ago, they didn't imagine that eleven straight years of college would ensue. My parents, who have always given me their unconditional love and a warm welcome on visits home, deserve so much credit for giving me the personal resources to even

attempt something like this. This dissertation should have their names on the front cover also.

My brothers, Hank and Robert, who have long since finished college, probably think I stayed in school so I wouldn't have to get a "real job" like them. They might be right but if they want to ask me, they will first have to address me as "Doctor!"

Most of all, my wife of almost exactly five years, Brenda, has constantly supported me throughout the good times and the tough times at Caltech and there have been plenty of both. She has supported me far beyond her fair share. She sacrificed not only where we lived over the first five years of our marriage but how we lived and when we lived. My seemingly endless need for excessively late nights, often working weekends and my distant nature especially over the past 6 months as I feverishly worked to finish this dissertation has been tough. Brenda, you always allowed me to get done what I felt like I needed to get done and for that I am incredibly grateful. We deserve a long vacation together!

Abstract

A new methodology for calculating optimal effective linear parameters for use in predicting the earthquake response of structures is developed. The methodology is applied to several single-degree-of-freedom inelastic structural models subjected to a suite of earthquake acceleration time histories. Separately, far-field and near-field earthquakes are analyzed. Error distributions over a two-dimensional parameter space of period and damping are analyzed through a statistical approach with optimization criterion most applicable to structural design. Four hysteretic models are analyzed: bilinear, stiffness degrading, strength degrading and pinching. Initial structural periods are analyzed in groups for several second slope ratios (α) at different levels of ductility. It was discovered that as ductility increases, the accuracy of the effective parameters decrease but the consequences of bad parameter selection become less severe.

The new effective parameters are intended for use in displacement-based structural analysis procedures as used in Performance-Based Engineering. Of the several procedures available, Nonlinear Static Procedures, such as the Capacity Spectrum Method, are widely used by structural engineers because the nonlinear characteristics of both structural components and the global structure are utilized without running a nonlinear time history analysis. Effective linear parameters are used in the Capacity Spectrum Method to calculate the expected displacement demand, or Performance Point, for a structure. Because several sources of error exist within the Capacity Spectrum Method, an analysis that isolates the error from the effective linear parameters is performed. The new effective linear parameters show considerable improvement over the existing effective linear equations. The existing linear parameters are extremely

unconservative at the lower ductilities and conservative at the higher ductilities. The new parameters lead to a significant improvement in both cases.

A modification to the Capacity Spectrum Method is introduced to account for the new effective linear period. Currently, the Capacity Spectrum Method uses the secant period as the effective linear period. The modification preserves the basic Performance Point calculation. Finally, a new, entirely graphical solution procedure using a Locus of Performance Points provides crucial insight into the effects of strengthening, stiffening and increasing building ductility not available in the current procedure.

Contents

List of Figures

List of Tables

Chapter 1

Background and Motivation

1.1 Introduction

This chapter will develop the equations of motion that will be used throughout the study. Both inelastic and elastic systems will be used in the analysis. Approximate solution techniques estimating the response of inelastic systems by effective linear systems will be introduced. Previous approaches have employed several different methodologies for developing effective linear parameters. Some of these methodologies are briefly summarized.

The methodology proposed in this study (Chapter 2) has been developed in relation to its expected use within current engineering analysis procedures. A background of the current engineering design procedure is presented to explain the context in which the methodology will be applied. This study will improve a widely used analysis procedure by improving the approximate linear analysis employed within the method. The method itself will be modified to allow the use of the new effective linear parameters.

1.2 Single-Degree-Of-Freedom Structural Model

The equation of motion for the single-degree-of-freedom system in Figure 1.1(a) is

$$m\ddot{x} + f(x, \dot{x}) = -m\ddot{u}(t) \tag{1.1}$$

where m is the mass of the system and $f(x, \dot{x})$ is the general restoring force that is a function of both displacement, x, and velocity, $\dot{x}$. The term $f(x, \dot{x})$ can be categorized into two main types: linear or nonlinear.

For a linear system in Figure 1.1(b) the term $f(x, \dot{x})$ may be expressed as

$$f(x, \dot{x}) = kx + c\dot{x} \tag{1.2}$$

where k is the spring stiffness and c is the viscous damper coefficient.

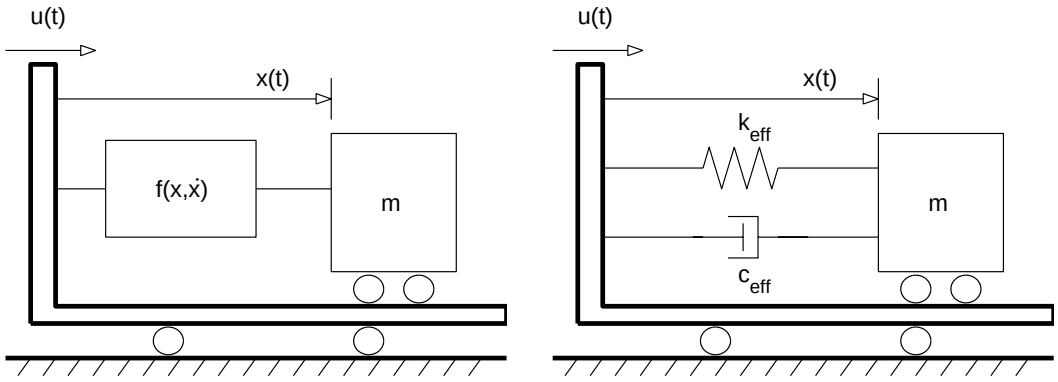

(a) General oscillator (b) Linear oscillator

Figure 1.1: Single-degree-of-freedom structural models

The solution to the linear differential equation of motion for a given base excitation, $\ddot{u}(t)$, can be expressed in a Green's Function approach as

$$x(t) = x_o u_1(t) + \dot{x}_o u_2(t) + \frac{1}{m} \int_0^t \ddot{u}(\tau) h(t - \tau) d\tau \tag{1.3}$$

where x_o and $\dot{x}_o$ are the initial displacement and velocity, respectively, $u_1(t)$ is the displacement response to a unit initial displacement, $u_2(t)$ is the displacement response to a unit initial velocity and $h(t)$ is the unit impulse response function with zero initial conditions. Whether or not Equation 1.3 has an analytical solution is dependent upon the form of the base excitation, $\ddot{u}(t)$. For any base excitation, numerical integration procedures can be used to solve the integral in Equation 1.3.

There are many possible nonlinear forms of $f(x, \dot{x})$. One form is nonlinear elastic

system in which $f(x, \dot{x})$ is an explicit function of displacement and velocity. An example of a nonlinear elastic equation is

$$f(x, \dot{x}) = c\dot{x} + g(x) \text{ where } g(x) = a_1 x + a_3 x^3 \tag{1.4}$$

Another form of nonlinear system is an inelastic system, also known as a hysteretic system. In an inelastic system, $f(x, \dot{x})$ is a *history dependent* function of both the displacement and velocity response. A bilinear hysteretic system is shown in Figure 1.2.

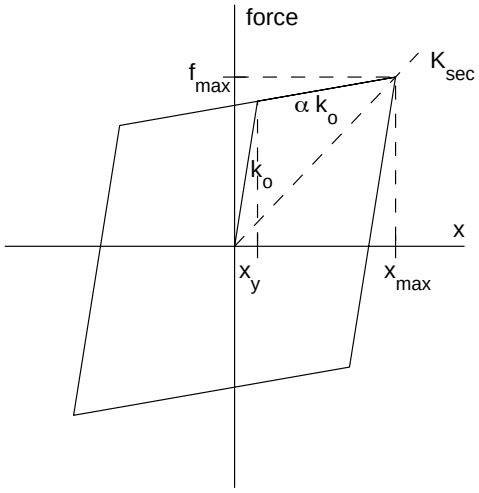

Figure 1.2: Bilinear force versus displacement curve

For many nonlinear systems, obtaining an analytical time history solution to Equation 1.1 will be impossible. Unlike for a linear system, a Green's Function approach will not work because superposition is not applicable to nonlinear systems.

Solutions for nonlinear systems subjected to arbitrary time dependent loading functions are available only by numerical integration procedures. In this study, inelastic systems will be subjected to earthquake acceleration time histories and numerical integration procedures will be the solution approach.

1.3 Approximate Solution Techniques

Approximate analytical methods are essential to analyzing nonlinear single-degree-of-freedom and multi-degree-of-freedom problems. Before computers became readily accessible, approximate techniques were the best option to solving these problems. Today, numerical techniques make almost any nonlinear system solvable. However, just because a system may be solvable numerically, doing so might not be practical for a number of different reasons. For example, a system with a large number of degrees-of-freedom may require an exorbitant amount of time to construct an accurate computer model. Also, the enormous amount of output from such a model may be impractical to analyze. Even for single-degree-of-freedom systems, the number of different loading cases needed to be solved may be too large. This demonstrates that there will always be a need for good approximate methods of analysis for nonlinear systems.

One approximate analysis technique involves replacing the actual nonlinear system with an equivalent linear system. The replacement linear system can then be evaluated either analytically or numerically using Equation 1.3. Conclusions about the characteristics of nonlinear system response may be postulated by analyzing the linear system response. This is generically referred to as equivalent linearization.

The linear parameters obtained through the equivalent linearization analysis have been designated by the subscript *eff*. The replacement differential equation of motion may be expressed as

$$\ddot{x} + 2\zeta_{eff}\omega_{eff}\dot{x} + \omega_{eff}^2 x = -\ddot{u}(t) \tag{1.5}$$

where

$$\omega_{eff} = \sqrt{k_{eff}/m} \tag{1.6}$$

and

$$\zeta_{eff} = c_{eff}/2\sqrt{k_{eff}m} \tag{1.7}$$

The effective period is related to the effective frequency and stiffness by

$$T_{eff} = 2\pi/\omega_{eff} = 2\pi\sqrt{m/k_{eff}} \tag{1.8}$$

1.3.1 Equivalent Linearization Based on Assumed Response

One way to accomplish the equivalent linearization is to analytically minimize the difference between the inelastic restoring force and the elastic restoring force [43]. This can be done by rewriting Equation 1.1 as

$$m\ddot{x} + c_{eff}\dot{x} + k_{eff}x + \varepsilon(x,\dot{x}) = -m\ddot{u}(t) \tag{1.9}$$

where

$$\varepsilon(x,\dot{x}) = f(x,\dot{x}) - c_{eff}\dot{x} - k_{eff}x \tag{1.10}$$

By selecting values for c_{eff} and k_{eff} that minimize the difference term, $\varepsilon(x,\dot{x})$, in Equation 1.10, that term can be ignored in Equation 1.9. The remaining linear equation can be solved using Equation 1.3.

One possible approach to minimizing the difference is to minimize the the mean square error, $\overline{\varepsilon^2}$, with respect to c_{eff} and k_{eff}. This criteria is expressed as

$$\frac{\partial\overline{\varepsilon^2}}{\partial k_{eff}} = 0 \tag{1.11}$$

$$\frac{\partial\overline{\varepsilon^2}}{\partial c_{eff}} = 0 \tag{1.12}$$

If the forcing function, $\ddot{u}(t)$, is a harmonic function of time, the steady-state solution can be assumed to be of the form

$$x(t) = x_{max}cos(\omega t - \phi) = x_{max}cos\theta \tag{1.13}$$

where x_{max} is the maximum displacement amplitude, ω is the response frequency and ϕ is the phase lag. Analyzing a single cycle of the steady-state response leads to the

following equation for the mean square error

$$\overline{\varepsilon^2} = \frac{1}{2\pi}\int_0^{2\pi} (f(x_{max},\theta) - k_{eff}x_{max}cos\theta + c_{eff}\omega x_{max}sin\theta)^2\, d\theta \tag{1.14}$$

Applying the minimization criteria to Equation 1.14 yields

$$c_{eff} = -\frac{1}{x_{max}\omega\pi}\int_0^{2\pi} f(x_{max},\theta)sin\theta\, d\theta \tag{1.15}$$

and

$$k_{eff} = \frac{1}{x_{max}\pi}\int_0^{2\pi} f(x_{max},\theta)cos\theta\, d\theta \tag{1.16}$$

Another way to determine equivalent linear stiffness and damping parameters is through energy balance [19], [38], [43]. The energy dissipated by the hysteretic system is equated to the energy dissipated by an equivalent viscous damper. Assume the response to be of a harmonic form over one full cycle of response expressed as

$$x(t) = x_{max}cos(\omega t - \phi) = x_{max}cos\theta \tag{1.17}$$

Then, energy dissipated by a viscous damper over one cycle of response, E, can be expressed as

$$E = 2\pi^2 c_{eff}x_{max}^2/T \tag{1.18}$$

where T is the period of cyclic motion.

For a bilinear hysteretic model seen in Figure 1.2, the energy dissipated over one cycle of response, E, can be expressed as

$$E = 4x_y(k_o - \alpha k_o)(x_{max} - x_y) \tag{1.19}$$

Equating energies from Equation 1.18 and 1.19 leads to

$$c_{eff} = 2x_y(k_o - \alpha k_o)(x_{max} - x_y)T/(\pi^2 x_{max}^2) \text{ for } x_{max} \geq x_y \tag{1.20}$$

In Figure 1.2 the secant stiffness is labeled K_{sec} and can be expressed as

$$K_{sec} = k_o(x_y + \alpha(x_{max} - x_y))/x_{max} \text{ for } x_{max} \geq x_y \tag{1.21}$$

If the secant period, T_{secant}, is assumed to be the period of structural response, then

$$k_{eff} = K_{sec} \tag{1.22}$$

The secant stiffness can be related to the secant period by Equation 1.8. Substituting Equations 1.8 and 1.21 into Equation 1.20 leads to the following expression for c_{eff}

$$c_{eff} = \frac{4x_y(k_o - \alpha k_o)(x_{max} - x_y)}{\pi x_{max}^2}\sqrt{\frac{m}{K_{sec}}} \text{ for } x_{max} \geq x_y \tag{1.23}$$

1.3.2 Effective Parameter Approach for Determining Earthquake Response of Structures

Researchers have developed various different methods for use in linearizing inelastic systems subjected to earthquake excitation. Most methods use the secant period as the effective linear period.

The response ductility, μ, is defined as the ratio of the maximum displacement response, x_{max}, divided by the yield displacement, x_y, thus

$$\mu = \frac{x_{max}}{x_y} \tag{1.24}$$

The effective parameter equations in this section will be expressed in terms ductility. Also, the second slope ratio, α, will be defined as the ratio of the initial stiffness to the post-yield stiffness as indicated in Figure 1.2.

1.3.2.1 Effective Damping Equations Using the Secant Period

If the secant period is used as the effective linear period as discussed in Section 1.3.1, the ratio of the effective period (T_{eff}) to the initial linear period (T_o) can be expressed

as

$$\frac{T_{eff}}{T_o} = \sqrt{\frac{\mu}{1-\alpha+\alpha\mu}} \tag{1.25}$$

Gulkan and Sozen [28] commented that the secant period equation and c_{eff} from Equation 1.23 when applied to earthquake response prediction, lead to smaller maximum displacement response predictions compared to maximum inelastic earthquake response because of the large damping value. Incorporating shake table results of small-scale reinforced concrete frames and simulation results using the Takeda hysteretic model [65], Gulkan and Sozen developed the following effective damping equation

$$\zeta_{eff} - \zeta_0 \ (\%) = 200(1 - \frac{1}{\sqrt{\mu}}) \tag{1.26}$$

where ζ_o is the nominal fraction of critical damping for the system.

Kowalsky [49], also using the secant period as the effective linear period and the Takeda hysteretic model, developed the following effective damping equation

$$\zeta_{eff} - \zeta_0 \ (\%) = \frac{100}{\pi}(1 - \frac{1-\alpha}{\sqrt{\mu}} - \alpha\sqrt{\mu}) \tag{1.27}$$

The current Capacity Spectrum Method [19], which this study is directed towards improving, uses the secant period as the effective linear period along with the following equation for effective damping coefficient

$$\beta_{eff} \ (\%) = \kappa\beta_0 + 5 \tag{1.28}$$

where β_o is given by

$$\beta_0 \ (\%) = (\frac{200}{\pi})\frac{(\mu-1)(1-\alpha)}{\mu+\mu\alpha(\mu-1)} \tag{1.29}$$

Equation 1.29 is equivalent to Equation 1.23 by using the relationship $c_{eff} = 2\beta_o\omega_{eff}$. Table F.7 contains the values of the factor κ.

1.3.2.2 Two-Dimensional Minimization

In 1980, Iwan [42] proposed a set of effective linear parameters based on the response of hysteretic systems to earthquake excitations. The methodology compared elastic velocity spectra to inelastic velocity spectra. Effective linear parameters were obtained by shifting the inelastic spectra in a manner that minimized the average absolute value difference between the inelastic spectra and the linear spectra over a range of periods. Using the stated procedure, the following relationships were obtained for the effective linear parameters

$$\frac{T_{eff}}{T_o} = 0.121(\mu - 1)^{0.939} + 1 \tag{1.30}$$

$$\zeta_{eff} - \zeta_o \ (\%) = 5.87(\mu - 1)^{0.371} \tag{1.31}$$

A summary of the effective linear parameters discussed above is shown in Figure 1.3.

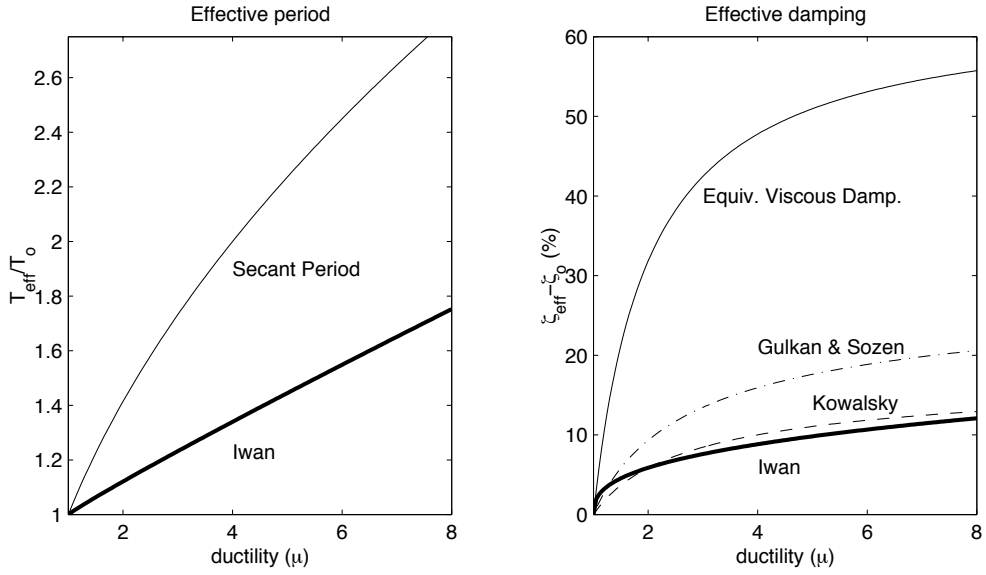

Figure 1.3: Summary of effective linear parameters from previous methodologies

1.4 Performance-Based Engineering

Very little interest was taken in earthquake resistant building design until after the 1933 Long Beach earthquake. After that particular urban event, building codes began to be developed that required provisions on a lateral force analysis for new structures. These codes have evolved over the years but their main focus has never change - preserve human life in a structure by preventing structural collapse. Very little consideration has been given to other possible consequences of earthquakes on structures. Recently, as building design and construction procedures have improved, the desire to predict the amount of expected damage from a seismic event has emerged. Performance-Based Engineering (PBE) has been developed to predict intermediate levels of building damage.

Consequences of earthquakes on buildings can be divided into three main categories: life safety, capital losses and functional losses [2]. Life safety deals with deaths and injuries to both building occupants and passersby. Capital losses are the costs associated with repairing damage to buildings or its contents. Functional losses are losses of revenue or increased operating expenses after an earthquake. Performance-Based Engineering attempts to take into account life safety, capital losses and functional losses by defining Building Performance Levels that are directly related to these three issues. Building Performance Levels combine both structural performance and non-structural performance. A building component is considered structural if it is load bearing or part of the lateral load resisting system. Non-structural components are anything that is not structural.

There are four main Building Performance Levels. Each level is composed of different structural and non-structral performances. The levels are:

- Operational Performance Level - There is limited structural damage. The structure is practically identical to the pre-earthquake state and occupation of the building is not interrupted. Non-structural elements are generally in place and functional. Minor disruptions may occur and some cleanup may be warranted.

- Immediate Occupancy Performance Level - There is limited structural damage,

as in the Operational level. However, non-structural items are generally in place but may have experienced damage.

- Life Safety Performance Level - Significant structural damage may have occured but some margin exists before total or partial structural collapse. Typically, major structural components are damaged and extensive repairs will have to be made. The building is unsafe to occupy after the seismic event. Significant non-structural damage may have occured but no collapse or falling of heavy items occured.

- Structural Stability Performance Level - The structure is on the verge of experiencing partial or total collapse but the vertical load carrying capacity of the structure remains. Non-structural damage is not addressed in this performance level.

The demand placed on a structure at a particular site can come from several sources. The earthquake ground motion demand is defined as the engineering characteristic of the shaking at a site for a given earthquake that has a certain probability of occuring [2]. This demand is generally broken into three categories:

- Serviceability Earthquake - The ground motion with a 50% chance of being exceeded in a 50-year period.

- Design Earthquake - The ground motion with a 10% chance of being exceeded in a 50-year period.

- Maximum Earthquake - Maximum level of ground motion expected within the known geologic framework due to a specified single event (median attenuation), or the ground motion with a 5% chance of being exceeded in a 50-year period.

The representation of earthquake demand will be discussed in section 1.4.2.3. Wind and tsunamis are non-ground motion demands which are not relevant to this study but still exist and must be properly accounted for.

1.4.1 Performance Objectives

A Performance Objective is the Building Performance Level for a specific level of Seismic Demand. The Performance Objectives are all possible combinations of building performance and seismic demand as presented in Table 1.1. There can be a single Performance Objective or multiple Performance Objectives, one for different Seismic Demands. Performance Objectives may be assigned dependent upon the function of the building, life expectancy of the structure, historical preservation issues, cost considerations and other conditions or constraints. More stringent Performance Objectives will typically result in higher costs. Choosing an Operational Building Performance Level for the Maximum Earthquake demand will cost more than the Life Safety Level for the Design Earthquake demand. The decision on the final Performance Objective must take all these factors into account.

Seismic Demand	Building Performance Level			
	Operational	Immediate Occupancy	Life Safety	Structural Stability
Servicibility EQ				
Design EQ				
Maximum EQ				

Table 1.1: Performance Objectives for Performance-Based Engineering combine a Building Performance Level with a Seismic Demand

1.4.2 Analysis Techniques

A number of guidelines for the analysis techniques required for determining the building performance levels are contained in such documents as Applied Technology Council-40 (ATC-40), *Seismic Evaluation and Retrofit of Concrete Buildings* and Federal Emergency Management Agency (FEMA) 273, *NEHRP Guidelines for the Seismic Rehabilitation of Buildings*. The documents contain both linear and nonlinear analysis procedures. Currently, four types of procedures are available for building analysis. They include the Linear Static Procedure (LSP), Linear Dynamic Procedure (LDP), Nonlinear Static Procedure (NSP) and Nonlinear Dynamic Procedure (NDP).

Each procedure will now be briefly summarized and further details are available in FEMA 273.

- Linear Static Procedure - The building is modeled with all elements as linearly-elastic. Displacements are calculated from a pseudo-static lateral load analysis and are intended to represent the inelastic displacement demand that is expected from the Design Earthquake. It may be shown that the internal forces calculated will equal or exceed those values expected during the building response to the Design Earthquake.

- Linear Dynamic Procedure - The building is modeled with all elements as linearly-elastic. Displacements are calculated from either a time history analysis or a modal spectral analysis and are intended to represent the inelastic displacement demand that is expected from the Design Earthquake. For time-history analysis, a suite of at least three ground motions must be used to account for the variability of different ground motions. Modal spectral analysis is the summation of expected modal responses using displacements from a response spectrum (Section 1.4.2.3) at the periods of the lower modes of the structure.

- Nonlinear Static Procedure - The building is modeled with the expected nonlinear characteristics of the individual elements. An incrementally increasing lateral load profile simulates the expected inertial forces experienced during the seismic demand (Section 1.4.2.2). This results in a push-over curve which represents the structural capacity of the building. Earthquake demand is represented by a response spectrum (Section 1.4.2.3). Displacement demand is calculated by either determining the Performance Point, as in the Capacity Spectrum Method (Section F.1), or modifying the elastic response to determine the Target Displacement, as in the Coefficient Method (Section F.2).

- Nonlinear Dynamic Procedure - The building is modeled with the expected nonlinear characteristics of the individual elements. Displacements are determined using nonlinear time history analysis. It is suggested, but not required, to use

more than one ground motion. Nonlinear response can be highly sensitive to the ground motion characteristics so it would be wise to use a suite of ground motions in the analysis.

1.4.2.1 Nonlinear Static Procedures

Nonlinear Static Procedures have become very popular for Performance-Based Engineering analysis. The appeal to structural engineers is that without the running of nonlinear time history analyses, displacement demands can be calculated which directly take into account the approximate nonlinear load-deformation characteristics of the structural elements and the entire structure. Nonlinear time history analyses can often be difficult to execute and interpret.

Nonlinear Static Procedures combine structural capacity, determined from a push-over analysis (Section 1.4.2.2), with seismic demand, represented as a response spectrum (Section 1.4.2.3), in order to predict building response to earthquakes. Lateral deformation values on the push-over curve can be associated with specific Building Performance Levels. As commented in ATC-40 [19]: *The process of defining lateral deformation points on the capacity curve at which specific Building Performance Levels may be said to have occurred requires the exercise of considerable judgment on the part of the engineer.* Figure 1.4 shows a push-over curve with displacements associated with different Building Performance Levels.

The seismic demand experienced by a structure is represented by an Acceleration-Displacement Response Spectrum (ADRS). Through a type of modal conversion (Equations 5.1 and 5.2), the push-over curve is transformed into the capacity spectrum changing from units of force and displacement to spectral acceleration and spectral displacement. The capacity curve and seismic demand may now be drawn on the same axes. For the *Coefficient Method*, only a 5% damped response spectrum is required. The linear displacement response of the structure is modified by a series of coefficients accounting for hysteretic shape, inelastic amplification and other dynamic features.

The *Capacity Spectrum Method* is relatively intuitive in nature. The Capacity

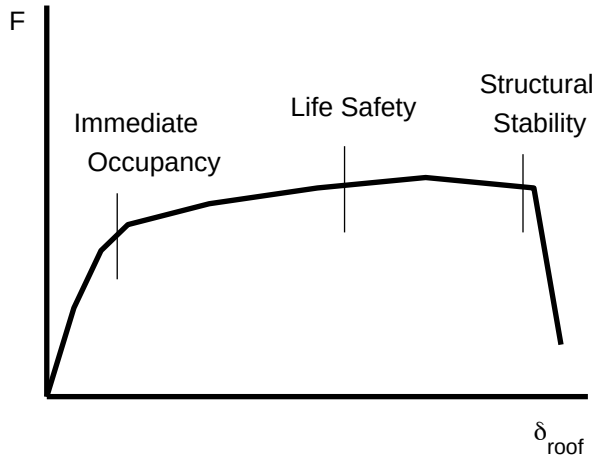

Figure 1.4: Building Performance Levels as determined for a capacity curve

Spectrum Method requires the representation of inelastic seismic demand by using response spectra with varying amounts of damping. Inelastic response is characterized by ductility (Equation 1.24). Effective linear parameter equations are used in the Capacity Spectrum Method to assign damping for different levels of ductility. When the demand and capacity ductilities are equal, the system is in a type of dynamic equilibrium. The equilibrium point defines the expected performance of the structure, referred to as the *Performance Point*. As seen in Figure 1.5, the intersection of the demand and capacity will be the Performance Point for the structure.

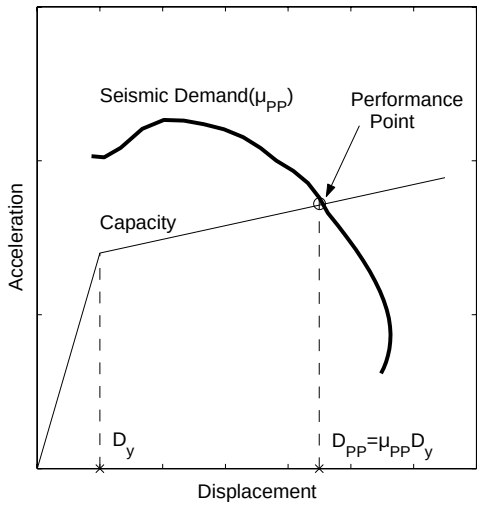

Figure 1.5: Performance Point calculation in the Capacity Spectrum Method

This study will focus on improvement of the Capacity Spectrum Method. This will be accomplished by improving the effective linear parameters used in the solution procedure. Motivation came from a preliminary study by Iwan and Guyader [46] that used the effective linear parameters developed by the 1980 Iwan study in place of the current Capacity Spectrum Method effective linear equations (Section 1.3). The displacement predictions using the Iwan equations showed a considerable improvement over the current Capacity Spectrum Method equations. Using an effective period not equal to the secant period was an important factor in this improvement.

1.4.2.2 Representing Structural Capacity: Push-over Analysis

Nonlinear static procedures use a push-over analysis to develop a representation of structural capacity. The ability to perform a nonlinear static analysis must meet the first fundamental requirement that *extensive* knowledge must be available about the structure, components, connections and material properties. If this information is unattainable, nonlinear static procedures must not be used to analyze the building.

With this knowledge of the building, an accurate computer model of the building can be constructed. The model must take into account the expected load-deformation characteristics of the components and connections. The load-deformation behavior of the components and connections are adopted from cyclic laboratory testing. The cyclic tests create hysteretic response loops from which a backbone curve is constructed. The backbone curve is the locus of turn around points from the cyclic test data.

A horizontal load profile must be developed to deform the building model. The load profile represents the expected inertial forces experienced in the structure during an earthquake. Usually, the response of structures to far-field, random-like ground motions is a resonance build-up in the fundamental mode. Therefore, a sensible choice for the load profile is the first-mode shape. However, the response of the structure is highly dependent upon the characteristics of the ground motion.

Push-over analysis should not be performed on structures in which the probable inertial forces from the earthquake cannot be accurately represented. If higher modes

of response are significant, a first-mode push-over profile would not be accurate. Methods have been developed that attempt to use higher-mode load profiles to deform building models [17], [33], [63]. Currently, guidelines for these methods are being formulated for use in forthcoming design guidelines [20].

A case where the probable earthquake inertial forces would be misrepresented by a first-mode profile is when the ground motion has a pulse-like character. The response of the building in this case would not be of a resonance build-up but instead a localized collection of damage from the sudden large ground displacement pulse [7], [11], [12], [34], [36], [47]. For these ground motions, the load profile to represent earthquake inertial forces would need to be drastically different from any of those currently proposed for analysis.

The horizontal load is applied in an incremental fashion and the sum of the lateral force versus roof displacement is recorded at various levels of load. Figure 1.6 shows an example of a push-over analysis using a triangular load profile.

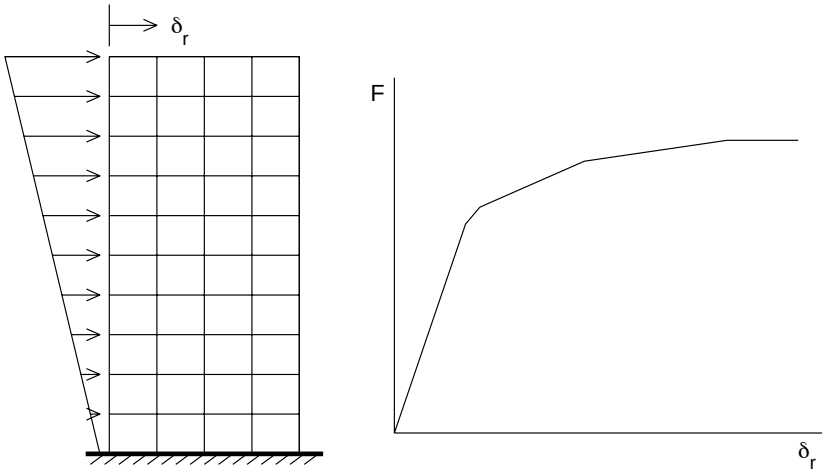

Figure 1.6: Push-over load profile used to deform a building model and the resulting capacity curve

The push-over results are dependent upon such factors as the load profile used, the detail of the computer model, the solution algorithm of the software and the ability of the software to account for P-$\triangle$ effects [31], [35], [66]. P-$\triangle$ is a geometric nonlinearity in structures generated by gravity forces due to the displaced configura-

tion. An inverted pendulum with a rotation spring is an example of such a geometric nonlinearity. The differential equation of motion is of the form

$$I\ddot{\theta} + K\theta - mgh\ sin\theta = M(t) \tag{1.32}$$

where K is the stiffness of the rotational spring and m is the mass of the pendulum at a height h above point of rotation in the vertical configuration ($\theta = 0$). For the linearized case, the effective spring stiffness is $K - mgh$, thereby increasing the rotational deflection of the system as compared to the case when gravity is assumed to be "turned off" (i.e., gravity is equal to zero). Gravity forces *must* be included in the push-over analysis to accurately represent the building response at all displacement levels.

For the simple single-degree-of-freedom inverted pendulum, the inclusion of the effects of gravity is relatively straight forward, especially in the static case. The inclusion of gravity forces in structural analysis is not as straight forward. Iterative techniques may be used to solve for equilibrium in the displaced configuration which accounts for P-$\triangle$ effects. The other nonlinearities that must be taken into account are the decrease of rotational strength as axial force increases and the possibility of buckling in axial force members. However, software codes that take all these factors into account can be cost prohibitive.

The push-over curve is now a structural surrogate for the actual multi-degree-of-freedom building model. The push-over will be the sole representation of the building for the remainder of the analysis. It *must* be as accurate as possible. The push-over curve represents the backbone of cyclic structural response. From the push-over curve the value of the initial elastic period can be determined as well as an approximate value for the second slope ratio, α.

The building must also be categorized as a certain hysteretic model type. The backbone of cyclic response still leaves the question as to how the building will respond during the cycles of response. The hysteretic shape may be bilinear for all cycles of response or there may be stiffness degradation. Another option is pinching

hysteretic response as may be found in concrete structures. Categorizing the model as a certain hysteretic type is left up to the discretion of the engineer and often requires considerable "engineering judgment". Categorizing the model is further discussed in Section 3.1.

1.4.2.3 Representing Seismic Demand: Response Spectra

Within the Capacity Spectrum Method, seismic demand is represented as response spectra in acceleration versus displacement format. This is commonly referred to as Acceleration-Displacement Response Spectra (ADRS). An example of the ADRS format is shown in Figure 1.7. A nominal amount of viscous damping, ζ_o, may be assumed for every building. Normal viscous damping ranges from 2% to 10%, assuming no supplemental damping devices or base isolation is present. The nominal viscous damped response spectrum is the Design Spectrum which represents the linear response case. The seismic demand must be represented as a function of ductility for application in the Capacity Spectrum Method. Through the effective linear parameters, damping is a function of ductility. Generally, higher levels of ductility are represented by higher levels of damping. This study will produce new effective linear equations which will substantially increase the accuracy of the demand representation. The increased accuracy of the demand will increase the overall accuracy of the displacement prediction in the Capacity Spectrum Method.

Recall Equation 1.5. The Spectral Acceleration (SA) is defined as the maximum absolute acceleration of a single-degree-of-freedom oscillator from an acceleration time history analysis. This may be expressed as

$$\text{Spectral Acceleration (SA)} = \max \forall t |\ddot{x}(t) + \ddot{u}(t)| \tag{1.33}$$

Spectral Acceleration may also be expressed in terms of the displacement and velocity response. Combining Equations 1.5 and 1.33 leads to

$$\text{SA} = \max \forall t |2\zeta_{eff}\omega_{eff}\dot{x}(t) + \omega_{eff}^2 x(t)| \tag{1.34}$$

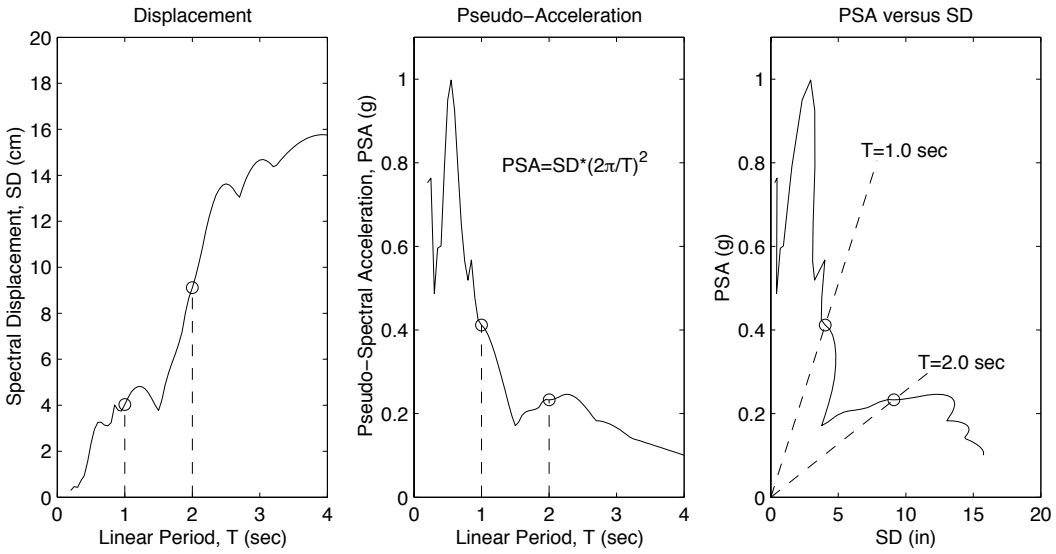

Figure 1.7: Spectral Displacement (SD) and Pseudo-Spectral Acceleration (PSA) combined in an Acceleration-Displacement Response Spectra (ADRS)

The Spectral Displacement (SD) is defined as the maximum relative displacement of a linear single-degree-of-freedom oscillator for an acceleration time history analysis. This may be expressed as

$$\text{Spectral Displacement(SD)} = \max \forall t|x(t)| \tag{1.35}$$

Over a range of natural frequencies, ω_{eff}, for a constant value of damping, ζ_{eff}, combinations of Spectral Displacement and Spectral Acceleration can be computed from time history analyses. Plotting these combinations with displacement on the horizontal axis and acceleration on the vertical axis and connecting them for sequential ω_{eff} values will form a curve. This curve is the Acceleration-Displacement Response Spectrum.

The Pseudo-Spectral Acceleration (PSA) is defined as the Spectral Displacement times the natural frequency squared

$$\text{Pseudo-Spectral Acceleration (PSA)} = \text{SD}\omega_{eff}^2 \tag{1.36}$$

Comparing Equations 1.34 and 1.36, it is seen that SA = PSA when $\zeta = 0$ and SA $\geq$ PSA when $\zeta > 0$.

A radial line on the Acceleration-Displacement Response Spectrum has units of inverse frequency squared ($1/\omega_{eff}^2$). Using Equation 1.8, the period value associated with a radial line is related to the slope of the line by

$$T = \frac{2\pi}{\sqrt{\text{slope}}} \tag{1.37}$$

For plots of SA versus SD, Equation 1.37 may be expressed as

$$T = 2\pi\sqrt{\frac{\max\ \forall t|x(t)|}{\max\ \forall t|2\zeta_{eff}\omega_{eff}\dot{x}(t) + \omega_{eff}^2 x(t)|}} \tag{1.38}$$

For plots of PSA versus SD, Equation 1.37 may be expressed as

$$T = 2\pi\sqrt{\frac{\max\ \forall t|x(t)|}{\omega_{eff}^2 \max\ \forall t|x(t)|}} = 2\pi\sqrt{\frac{1}{\omega_{eff}^2}} = T_{eff} \tag{1.39}$$

Therefore, on a plot of PSA versus SD, a radial line represents a constant value of structural period for all values of damping. On plots of SA versus SD, this is not guaranteed to be true.

For the Capacity Spectrum Method, it is *necessary* that radial lines on the ADRS represent constant structural periods for a wide range of damping values. Therefore, seismic demand must be plotted as PSA versus SD.

Chapter 2

Methodology

2.1 Equations of Motion

Recall the equation of motion for the single-degree-of-freedom system in Figure 1.1 (Equation 1.1). When $f(x, \dot{x})$ represents a linear viscous damped system, the differential equation of motion may be expressed as

$$m\ddot{x}_{lin} + c_{eff}\dot{x}_{lin} + k_{eff}x_{lin} = -m\ddot{u}(t) \tag{2.1}$$

Where c_{eff} and k_{eff} are the viscous damping coefficient and spring stiffness, respectively. For a given ground excitation, $\ddot{u}(t)$, the solution, $x_{lin}(t)$, may be computed using a numerical solution procedure. For an inelastic system, the restoring force, $f(x, \dot{x})$, may take a variety of forms as discussed in Section 1.2. The solution for the inelastic system will be designated as $x_{inel}(t)$.

Many different approaches are available for making a comparison between the displacement time histories $x_{inel}(t)$ and $x_{lin}(t)$. These include, but are not limited to, a point by point comparison of the displacement, velocity or acceleration time histories, comparing the number of zero displacement crossing or comparison of the amplitude spectra from a Fourier Transform. However, to quantify a comparison, there must be a value assigned to the amount of similarity or difference. Within the framework of Performance-Based Engineering, the key performance variable is the maximum relative displacement amplitude that a structure experiences from the

demand earthquake. The relative displacement for the inelastic and linear single-degree-of-freedom systems is $x_{inel}(t)$ and $x_{lin}(t)$, respectively.

The effective linear parameters obtained based on a comparison of displacement values would not be appropriate to be used in a velocity or force-based design procedure. For example, the maximum velocities or accelerations from the linear solution should not be used as estimates for the maximum values of $\dot{x}_{inel}(t)$ or $\ddot{x}_{inel}(t)$. The maximum acceleration or maximum pseudo-acceleration would be a much better comparison parameter for effective linear parameters intended for use in a force-based approach.

The maximum displacement amplitude of the nonlinear time history $x_{inel}(t)$ will be designated as D_{inel} and the maximum displacement amplitude of the linear time history $x_{lin}(t)$ will be designated as D_{lin}. Previous methodologies for developing effective linear parameters are discussed in Section 1.3. Many approaches are based either on the assumption of a steady-state harmonic response or have employed empirical methods based on the earthquake response of both computer models and shake table models. The effective linear parameters developed in this study will be used for estimating the response of structures subjected to earthquake excitations. Therefore, using real earthquake time histories as the model inputs is most logical.

The methodology developed in this study employs a search over a two-dimensional parameter space related to the linear system coefficients c_{eff} and k_{eff} in Equation 2.1. One can expect to find a combination or combinations of c_{eff} and k_{eff} that have the best maximum displacement match with an inelastic system, in some sense. The terms c_{eff} and k_{eff} will be replaced by the fraction of critical damping, ζ_{eff}, and the natural period of oscillation, T_{eff}. Using Equations 1.6 through 1.8, Equation 2.1 can be expressed as

$$\ddot{x} + \frac{4\pi\zeta_{eff}}{T_{eff}}\dot{x} + (\frac{2\pi}{T_{eff}})^2 x = -\ddot{u}(t) \tag{2.2}$$

The system parameters ζ_{eff} and T_{eff} completely describe the linear single-degree-of-freedom system.

2.2 Error Measure

In order to compare the maximum displacements, D_{inel} and D_{lin}, an error measure will be defined. In engineering design, unconservative displacement predictions may be less desirable than conservative predictions. Therefore, a fundamental requirement of any error measure is that it distinguish between a conservative displacement prediction and a non-conservative displacement prediction. An error measure that uses an absolute value of the difference between D_{inel} and D_{lin} would not satisfy this requirement.

A simple error measure satisfying the above requirement is the ratio of the difference between the linear system maximum displacement, D_{lin}, and the inelastic system maximum displacement, D_{inel}, to the inelastic system maximum displacement.

$$\epsilon_D = \frac{D_{lin} - D_{inel}}{D_{inel}} \tag{2.3}$$

Then, a negative value of ϵ_D reflects an unconservative displacement prediction while a positive value reflects a conservative displacement prediction. ϵ_D might be considered to have a positive bias as it ranges from -1 to ∞. However, for the range of systems and excitations considered in this study, the slight positive bias in the statistical distribution of ϵ_D is inconsequential.

For a given inelastic system and ground excitation, there will be a certain topology of error, ϵ_D, as a function of linear system parameters T_{eff} and ζ_{eff} as shown in Figure 2.1. Note that there exists a nearly diagonal contour of zero error. For any combination of T_{eff} and ζ_{eff} lying along this contour there will be a perfect match between D_{lin} and D_{inel}. For any specified ensemble of inelastic systems and ground excitations, distributions of ϵ_D can be obtained for every combination of T_{eff} and ζ_{eff}. This is illustrated in Figure 2.2.

Sample distributions of ϵ_D at certain locations in the T_{eff}, ζ_{eff} parameter space are shown in Figures 2.3 through 2.5. The locations selected are in close proximity to the optimal values of T_{eff} and ζ_{eff} which will be defined later. Figure 2.3 shows

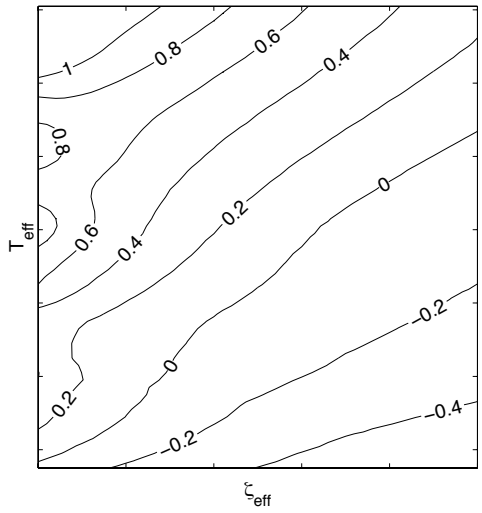

Figure 2.1: Contour values of ϵ_D over the two-dimensional parameter space of T_{eff} and ζ_{eff} for a single combination of inelastic system and ground excitation

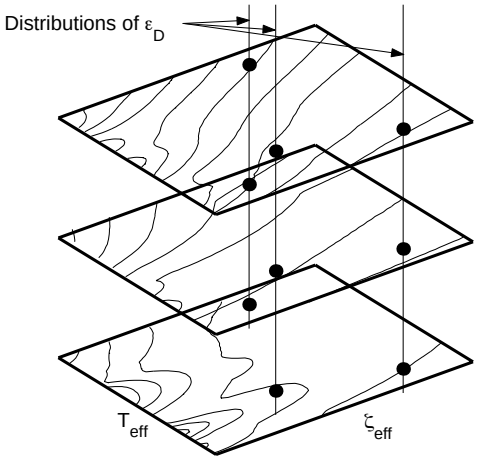

Figure 2.2: Illustration of assembling ϵ_D error distributions at every combination of T_{eff} and ζ_{eff} over an ensemble

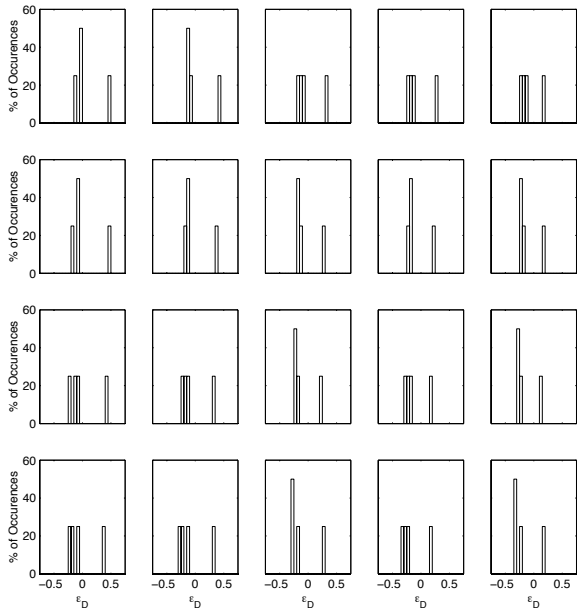

Figure 2.3: Error distributions at selected combinations of T_{eff} and ζ_{eff} for a few members from the ensemble

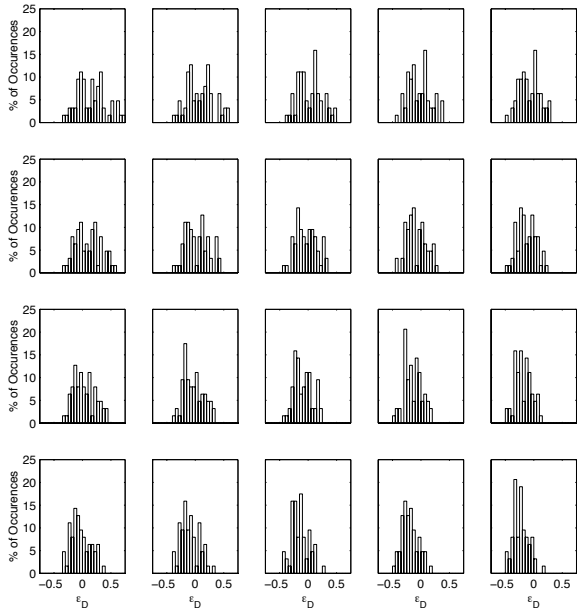

Figure 2.4: Error distributions at selected combinations of T_{eff} and ζ_{eff} for about half the members from the ensemble

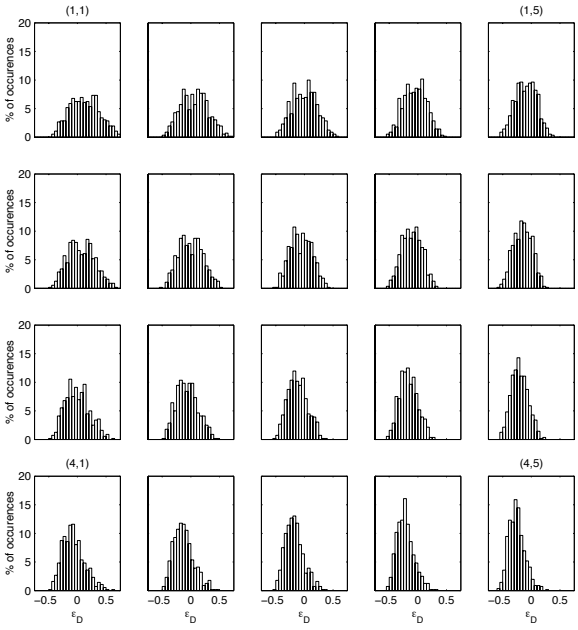

Figure 2.5: Error distributions at selected combinations of T_{eff} and ζ_{eff} for the entire ensemble

the histograms for a few members from the ensemble of systems and earthquake excitations. As would be expected from such a small sample size, the histograms do not have a smooth distribution. Figure 2.4 shows the histograms for about half of the full ensemble. The histograms are beginning to show definite signs of a smooth distribution. Figure 2.5 shows the histograms for the entire ensemble considered in this study. As the ensemble size increases, it is observed that the error distributions becomes much smoother.

The mean and standard deviation of the error distribution for every combination of T_{eff} and ζ_{eff} may be used to characterize the parameter space and will yield results similar to those shown in Figure 2.6. Notice the similarity between the mean value contour plot and the previous ϵ_D contour values in Figure 2.1. Contour lines run generally in the same direction on both plots and there exists a contour with a zero value. Whereas any point on the zero contour line in Figure 2.1 corresponds to zero error, the zero contour in Figure 2.6 corresponds to a distribution of errors with a zero mean value.

Many distributions in Figure 2.5 resemble a Normal distribution. Others more

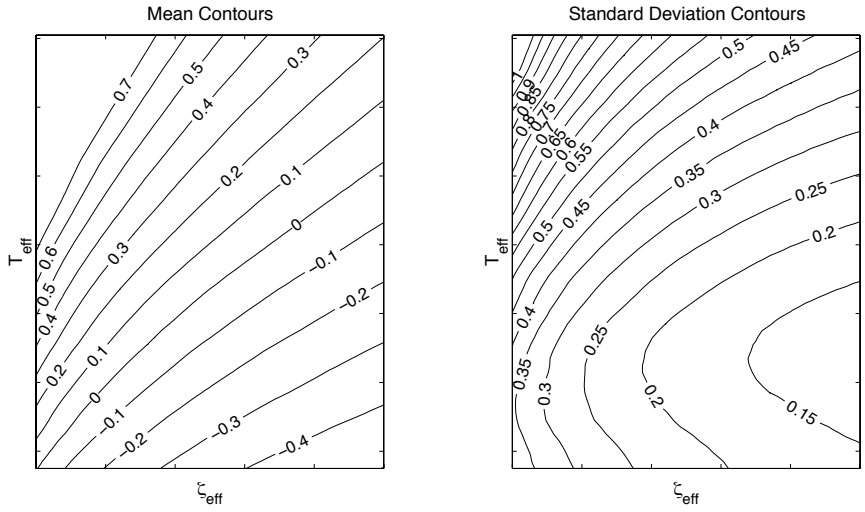

Figure 2.6: ϵ_D error distribution mean value contours and standard deviation contours over the two-dimensional parameter space for the entire ensemble

resemble a Log-normal distribution. For combinations of T_{eff} and ζ_{eff} in the parameter space closest to the optimal combination discussed later, the distributions more closely resemble a Normal distribution. Therefore, the Normal distribution will be used in the subsequent analysis.

The importance of using the standard deviation as well as the mean of the error distribution is illustrated in the following example. Two probability density functions are shown in Figure 2.7. For the more widely spread error distribution, the mean error value is zero, while for the tighter distribution, the mean error value is -5%. Solely in terms of the mean value, the widely spread distribution is more accurate than the tighter distribution. However, a more insightful way to analyze the distributions would be in terms of an acceptable range of error values. In this example, an acceptable range of error values could be chosen from -20% to 20%. The distribution with the mean value of -5% would be both more accurate and precise compared to the distribution with a mean value of 0%. Reliability is both the accuracy and precision of some statistical measure. Clearly, in terms of the stated acceptable range of error values, the -5% mean-valued distribution is much more reliable than the 0% mean-valued distribution.

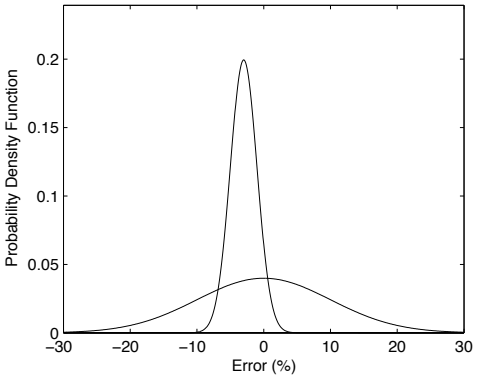

Figure 2.7: Illustration of probability density functions of displacement error for a Normal distribution

Let $\mathcal{F}$ be the probability that the error ϵ_D lies outside the range from a to b. Then, $\mathcal{F}$ may be expressed as

$$\mathcal{F} = 1 - Pr(a < \epsilon_D < b) \tag{2.4}$$

If the distribution of ϵ_D is assumed to be Normal, $\mathcal{F}$ can be expressed as

$$\mathcal{F} = 1 - \int_a^b \frac{1}{\sigma\sqrt{2\pi}} e^{\frac{-(x-m)^2}{2\sigma^2}} dx \tag{2.5}$$

where m is the mean value and σ is the standard deviation of the distributions of ϵ_D values.

In Figure 2.8, $\mathcal{F}$ is graphed for three different combinations of a and b. The selection of a and b are critical to the structure of $\mathcal{F}$. It can be shown mathematically that $\mathcal{F}$ is symmetric about the horizontal line through the average of a and b. Thus, choosing $a = -20\%$ and $b = 20\%$, implies $\mathcal{F}$ is symmetric about the 0% mean error line. It is further noted that increasing the size of the desired range of error values in a symmetric fashion makes the value of $\mathcal{F}$ decrease for a given mean and standard deviation. The smaller the value of $\mathcal{F}$, the more reliable the linear system prediction to be within the range from a to b. For a given value of mean and standard deviation, the reliability of the prediction increases as the range from a to b is widened.

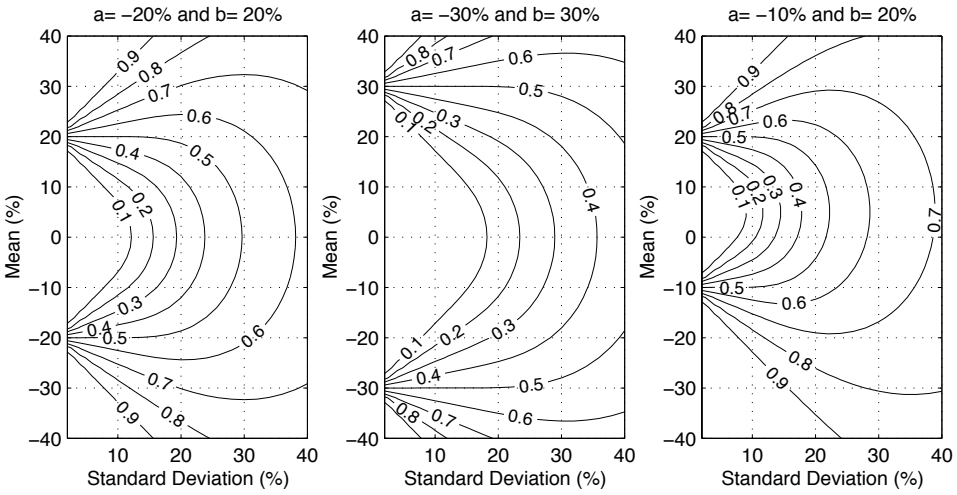

Figure 2.8: Contour plots of $\mathcal{F}$ for different values of a and b over a range of mean and standard deviation values

In Figure 2.8, consider a vertical line of constant standard deviation over the range of mean values on all three plots. Assume the constant standard deviation value to be 20%. For the cases $a = -20\%$, $b = 20\%$ and $a = -30\%$, $b = 30\%$, the minimum value of $\mathcal{F}$ will occur at the 0% mean value. However, for the case with $a = -10\%$ and $b = 20\%$, the minimum value of $\mathcal{F}$ will occur at the 5% mean value. Thus, a slight positive bias has been introduced into the location of the minimum value of $\mathcal{F}$.

It has been determined that the most desirable range of error values, ϵ_D, from an engineering design point of view is between -10% and $+20\%$. This conclusion was reached after consulting with several prominent structural engineers. This range of error values will be referred to as the Engineering Acceptability Range (EAR). This range takes into account the general desire for a more conservative design rather than an unconservative design. That is, a 20% error is more acceptable than a -20% error.

2.3 Optimization Criterion

The *optimum* point in the T_{eff}, ζ_{eff} parameter space is chosen to be the point that minimizes the probability that the error, ϵ_D, will be outside the Engineering Acceptability Range. The *Engineering Acceptability Criterion* may therefore be defined

as

$$\mathcal{F}_{EAR} \equiv 1 - Pr(-0.1 < \epsilon_D < 0.2) = \text{minimum} \tag{2.6}$$

Figure 2.9 shows contours of $\mathcal{F}_{EAR}$ as a function of T_{eff} and ζ_{eff}. Also shown is the optimal point over the two-dimensional parameter space which is denoted by a square.

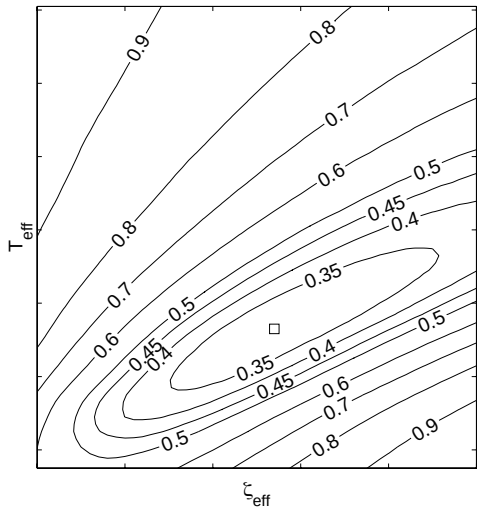

Figure 2.9: Contours of $\mathcal{F}_{EAR}$ over the T_{eff}, ζ_{eff} parameter space. The optimum point is marked by a square

The diagonal trend to the contours in Figure 2.9 can be explained by the following physical reasoning. Consider the displacement response of a linear oscillator subjected to an earthquake excitation. Decreasing the system damping will always increase the displacement response. Generally speaking, decreasing the natural period will also decrease the displacement response. Although this is not true in all cases, especially for near-field ground motions, it is a general trend that by increasing period and damping in the correct proportion, a nearly constant maximum displacement can be achieved.

The size and shape of the contours in Figure 2.9 give insight into the ramifications of using effective linear parameters different from the values at the optimal point. In Figure 2.9, the contour closest to the optimum point has a value of 0.35 while the minimum value of $\mathcal{F}_{EAR}$ ($\mathcal{F}_{EAR_{min}}$) is 0.31. The gradient of the contours is more

gradual along a line roughly from lower left to upper right. Therefore, if the effective period is under-predicted, it is best to also have an under-predicted damping. If the effective period is over-predicted, it is best to also have an over-predicted damping. In the general direction from lower right to upper left, the gradient of the contours is very large and the value of $\mathcal{F}$ quickly increases for relatively small changes in the effective parameters. Over-predicting one parameter and under-predicting the other can have serious repercussions on the reliability of the displacement prediction.

Figure 2.10 has points marked with an "X" that are in the general vicinity of $\mathcal{F}_{EAR_{min}}$. These are the locations of the distributions shown in Figure 2.5. The region near $\mathcal{F}_{EAR_{min}}$ is the area of most interest. The points in the parameter space not near $\mathcal{F}_{EAR_{min}}$ are of less importance. Whether the error distributions at these locations are Normal or Log-normal has little effect on the location of the optimal point. The distributions closest to $\mathcal{F}_{EAR_{min}}$ are approximately Normal. The effects of this assumption can be investigated further in terms of the Engineering Acceptability Range.

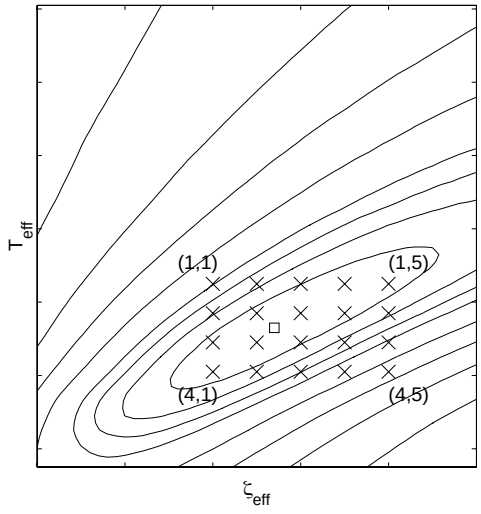

Figure 2.10: Locations of ϵ_D error distributions

If the Engineering Acceptability Criterion (Equation 2.6) was applied to the error distributions *before* making any assumptions about them, contours similar to those seen in Figure 2.11 would result. This figure shows the percentage of occurrences of

ϵ_D outside the Engineering Acceptability Range. ϵ_D without any assumptions about the distributions will be referred to as the raw data. Assuming the distributions of ϵ_D to be Normal results in contours of $\mathcal{F}_{EAR}$ as seen in Figure 2.9. Assuming the distributions of ϵ_D to be Log-normal results in contours of $\mathcal{F}_{EAR}$ as seen in Figure 2.12.

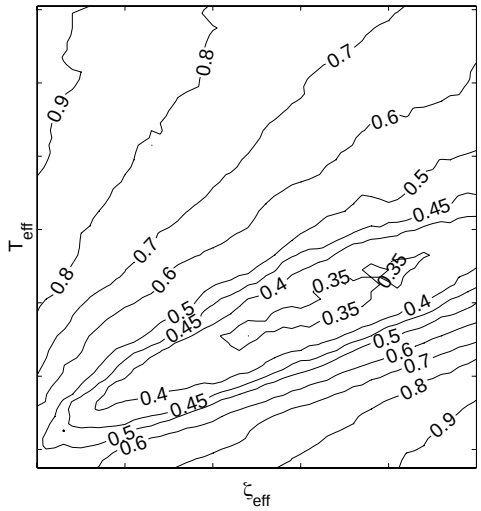

Figure 2.11: Percentage of occurrences of ϵ_D outside the Engineering Acceptability Range over the T_{eff}, ζ_{eff} parameter space. This will be further referred to as the contours of the raw data

Figure 2.13 shows the 0.35 valued contour of $\mathcal{F}_{EAR}$ for the raw data, distributions assumed as Normal and distributions assumed as Log-normal. $\mathcal{F}_{EAR_{min}}$ from the Log-normal assumption is outside the 0.35 contour from the raw data while $\mathcal{F}_{EAR_{min}}$ from the Normal assumption is well inside the 0.35 contour from the raw data. Clearly, the 0.35 contour from the Normal distributions is more representative of the contours from the raw data than the same contour from the Log-normal distributions.

Any assumptions made upon the data should not significantly change the location of the smallest valued contours. The region of the smallest valued contours is most critical to the selection of the minimum point. Therefore, the best assumption is that the distributions are Normal. However, it must be emphasized that this has only been determined in reference to the Engineering Acceptability Range. For a desired range of error values not near zero, the Normal assumption should not be used without

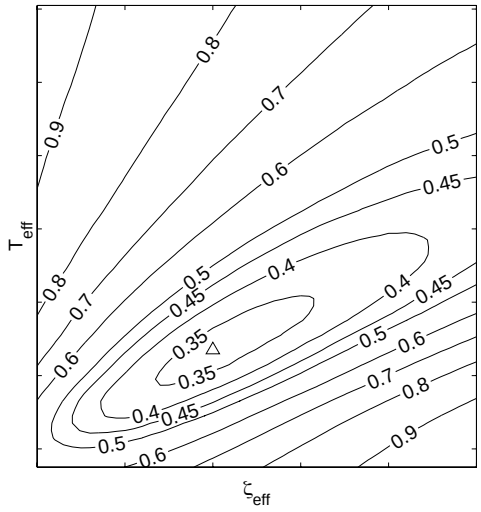

Figure 2.12: Contours of $\mathcal{F}_{EAR}$ over the T_{eff}, ζ_{eff} parameter space *assuming the distributions to be Log-normal*. The optimum point is marked by a triangle

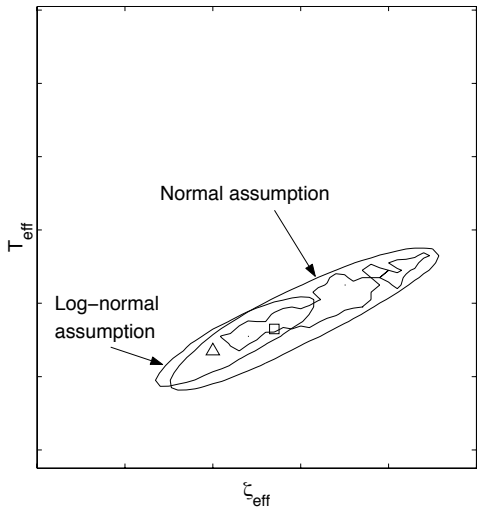

Figure 2.13: Contours of $\mathcal{F}_{EAR}$ for a value of 0.35 for the raw data (jagged contour), distributions assumed Normal and distributions assumed Log-normal. The triangle is the location of $\mathcal{F}_{EAR_{min}}$ for the Log-normal distributions and the square is the location of $\mathcal{F}_{EAR_{min}}$ for the Normal distributions

further investigation.

2.4 Nature of the Systems Considered

The ensemble discussed thus far has been a loosely defined combination of inelastic systems and ground motions. From Equation 1.1, an inelastic system is dependent upon the form of the nonlinear restoring force, $f(x, \dot{x})$. All nonlinear restoring forces used in this study will be hysteretic in nature. The differential equation of motion for a nonlinear system with nominal viscous damping, ζ_o, may be expressed as

$$m\ddot{x} + \frac{4\pi\zeta_o}{T_o}\dot{x} + f(x, \dot{x}) = -m\ddot{u}(t) \tag{2.7}$$

The term $f(x, \dot{x})$ is dependent not only upon the current displacement and velocity but also upon the displacement and velocity time history. Hysteretic systems have been chosen for this study because they best represent the response of buildings to earthquake motions. In laboratory testing, individual structural elements and assemblages have hysteretic response to cyclic loading. Buildings, which are composed of many structural elements and assemblages, also respond in a hysteretic manner when cycled into the inelastic range. An extensive discussion of the hysteretic systems used in this study is presented in Section 3.1.

All hysteretic systems considered will have a clearly definable value for the initial elastic period, T_o. The value of T_o is directly related to the elastic slope, k_o on the force-deflection curve as

$$T_o = 2\pi\sqrt{m/k_o} \tag{2.8}$$

All hysteretic systems considered have a clearly definable location on the force-deflection curve where the initial slope changes. This is called the yield point. The force associated with the yield point is the yield force, f_y, and the corresponding displacement is the yield displacement, D_y. The yield displacement, in conjunction with the maximum nonlinear system displacement, D_{inel}, defines the response ductility, μ,

as

$$\mu = \frac{D_{inel}}{D_y} \tag{2.9}$$

The ductility may be calculated only *after* a time history analysis has been performed for a given system with a given yield displacement.

2.5 Determining the Effective Linear Parameters

The full explicit functional dependence of ϵ_D may be indicated as follows

$$\epsilon_D(\frac{T_{eff}}{T_o}, \zeta_{eff} - \zeta_o, \alpha, \mu, \text{HYST}) = \frac{D_{lin}(T_{eff}, \zeta_{eff}) - D_{inel}(T_o, \zeta_o, \alpha, \mu, \text{HYST})}{D_{inel}(T_o, \zeta_o, \alpha, \mu, \text{HYST})} \tag{2.10}$$

The maximum displacement of the nonlinear system, D_{inel}, is a function of initial period, T_o, linear viscous damping, ζ_o, second slope ratio, α, response ductility, μ, and hysteretic model, denoted "HYST". The linear system response, D_{lin}, is a function of the two linear system parameters: period, T_{eff}, and damping, ζ_{eff}. It is desired to find effective linear parameters that are applicable over a range of T_o and ζ_o values. Therefore, multiple values of T_o and ζ_o will be included in the same ensemble. The two-dimensional T_{eff}, ζ_{eff} parameter space is transformed into the T_{eff}/T_o, $\zeta_{eff} - \zeta_o$ parameter space.

For a single hysteretic model, second slope ratio and ductility, groups of linear periods may be formed as indicated in Section 3.2. The nominal linear viscous damping values are discussed in Section 3.5.2. The Engineering Acceptability Criterion is applied to the error distributions over the T_{eff}/T_o, $\zeta_{eff} - \zeta_o$ parameter space and the optimum combination of T_{eff}/T_o and $\zeta_{eff} - \zeta_o$, is determined. Next, the ductility value is changed, and the entire process is repeated. The ductility values used in this study range from 1.25 to 6.5 at an increment of 0.25. This range of ductilities is believed to be most applicable to engineering design. Push-over curves with ductilities greater than 6.5 are unlikely, especially with the inclusion of P-$\triangle$ effects which increase lateral deformations for gravity load carrying elements as discussed in Section 1.4.2.2.

The optimum values of T_{eff}/T_o and $\zeta_{eff} - \zeta_o$ may be graphed as functions of ductility. Then, these results can be fitted with an analytical expression. Figure 2.14 shows the discrete optimum values of T_{eff}/T_o and $\zeta_{eff} - \zeta_o$ versus ductility and a curve fitted to them. The detailed curve fitting procedure is in Section 3.4.

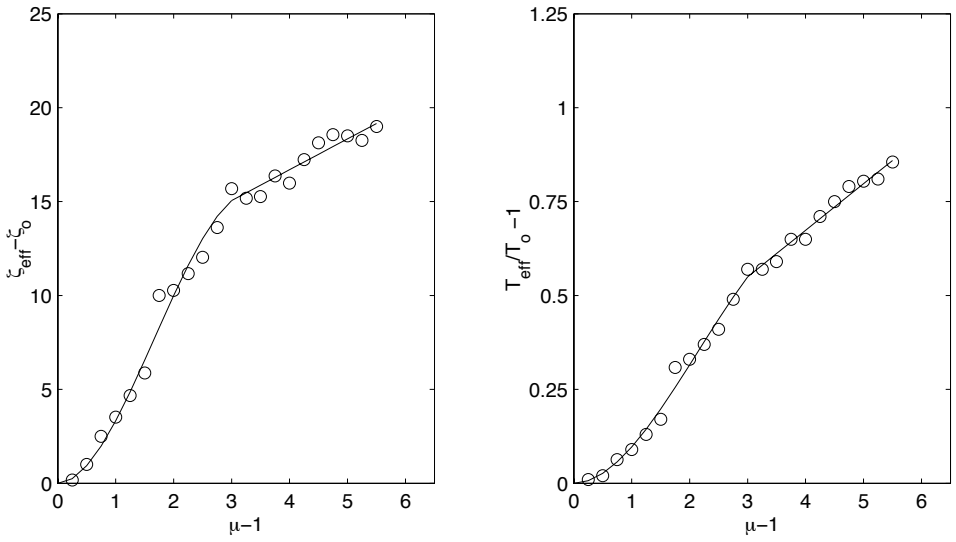

Figure 2.14: Example of optimal effective linear parameters - discrete points and the curve fitted to the data

A 3-D representation of $\mathcal{F}_{EAR_{min}} + 10\%$ as a function of ductility is shown in Figure 2.15. $\mathcal{F}_{EAR_{min}}$ is marked by a square on each 2-D face. The cone starts at the coordinate $\zeta_{eff} = \zeta_o$ and $\frac{T_{eff}}{T_o} = 1$, corresponding to the elastic case in which $\mathcal{F}_{EAR} = 0$. As the ductility increases, $\mathcal{F}_{EAR_{min}}$ also increases. Therefore, the reliability of the effective linear parameters is inherently worse as ductility increases. Projected on the back and bottom faces of the graph are 2-D representations of $\mathcal{F}_{EAR} + 10\%$. A 2-D view might lead one to believe the region of $\mathcal{F}_{EAR} + 10\%$ is a square when in fact it is an oval shape with a distinct orientation as seen in Figure 2.9.

2.6 Observations

The choice of displacement response error makes any scaling of the earthquake acceleration time histories unnecessary. Multiplying the acceleration time history by two

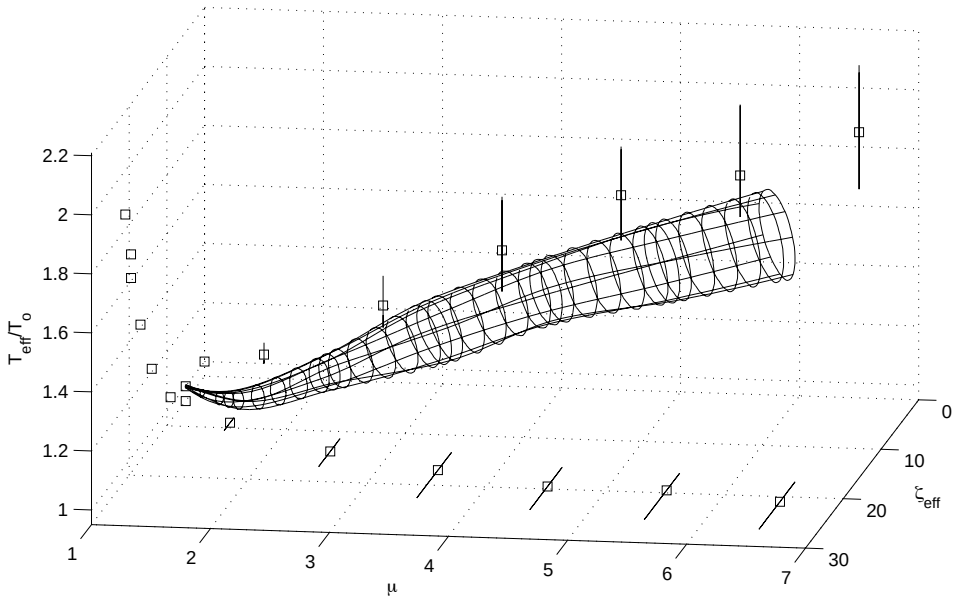

Figure 2.15: 3-D representation of $\mathcal{F}_{EAR_{min}} + 10\%$ as a function of ductility. The location of $\mathcal{F}_{EAR_{min}}$ is marked by a square on each two-dimension face. The lower reliability of the optimal effective parameters for higher ductility values is clearly seen

will double the value D_{lin}. However, it will also double the value D_{inel} for a given value of ductility and hence, the value of ϵ_D will remain constant. If the inelastic systems had been parameterized by yield force instead of ductility, this would not be the case.

Instead of categorizing the nonlinear systems by ductility, the strength reduction factor, R, could have been used. The strength reduction factor is defined as the ratio of the maximum elastic restoring force, $f_{lin_{max}}$, divided by the nonlinear yield force, f_y. That is,

$$R = \frac{f_{lin_{max}}}{f_y} \tag{2.11}$$

A graph of ductility versus strength reduction factor gives insight into why ductility has been chosen to characterize the system strength over strength reduction factor. Figure 2.16 shows R versus μ for a particular hysteretic system for the period range T_{short} subjected to a suite of ground motions. The mean value of the strength reduction factor as a function of ductility is below the line $R = \mu$ which corresponds to the Equal Displacement Rule ($D_{inel} = D_{lin}$). Although it is not possible to calculate

the mean value line of ductility as a function of R, the trend in the data implies that it would be far below the line of the mean value of R as a function of μ. The distribution of ductilities may extend to extremely large values even for a strength reduction factors as low as 2 to 3. Time histories would have to be run to values of ductility that are unrealistic in most structures in order to obtain a full distribution of ductilities. The ensembles for constant values of R would include extremely large values of ductility that are not attainable. This implies that the variance of R for a given value of μ is much greater than the variance of μ for a given value of R. This makes the analysis for constant R values less reliable than using constant ductility.

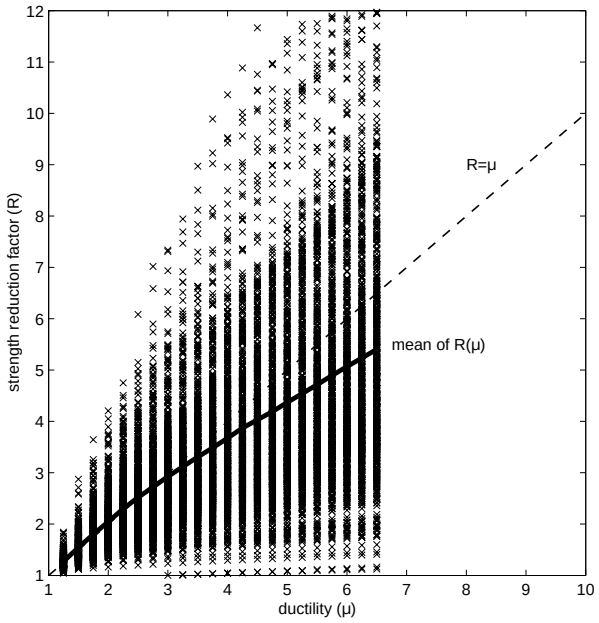

Figure 2.16: Strength reduction factor versus ductility for a sample of time history analyses of a single hysteretic model for period range T_{short} and a single value of second slope ratio

2.7 Evaluating the Effective Linear Parameters within the Framework of the Capacity Spectrum Method

Performance-Based Engineering proposes two Nonlinear Static Procedures: the Capacity Spectrum Method (Section F.1) and the Coefficient Method (Section F.2). The popularity of Nonlinear Static Procedures has increased because these techniques directly take into account the expected load-deformation characteristics of both the building elements and the entire structure without performing a nonlinear time history analyses. The nonlinearity of the structure is incorporated into the methods through a push-over analysis (Section 1.4.2.2). The push-over analysis transforms the multi-degree-of-freedom model into a load-deformation curve, or capacity curve. In the Capacity Spectrum Method, the capacity curve is approximated as an equivalent bilinear system. The bilinear system is then approximated as an equivalent linear system using effective linear parameters.

The Capacity Spectrum Method incorporates both structural capacity and seismic demand (Section 1.4.2.3) to determine a point where the demand and capacity are equal, referred to as the *Performance Point*. This is the expected displacement in the structure. The accuracy of the Capacity Spectrum Method will be evaluated using a new error measure. For a given ground motion, the Performance Point Error, $\epsilon_{D_{pp}}$, is defined as the difference between the displacement at the Performance Point and the maximum inelastic displacement divided by the maximum inelastic displacement. This can be expressed as

$$\epsilon_{D_{pp}}(\alpha, \mu, \text{HYST}) = \frac{D_{lin}(T_{eff}(T_o, \alpha, \mu_{pp}), \zeta_{eff}(\zeta_o, \alpha, \mu_{pp})) - D_{inel}(T_o, \zeta_o, \alpha, \mu, \text{HYST})}{D_{inel}(T_o, \zeta_o, \alpha, \mu, \text{HYST})} \tag{2.12}$$

Error statistics will be created by combining all T_o and ζ_o values for a hysteretic model, second slope ratio and ductility.

Several sources of error are introduced by the Capacity Spectrum Method. Errors may arise in both the determining of structural capacity and seismic demand. To evaluate the error from the equivalent linear parameters, all other sources of error

must be eliminated or determined to be negligible.

In determining the structural capacity, two sources of error exist: the capacity spectrum calculation and the hysteretic classification. A large source of error may come from representing a multi-degree-of-freedom building model by a single-degree-of-freedom system as discussed in Section 1.4.2.2. This source of error is eliminated by considering only single-degree-of-freedom structures.

The second source of error in determining the structural capacity is the hysteretic classification. Classifying a building as a specific hysteretic classification is discussed in Section 3.1. However, the process of determining the hysteretic model is removed because the actual hysteretic model is known apriori. Therefore, both sources of error associated with the structural capacity have now been removed.

In determining the seismic demand, error is introduced in determining the design spectrum and demand spectra (Section 1.4.2.3). In practical application, the design spectrum will be developed to represent several possible seismic events over some length of time. A design spectrum that represents several events is generally smooth and conservative. However, the error associated with using a design spectrum different from the earthquake response spectrum is eliminated by using the earthquake response spectrum as the design spectrum. Demand spectra are calculated using the effective linear parameters. The only remaining source of error in the Capacity Spectrum Method is the error associated with the effective linear parameters.

2.8 The Modified Acceleration-Displacement Response Spectrum

The conventional Capacity Spectrum Method uses the secant period as the effective linear period in determining the Performance Point. The effective linear periods developed in this study are very different from the secant period. Therefore, the conventional Capacity Spectrum Method will be modified in some fashion to enable the use of the effective parameters developed in this study.

The solution is to modify the seismic demand. The demand spectrum, in Acceleration-Displacement Response Spectrum (ADRS) format (Section 1.4.2.3), will be reshaped by the *modification factor*. Every value of acceleration at every displacement will be multiplied by the ratio of the secant stiffness of the capacity spectrum to the effective stiffness. Alternatively, the modification factor can be expressed as the square of the ratio between the effective period and secant period. An example of this is shown in Figure 2.17.

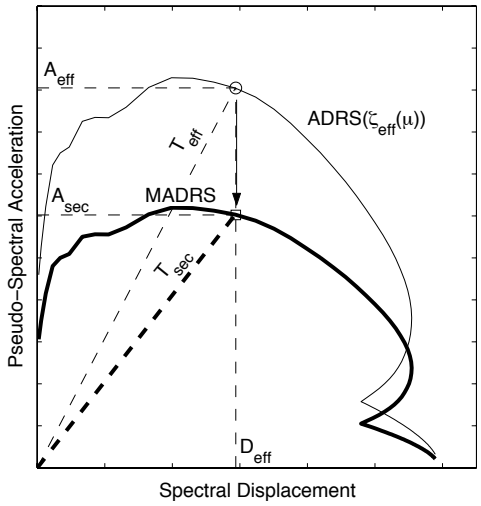

Figure 2.17: Application of the modification factor to the Acceleration-Displacement Response Spectrum (ADRS) creating the Modified Acceleration-Displacement Response Spectrum (MADRS)

The modification factor, M, is defined as

$$M = A_{sec}/A_{eff} \tag{2.13}$$

A_{eff} is the maximum acceleration obtained by the intersection of the ADRS and the radial line representing T_{eff}. A_{sec} is the value of acceleration corresponding to the intersection of the MADRS and the radial line representing the T_{sec}. A_{eff} and A_{sec} may be expressed as

$$A_{eff} = D_{eff}(\frac{2\pi}{T_{eff}})^2 \tag{2.14}$$

$$A_{sec} = D_{eff}(\frac{2\pi}{T_{sec}})^2 \tag{2.15}$$

Substituting Equations 2.14 and 2.15 into Equation 2.13 yields an alternative expression for the modification factor

$$M = (\frac{T_{eff}}{T_{sec}})^2 = (\frac{T_{eff}}{T_o}\frac{T_o}{T_{sec}})^2 \tag{2.16}$$

The Modified Acceleration-Displacement Response Spectrum (MADRS) can now be used in combination with the capacity spectrum to determine the Performance Point as shown in Figure 2.18. Through the implementation of the modification factor, the Performance Point appears to occur at the secant period, when in fact it occurs at the effective period which is less than the secant period.

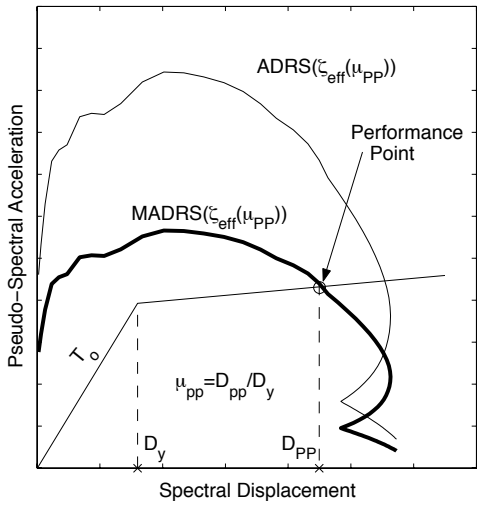

Figure 2.18: Procedure for determining the Performance Point using the Modified Acceleration-Displacement Response Spectrum (MADRS)

Additional insight can be gained into the Performance Point by creating a Locus of Performance Points. MADRS (demand spectra) must be computed for a range of ductility values. Mark the intersection of each MADRS with the corresponding secant period line from the capacity spectrum. Connect all points of intersection to create a Locus of Performance Points. The Performance Point is the intersection of the Locus of Performance Points and the capacity spectrum. This is shown in Figure 2.19. From

the information generated by this procedure, it can be seen how the location of the Performance Point will change for small variations in either the capacity spectrum or demand spectra. A more detailed procedure is discussed in Section 5.1.

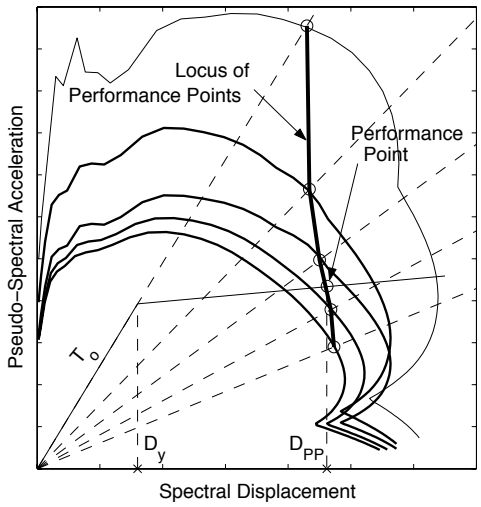

Figure 2.19: Procedure for determining the Performance Point using the Locus of Performance Points

Chapter 3

Effective Linear Parameters

3.1 Hysteretic Models

For all the hysteretic models used in this study, the differential equation of motion is

$$m\ddot{x} + \frac{4\pi\zeta_o}{T_o}\dot{x} + f(x,\dot{x}) = -m\ddot{u}(t) \tag{3.1}$$

The inelastic systems were subjected to a sinusoidal acceleration history and Figures 3.1 through 3.4 show the response of the different hysteretic models graphed as force ($f(x,\dot{x})$) versus displacement (x). The properties of the different hysteretic systems are explained in Sections 3.1.1 through 3.1.5.

3.1.1 Bilinear Hysteretic Model (BLH)

The bilinear hysteretic model (BLH) is shown in Figure 3.1. The force versus displacement diagram has two slopes: the initial linear stiffness, k_o, and the post-yield stiffness, αk_o. The point where the slope changes from the initial linear stiffness to the post-yield stiffness is the yield point of the structure. The second slope ratios, α, considered in this study are 0, 2, 5, 10 and 60%. The initial linear stiffness is regained immediately after all velocity reversals. The positive yield point and the negative yield point are always separated by a constant amount of force and displacement. Yielding of the positive yield point causes translation of the negative yield point and vice verse.

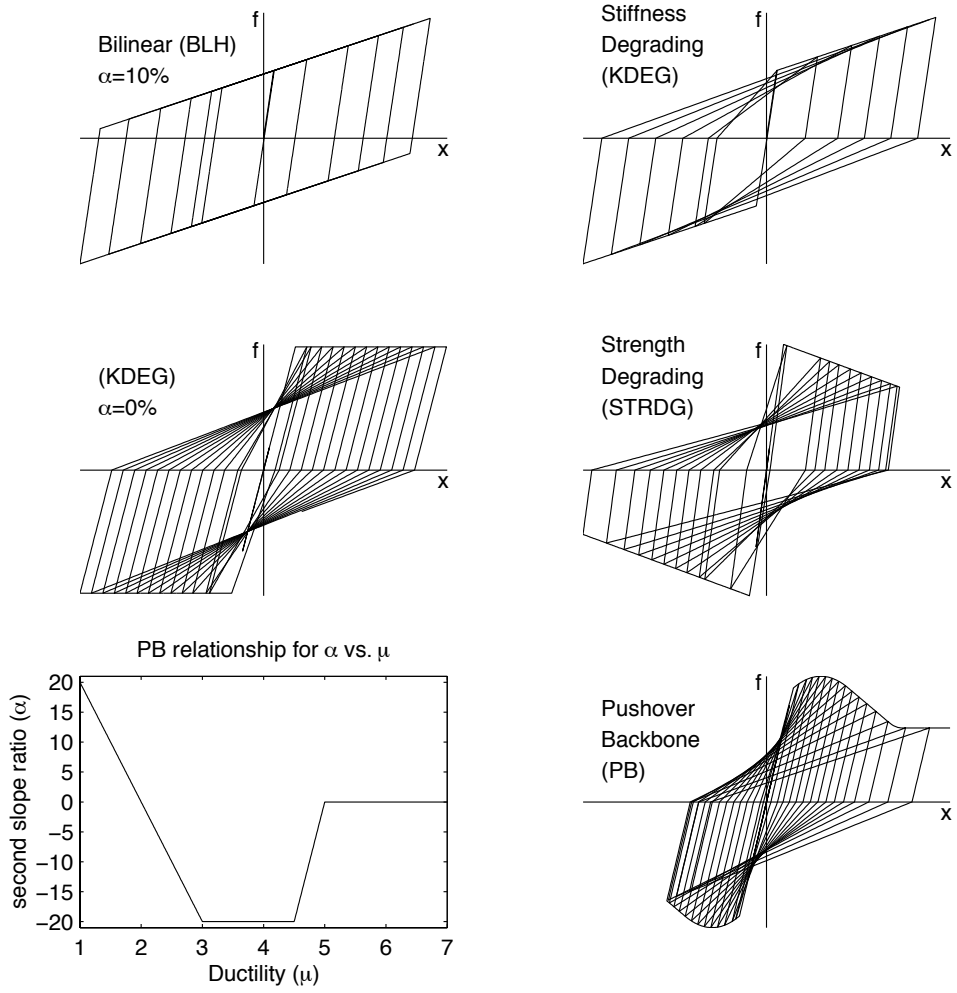

Figure 3.1: Force (f) versus displacement (x) for bilinear, stiffness degrading, strength degrading and push-over backbone models from a time history analysis with a sinusoidal acceleration function

3.1.2 Stiffness Degrading Model (KDEG)

The stiffness degrading model (KDEG) is shown in Figures 3.1 and 3.2. Second slope ratios of 0, 2, 5, 10 and 60% are considered. This particular model was initially developed by Riddell and Newmark [62]. The force versus displacement diagram has a decreasing stiffness as ductility increases. Once nonlinear response has occurred, a zero-force crossing will always change slope and head directly to the yield point. Translation of the positive yield point has no effect on the location of the negative yield point and vice verse. Figure 3.2 shows a harmonic response sequence. The first nonlinear excursion is experienced from point 1 to point 2. Then, on a velocity reversal the stiffness changes back to the initial linear stiffness until the force becomes less than zero at point 3. The stiffness then decreases so that the response heads directly toward the negative yield point (point 4). The response continues through points 5, 6, 7 and 8.

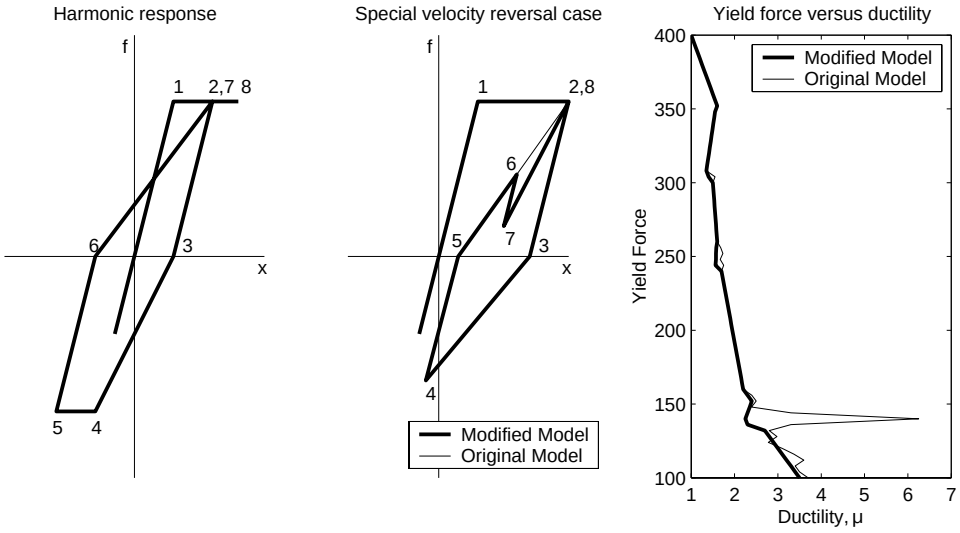

Figure 3.2: Stiffness degrading (KDEG) hysteretic properties and yield force versus ductility plot for the original model by Riddell and Newmark and the modified model used in this study

In this study, the original Riddell and Newmark model has been modified for in-cycle velocity reversals as shown in Figure 3.2. The first velocity reversal after a zero force crossing will always retain the initial stiffness but a second velocity reversal

without a zero force crossing will head directly to the previous yield point. Both models follow the same sequence from points 1 to 7. For a velocity reversal at point 7, the original model goes back to point 6, then to point 8. The modified model used in this study goes from point 7 directly to point 8 for a velocity reversal at point 7. This subtle feature has been added so that the relationship between the response ductility and the yield force does not behave unrealistically. In the original model, a slight change in yield force can change a double reversal with no zero crossing into a single reversal with a zero crossing. This can cause the response ductility to jump wildly for cases at large ductilities.

An example is shown in Figure 3.2. The time histories revealed that a change in the initial yield force level of less than 0.1% could triple the response ductility. However, this happens very rarely due to the fact that it is accentuated only when the current response ductility is much larger than the ductility at which the double reversal occurs. This is directly related to the slope of the line from point 7 to point 6 and the slope of the line from point 7 to point 8. If the difference in these two slopes is large, there is a possibility that the wild jump in response ductility may occur. It is believed that this modification has only a slight effect on any of the response statistics that will be presented in this study.

3.1.3 Strength Degrading Model (STRDG)

A strength degrading model (STRDG) is shown in Figure 3.1 This model was developed by using a negative second slope ratio of -3% and -5% for the stiffness degrading model with the strength degradation occurring within a cycle of response. Strength degradation can occur in two ways, in-cycle or out-of-cycle as seen in Figure 3.3. Out-of-cycle degradation models calculate the amount of strength and stiffness degradation as a function of the hysteretic energy dissipated and the peak deformation in previous cycles. These types of models can never exhibit a negative post-yield stiffness.

An in-cycle degradation model was chosen for this study because it was desired

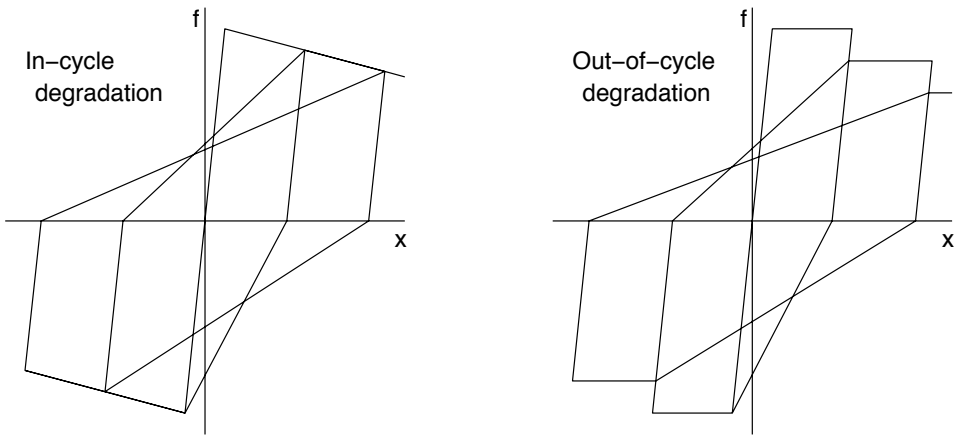

Figure 3.3: Hysteresis loops of strength degrading models with in-cycle and out-of-cycle degradation

to have a hysteretic model push-over curve the same as the building push-over curve. This occurs for any non-negative second slope ratio model. To be consistent, it was decided to have it also occur for the negative second slope ratios.

3.1.4 Pinching Hysteretic Models (PIN)

Pinching hysteretic models (PIN) are shown in Figure 3.4. Models PIN1 and PIN2 were developed by Iwan and Gates [41], [44]. The models consist of a combination of linear and Coulomb slip elements. The schematic of the three element system is also shown in the figure. The model consists of an elastic spring with stiffness k_e, an elastic-plastic element with stiffness k_s with yield force f_s and a grouping of Coulomb slip elements with stiffness k_c that both yields in tension (cracking force, f_b) and compression (crushing force, f_c). The elastic spring element and elasto-plastic element together form a bilinear hysteretic system. The inclusion of the Coulomb slip elements make the model a pinching hysteretic model. The nominal stiffness of the system is defined as k_o which is obtained by setting the crack strength equal to zero ($f_b = 0$). The second slope ratios considered are 2, 5, 10 and 60%.

Three parameters describe the PIN systems: β, γ and δ (Equations 3.2) through 3.4). The Coloumb slip elements determine the energy dissipated in a cycle of response

which is the area enclosed by the hysteresis loops. The hysteretic energy dissipated by PIN1 is less than the hysteretic energy dissipated by PIN2. Increasing β in PIN2 will increase the hysteretic energy dissipated and eventually the hysteresis loops will be the same as the bilinear model. Ductility, μ, is measured as x_{max}/x_s.

$$\beta = k_s/k_c \tag{3.2}$$

$$\gamma = x_s/x_c = \frac{f_s/k_s}{f_c/k_c} = f_s/f_c * 1/\beta \tag{3.3}$$

$$\delta = f_b/f_c \tag{3.4}$$

Model	β	γ	δ
PIN1	0.2	1.0	0.0
PIN2	1.0	1.0	0.0

Table 3.1: System parameters for pinching hysteretic models

3.1.5 Push-over Backbone Model (PB)

The stiffness degrading model has been modified so that the second slope ratio varies as a function of ductility as shown in Figure 3.1. This model will be referred to as the push-over backbone model (PB). A push-over curve commonly obtained by structural engineers is one that does not have a clearly defined yield point or a constant second slope ratio. The nonlinear static procedures require a bilinear approximation for the capacity curve. However, if a model such as the push-over backbone was used to represent a building push-over curve exactly, then there would be no need for a bilinear approximation.

The push-over backbone model also shows that the new methodology will work for any type of hysteretic model. Effective linear parameters may be obtained so long as the model is definable by some response quantity, such as ductility or strength reduction factor.

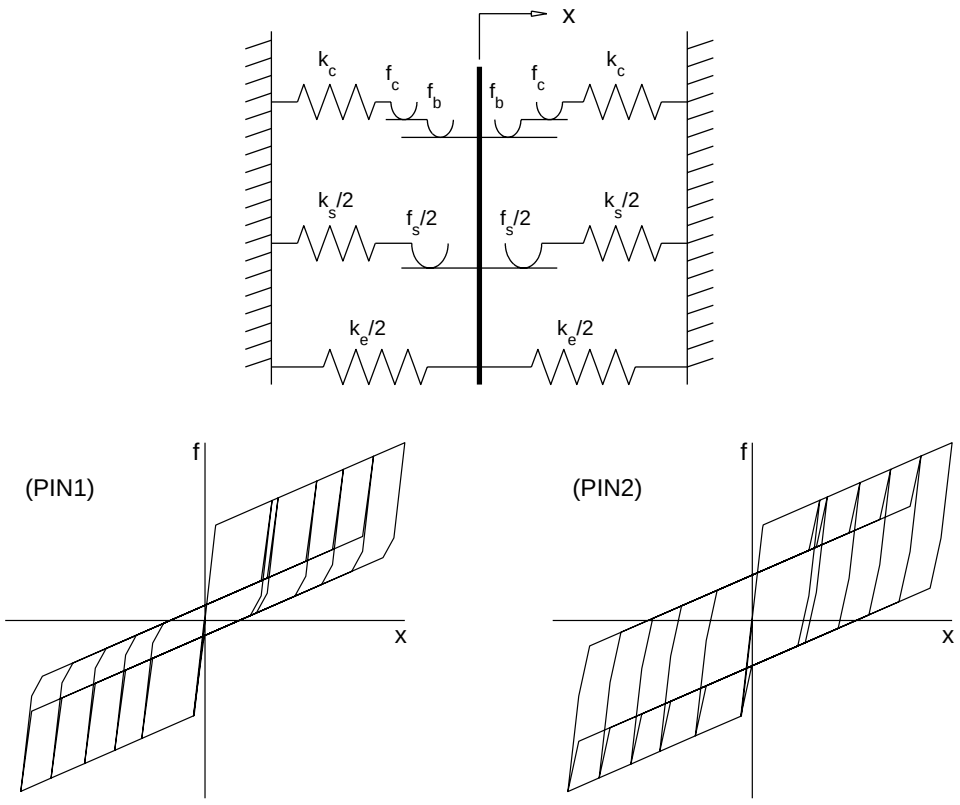

Figure 3.4: Schematic diagram and hysteresis loops for the pinching models

3.1.6 Hysteretic Classification

Once a push-over curve has been obtained, there still exists the question as to how the building will behave during the inelastic cycles of response. Answering this question is left to the judgment of the engineer by examination of the structural plans, or in the case of a retrofit, an inspection of the existing building [3].

Most new construction with a well designed lateral force resisting system should be categorized as a bilinear hysteretic system (BLH). The lateral resisting system should be free from any non-structural elements that may effect its performance. For example, non-structural elements should not be constructed such that they will effect the stiffness of the building upon failure.

Any existing construction that has a well designed lateral load resisting system with structural elements that are well detailed and constructed properly should probably be categorized as stiffness degrading (KDEG). The condition of the lateral load resisting system must be determined through investigation of the structural plans or an inspection of the building. The year in which the building was constructed and the material of construction will have an impact on this categorization. Older buildings, particularly those built before 1970, should be examined very carefully since it was the 1971 San Fernando Earthquake that motivated many changes in structural design. Existing concrete buildings must be well detailed to fit in this category. Design and detailing of concrete buildings changed significantly after the structural failures experienced at such buildings as the Olive View Hospital in Sylmar due to the 1971 event. New construction with slightly questionable lateral load resisting elements may conservatively be categorized as stiffness degrading.

Buildings with poor existing lateral force systems should be categorized as a pinching hysteretic model. The components making up the lateral resisting system may be poorly detailed or are expected to have very poor hysteretic response properties. The two pinching models (PIN1 and PIN2) reflect different amounts of dissipated hysteretic energy. For a building that is poorly designed but has a large amount of redundancy, perhaps the PIN2 model with less degradation is best. Also, a building

with a large amount of seismic mass may be categorized as PIN2. Any other poorly designed existing building should be categorized as PIN1. Conservatively, all poorly designed existing buildings may be categorized as PIN1 for the analysis.

3.2 Ground Motions and Structural Period Groups

3.2.1 Far-field Motions and Structural Periods

Twenty-eight far-field ground motion records from the CIT-SMARTS database [64] were used in this study. Each record was obtained by rotating the two perpendicular components to the maximum ground velocity direction. These ground motions represent a broad range of free-field motions varying in earthquake magnitude, soil conditions and epicentral distance. To avoid records possibly effected by soil-structure interaction, no records from building basements were used in this study. All far-field records are listed in Section G.1.

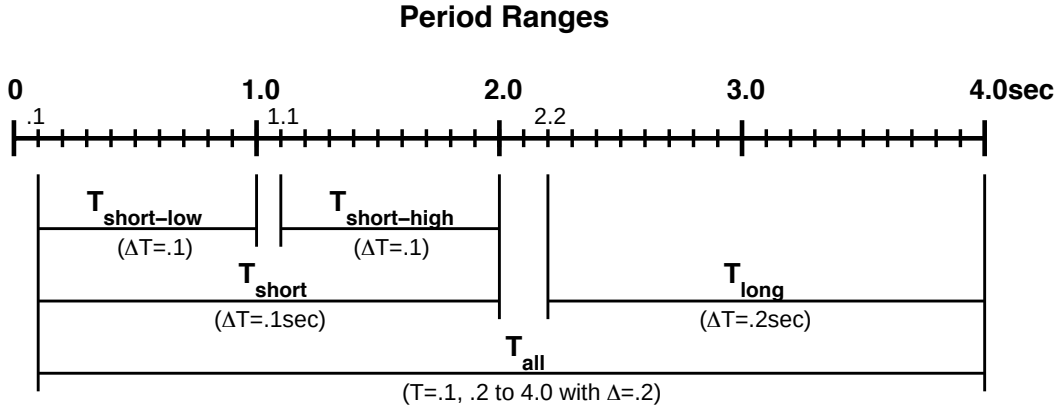

Figure 3.5: Groupings of initial periods, T_o

For the far-field analysis, the groups of linear structural periods are shown in Figure 3.5. The overall period range is from 0.1 sec to 4.0 seconds. T_{all} is over the entire range while T_{long} and T_{short} each account for half of T_{all}. The T_{short} range is further subdivided into $T_{short-low}$ and $T_{short-high}$. The period range deemed most applicable to the analysis of buildings is the T_{short} range. This period range covers low to

mid-rise structures that are commonly analyzed by nonlinear static procedures. Long period structures, like high-rise buildings, may have higher mode effects that require special consideration and may not be good candidates for analysis by a nonlinear static procedure as discussed in Section 1.4.2.2. Results for far-field motions will be for the T_{short} period range unless noted otherwise.

3.2.2 Near-field Motions and Structural Periods

A suite of 14 near-field motions was also obtained from sources at the California Institute of Technology. The near-field motions were analyzed in the orientations received. The motions have been parameterized by an effective pulse period from the velocity time history, T_p, defined as the time required for one complete cycle in the velocity time history. A complete velocity cycle is defined as starting from zero velocity to a peak, then to the opposite peak, then back to zero. This is an idealized requirement as most records will not have a smooth, complete cycle velocity pulse. If a complete pulse cycle is not present, the pulse period is estimated from the fragment of the pulse seen in the record. Consider a velocity history containing a single-sided pulse (from zero to a max, then back to zero). The time for that single-sided pulse must be doubled to give an estimate for a complete pulse cycle. In all near-field records considered, there exists at least part of a distinct velocity pulse.

The need to parameterize near-field ground motions by a pulse period is discussed by several researchers [7], [22], [36], [39], [51]. Within the context of this study, it is especially important because a building will be represented by an equivalent single-degree-of-freedom system through the push-over analysis. Response of a building in a mode different from the load profile used in the push-over analysis will make the capacity curve representation inaccurate. Values of T_o/T_p (ratio of initial linear period to pulse period) much greater than 1.0 make the single-degree-of-freedom approximation unreliable as traveling wave phenomenon may occur [36], [39]. To stay away from this range, the hysteretic systems are analyzed for T_o/T_p values from 0.1 to 1.2 with an increment of 0.1. The ground motions and their T_p values are given

in Section G.2. The structural periods are grouped into two categories, one with periods much less than the pulse period ($T_o/T_p \leq 0.7$) and one with periods centered around the pulse period ($0.8 \geq T_o/T_p \geq 1.2$).

3.3 Optimum Effective Linear Parameter Calculation

The methodology presented in Chapter 2 for determining effective linear parameters is applied to all hysteretic models and second slope values seperately. A nominal visocous damping value of 5% is used for all nonlinear time history analyses. The use of other damping values will be discussed in Section 3.5.2.

Refer to Figure 3.6. Consider the bilinear hysteretic model with a second slope ratio of 2%. For a ductility of 1.25, the maximum inelastic time history displacement, D_{inel}, is computed for a range of T_o values and a suite of ground motions. For a given value of T_o and ground motion, D_{inel} is compared to the entire two-dimensional grid of D_{lin} values from linear time histories with varying combinations of period, T_{eff}, and damping, ζ_{eff}. The values of damping range from 5% to 30% at an increment of 0.25%. The linear period values are chosen such that the values of T_{eff}/T_o range from 0.9 to 2.2 at an increment of 0.02. A two-dimensional grid of ϵ_D values result for every combination of T_o and ground motion. The two-dimensional grids are combined such that at every coordinate $\zeta_{eff} - \zeta_o$, T_{eff}/T_o there exists a distribution of ϵ_D values.

As discussed in Chapter 2, the distributions are assumed to be Gaussian. Figure 3.7 shows typical examples of mean and standard deviation contour plots of ϵ_D. Computing the value of $\mathcal{F}_{EAR}$ (Equation 2.6) at every combination $\zeta_{eff} - \zeta_o$, T_{eff}/T_o is extremely time consuming. However, not all values of $\mathcal{F}_{EAR}$ need to be computed. Due to the structure of the mean and standard deviation contours, along each mean contour, there exists a location of minimum standard deviation. These combinations of mean and standard deviation comprise the "eligible points" at which evaluation of $\mathcal{F}_{EAR}$ will be necessary. $\mathcal{F}_{EAR_{min}}$ over the eligible points will identify the optimal

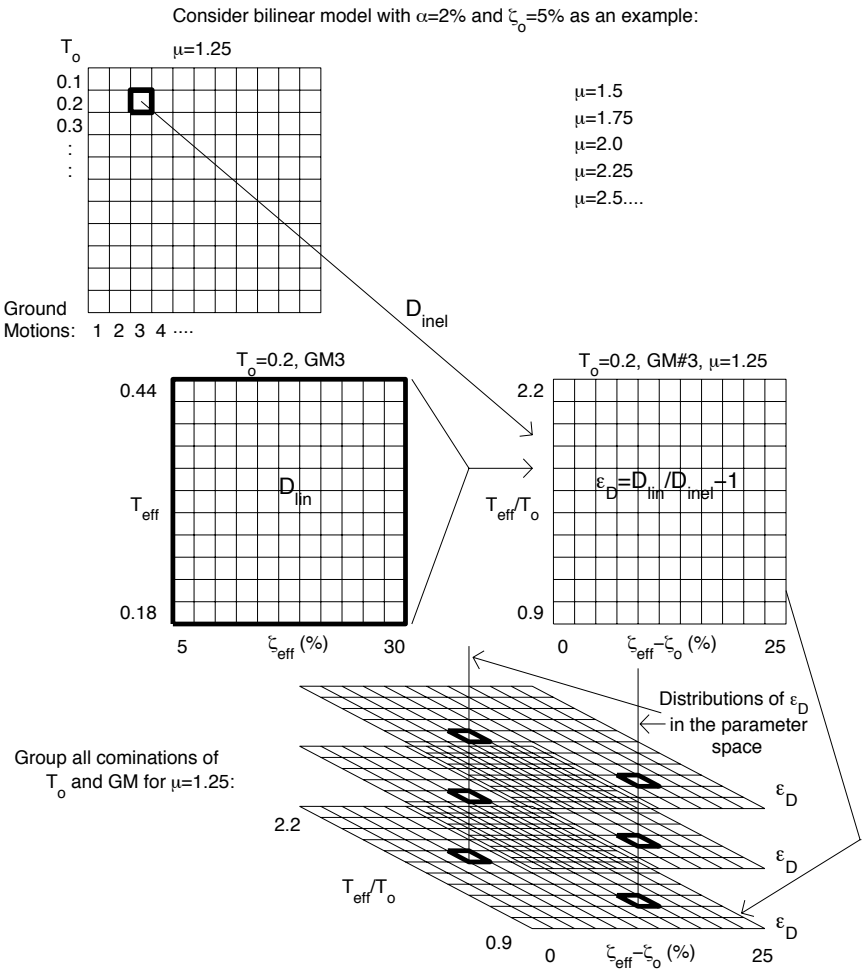

Figure 3.6: Illustration of assembling ϵ_D error distributions at all points over the two-dimensional parameter space

combination of $\zeta_{eff} - \zeta_o$ and T_{eff}/T_o.

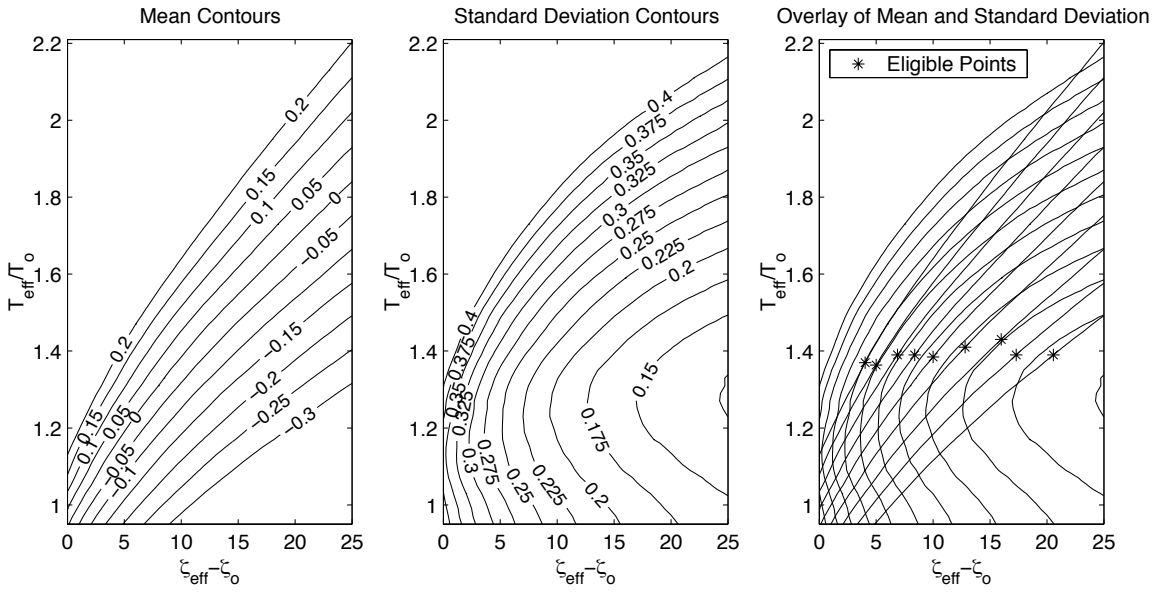

Figure 3.7: ϵ_D mean value contours (left), standard deviation contours (middle) and the overlay of both the mean contours and standard deviation contours (right) producing a line of eligible points

Due to the structure of $\mathcal{F}_{EAR}$ as seen in Figure 2.8 (Equation 2.6) and the trend of the eligible points, not all mean values need to be checked. Only mean values of $(a + b)/2$ and less must be examined. Mean values larger than $(a + b)/2$ need not be checked because as the mean increases, so does the standard deviation. This guarantees a larger value of $\mathcal{F}_{EAR}$. However, as the mean value decreases from $(a + b)/2$, the minimum standard deviation also decreases. Combinations of mean and minimum standard deviation are overlayed on a plot of $\mathcal{F}_{EAR}$, as seen in Figure 3.8. The minimum value, $\mathcal{F}_{EAR_{min}}$, is marked by a square.

3.4 Analytical Expressions for the Effective Linear Parameters

The optimal effective period and effective damping values determined at discrete values of ductility from 1.25 to 6.5 will be fit with an analytical expression. The optimal

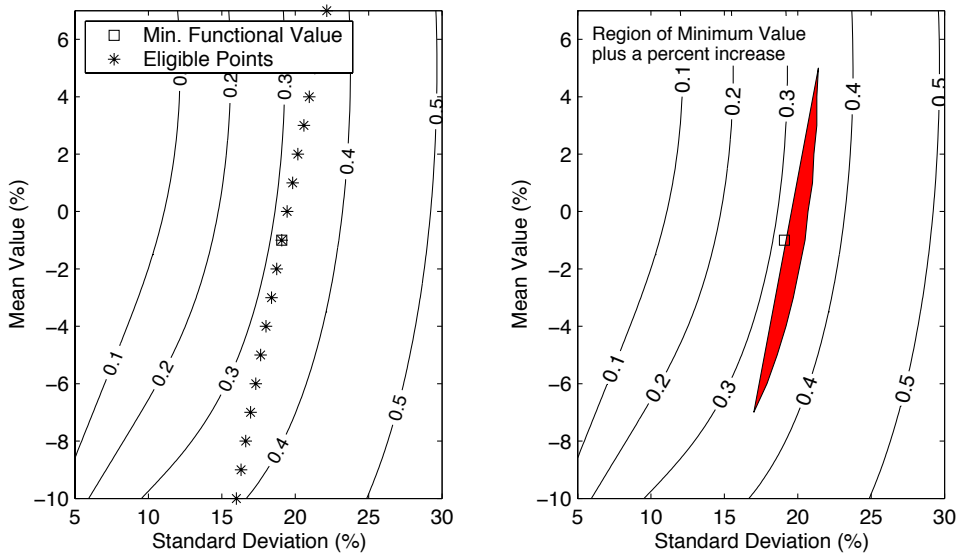

Figure 3.8: Minimum functional value of $\mathcal{F}_{EAR}$ ($\mathcal{F}_{EAR_{min}}$) and a shaded region of $\mathcal{F}_{EAR_{min}} + 10\%$

effective period and damping values for far-field motions are shown in Figure 3.9 for the bilinear hysteretic model and Figures 3.10 through 3.12 for the stiffness degrading and pinching hysteretic models. For near-field motions, optimal values for the bilinear model are presented in Figures 3.13 and 3.14 while the stiffness degrading model effective linear parameters are shown in Figures A.1 and A.2. Both the effective period and the effective damping will be expressed as continuous functions of ductility, μ. This is most easily achieved by fitting a curve to the effective period and damping points.

From observations on many sets of optimal points, a linear trend in both the effective period and damping was present for ductilities greater than 4.0 for far-field ground motions and 3.0 for near-field ground motions. Those optimal points were fit with a straight line. The value of the linear fit at $\mu = 4.0$ was used as a constraint on the fit of optimal points at the lower ductilities. Another constraint was that the curve must originate from the point $\mu = 1$, $T_{eff}/T_o = 1$ for effective period and from the point $\mu = 1$, $\zeta_{eff} = \zeta_o$ for effective damping. The optimal points for $\mu < 4$ were fit with a cubic function without the linear term because the optimal points had a distinct double curvature trend. There was no linear trend present in the

optimal points at the smaller ductilities. All data fitting was done by a least squares approach that minimized the absolute error difference between the optimal point and the analytical expression.

Insight into the sensitivity of the optimal point was discussed in Section 2.6 and is further discussed here. The shaded region in the Figure 3.8 represents the area surrounded by the line of eligible points and the curve of the minimum value of $\mathcal{F}_{EAR}$ plus a percentage increase. This region transformed back to the $\zeta_{eff} - \zeta_o$ and T_{eff}/T_o parameter space results in an oval shape. Contours of $\mathcal{F}_{EAR_{min}}$ +5, 10, 15 and 20% are shown in Figure 3.15. This reveals the increased sensitivity of the optimal parameters at the lower ductilities. At larger ductilities, the optimal point is less sensitive to deviations from the optimal point.

The general form of the equations for far-field motions is assumed to be

$$\zeta_{eff} - \zeta_o = \mathbf{A}(\mu - 1)^2 + \mathbf{B}(\mu - 1)^3 \text{ for } \mu < 4.0 \tag{3.5}$$

$$\zeta_{eff} - \zeta_o = \mathbf{C} + \mathbf{D}(\mu - 1) \text{ for } 4.0 \leq \mu \leq 6.5 \tag{3.6}$$

$$\frac{T_{eff}}{T_o} - 1 = \mathbf{E}(\mu - 1)^2 + \mathbf{F}(\mu - 1)^3 \text{ for } \mu < 4.0 \tag{3.7}$$

$$\frac{T_{eff}}{T_o} - 1 = \mathbf{G} + \mathbf{H}(\mu - 1) \text{ for } 4.0 \leq \mu \leq 6.5 \tag{3.8}$$

Coefficients are in Table 3.2 for period range T_{short}.

For the near-field motions, the general form of the equations is assumed to be

$$\zeta_{eff} - \zeta_o = \mathbf{A}(\mu - 1)^2 + \mathbf{B}(\mu - 1)^3 \text{ for } \mu < 3.0 \tag{3.9}$$

$$\zeta_{eff} - \zeta_o = \mathbf{C} + \mathbf{D}(\mu - 1) \text{ for } 3.0 \leq \mu \leq 6.5 \tag{3.10}$$

$$\frac{T_{eff}}{T_o} - 1 = \mathbf{E}(\mu - 1)^2 + \mathbf{F}(\mu - 1)^3 \text{ for } \mu < 3.0 \tag{3.11}$$

$$\frac{T_{eff}}{T_o} - 1 = \mathbf{G} + \mathbf{H}(\mu - 1) \text{ for } 3.0 \leq \mu \leq 6.5 \tag{3.12}$$

Coefficients are in Table 3.3.

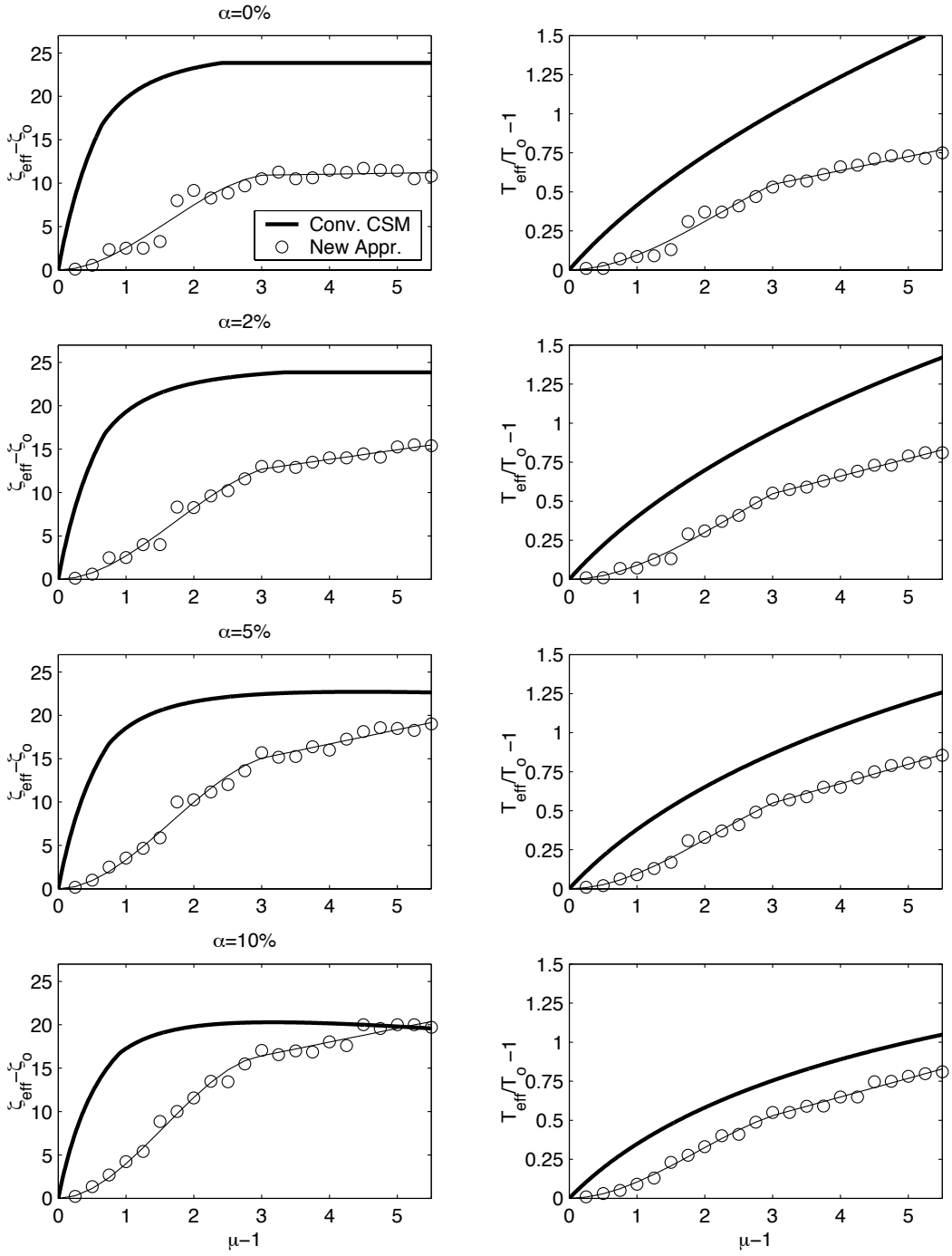

Figure 3.9: Effective parameters for bilinear hysteretic system (BLH) - far-field motions. Conv. CSM - conventional Capacity Spectrum Method, Structural Behavior Type B (ATC-40). New Appr. - new approach implemented in this study. Second slope ratios, α, as indicated

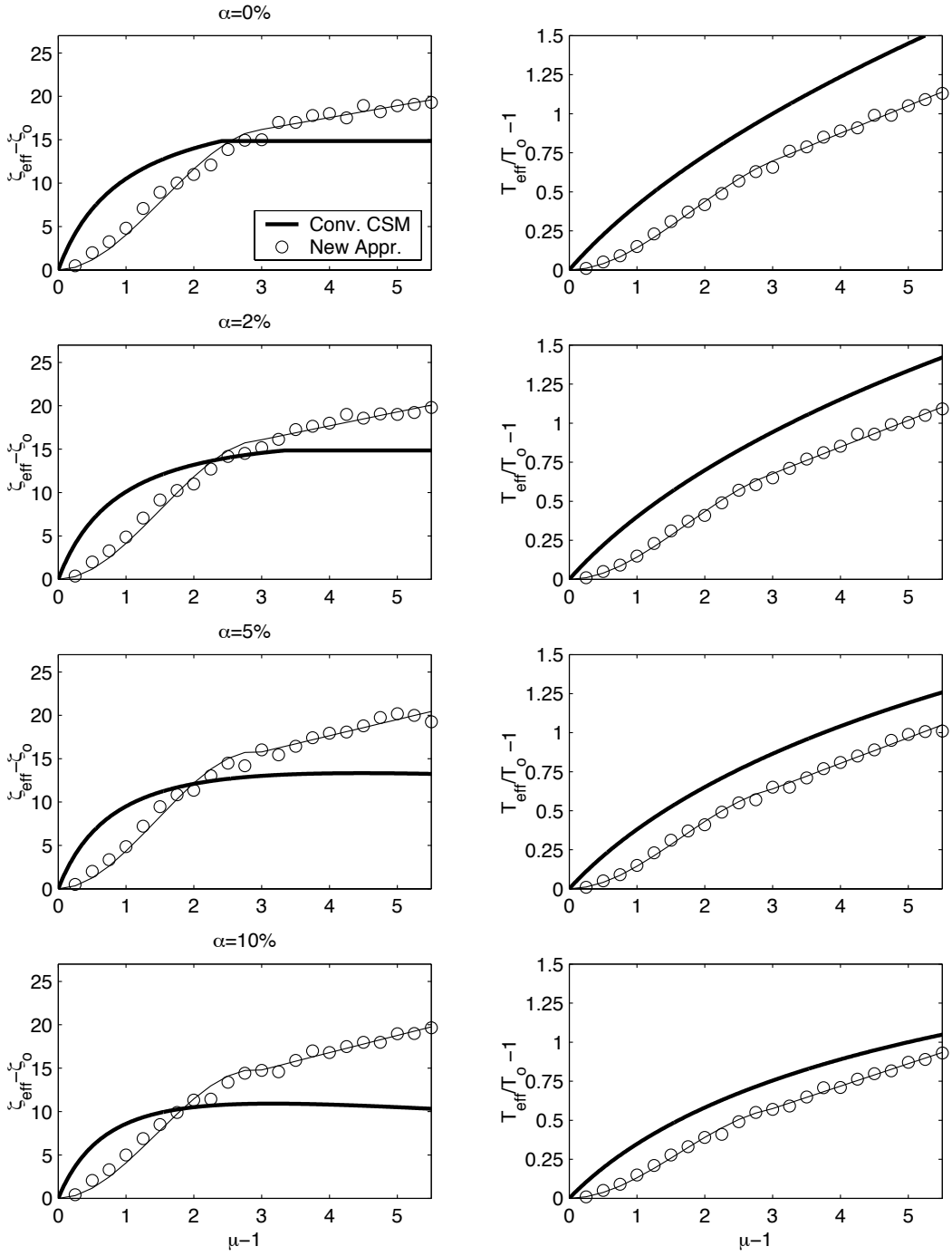

Figure 3.10: Effective parameters for stiffness degrading system (KDEG) - far-field motions. Conv. CSM - conventional Capacity Spectrum Method, Structural Behavior Type C (ATC-40). New Appr. - new approach implemented in this study. Second slope ratios, α, as indicated

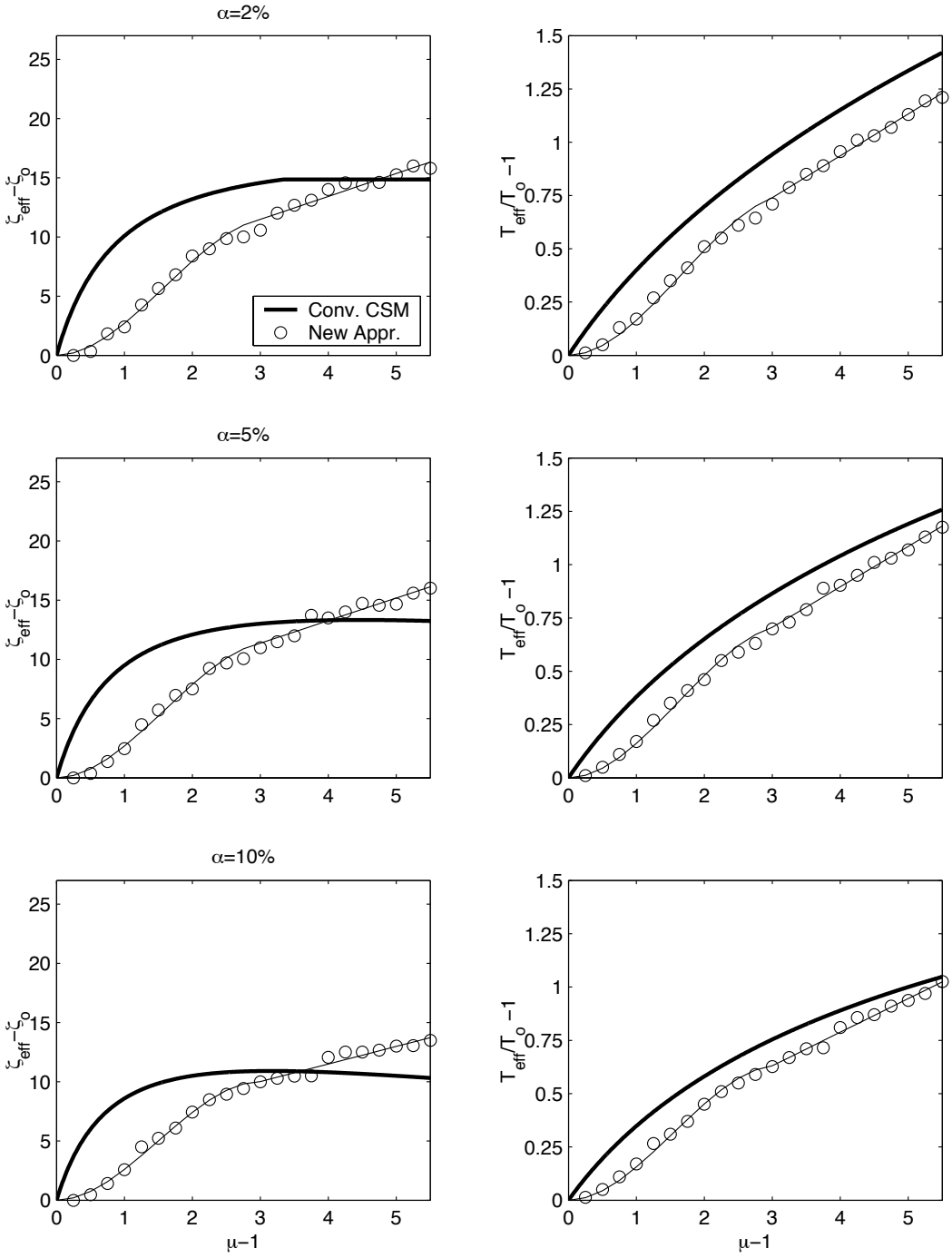

Figure 3.11: Effective parameters for pinching hysteretic system (PIN1) - far-field motions. Conv. CSM - conventional Capacity Spectrum Method, Structural Behavior Type C (ATC-40). New Appr. - new approach implemented in this study. Second slope ratios, α, as indicated

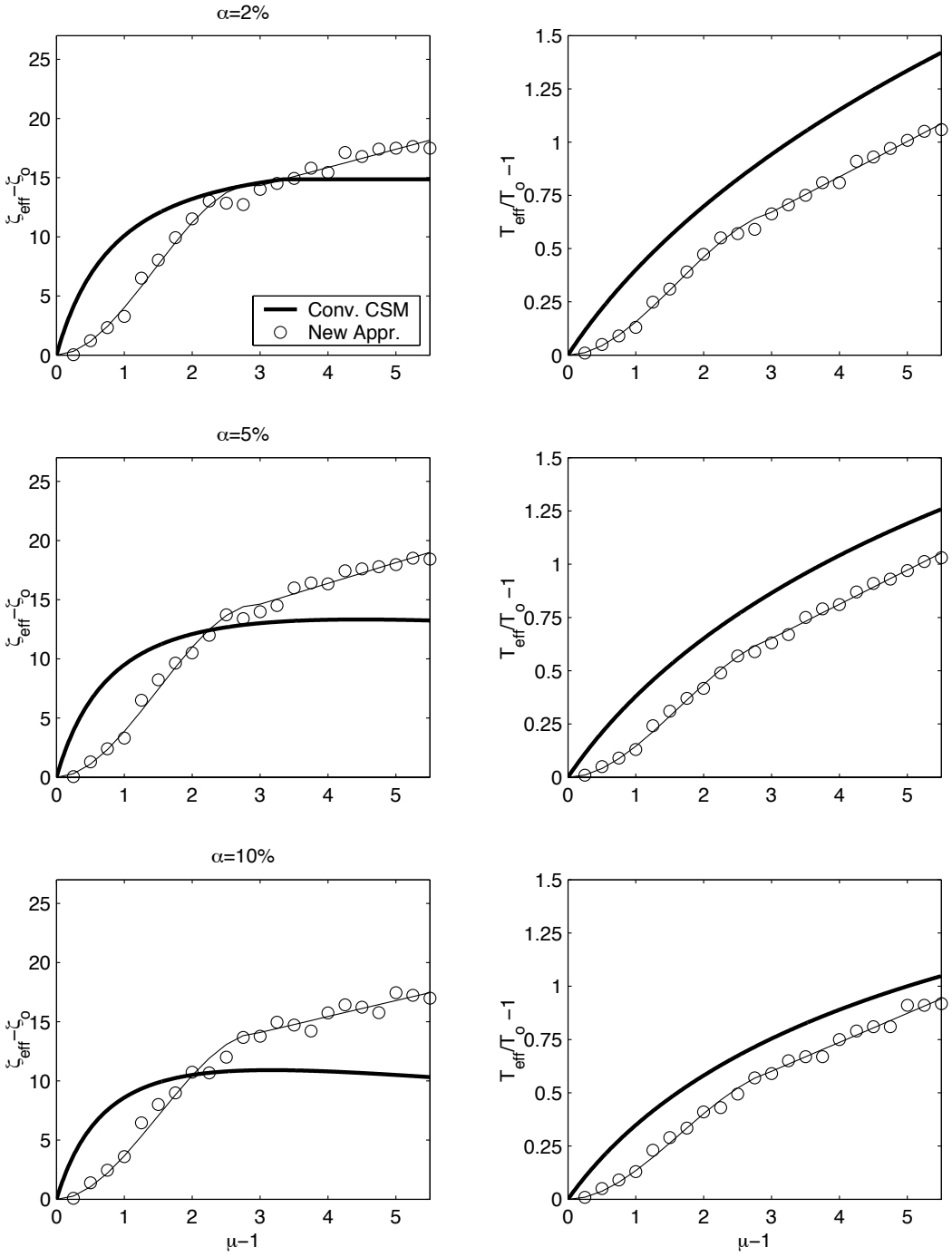

Figure 3.12: Effective parameters for pinching hysteretic system (PIN2) - far-field motions. Conv. CSM - conventional Capacity Spectrum Method, Structural Behavior Type C (ATC-40). New Appr. - new approach implemented in this study. Second slope ratios, α, as indicated

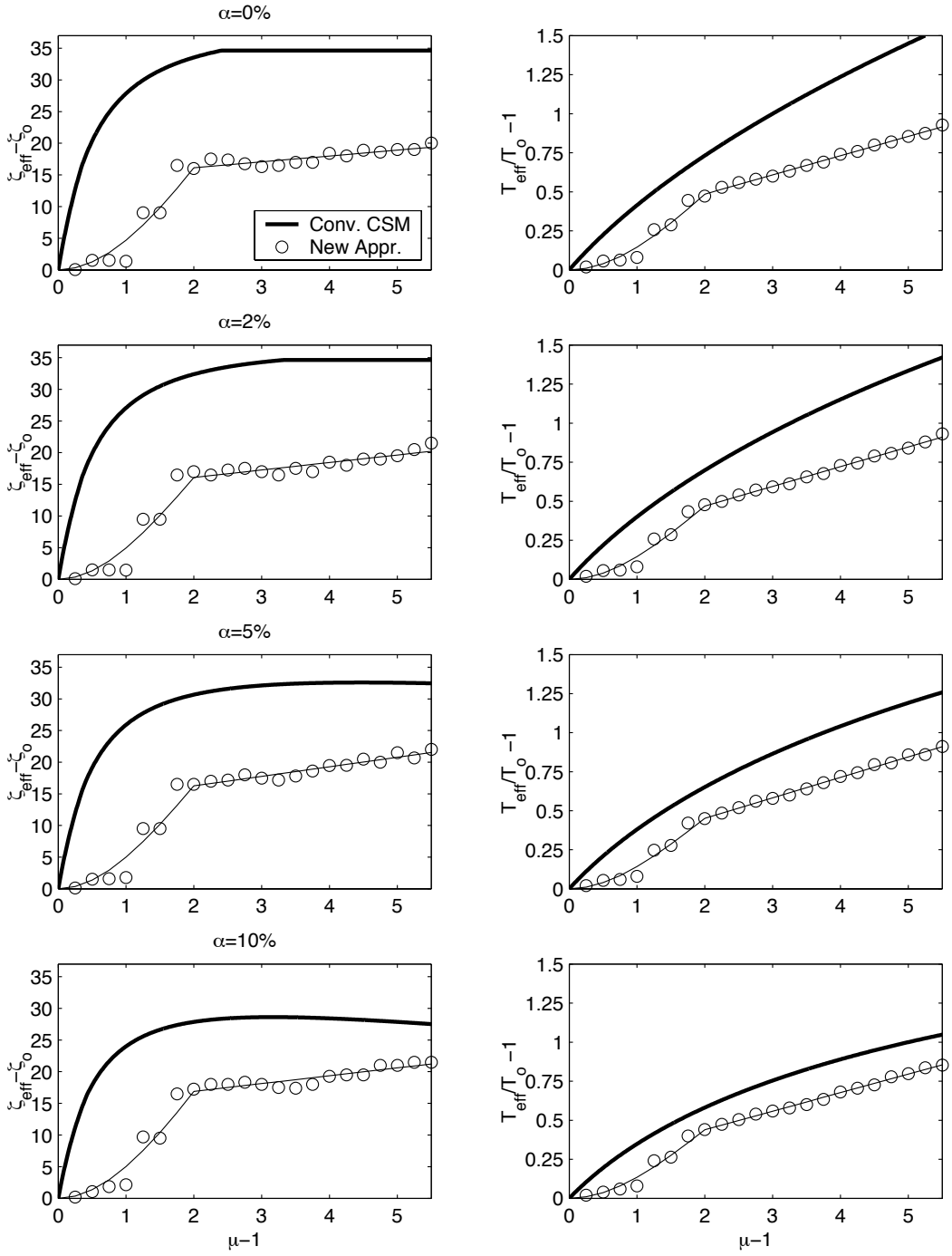

Figure 3.13: Effective parameters for bilinear hysteretic system (BLH) - near-field motions with $T_o/T_p \leq 0.7$. Conv. CSM - conventional Capacity Spectrum Method, Structural Behavior Type A (ATC-40). New Appr. - new approach implemented in this study. Second slope ratios, α, as indicated

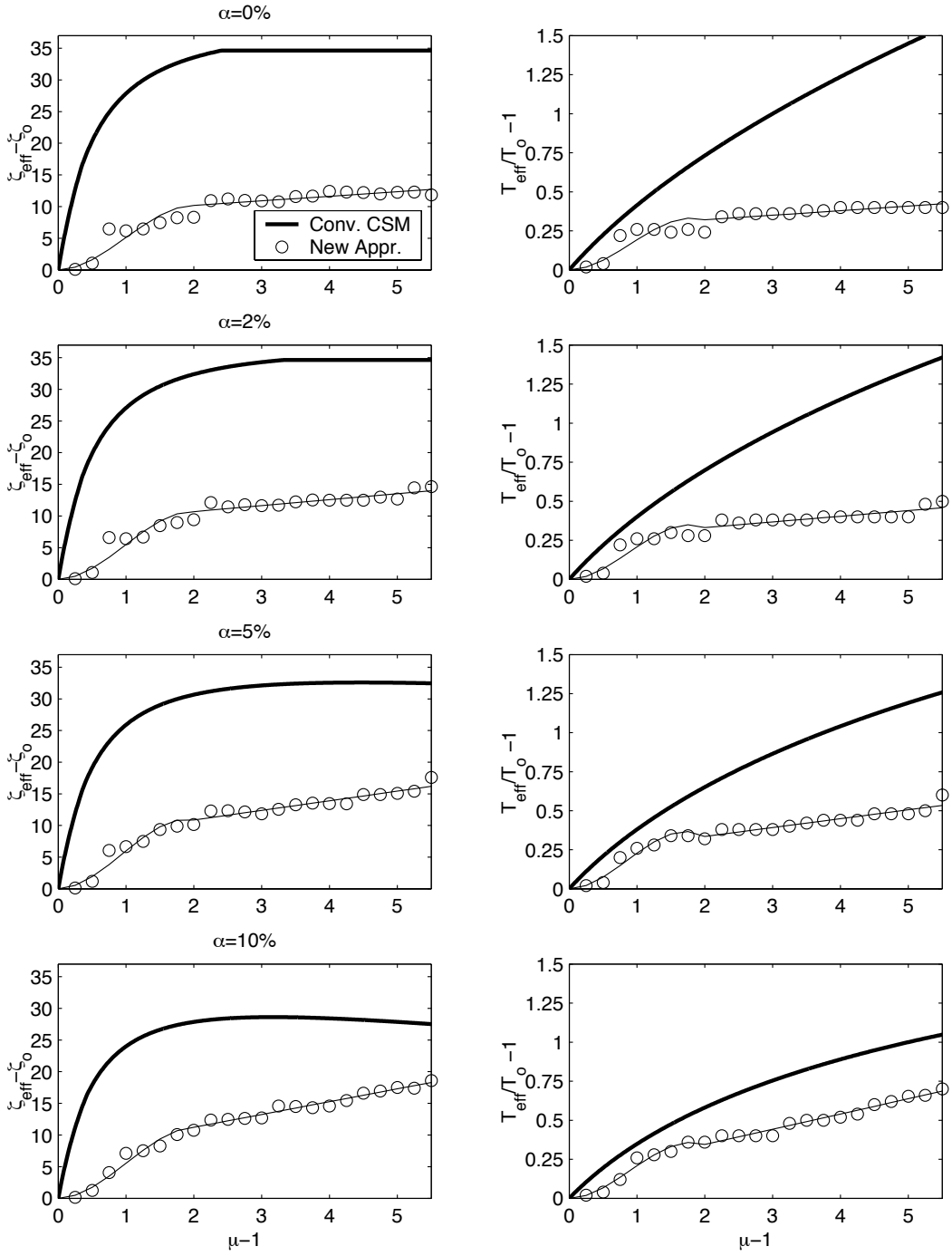

Figure 3.14: Effective parameters for bilinear hysteretic system (BLH) - near-field motions with $0.8 \leq T_o/T_p \leq 1.2$. Conv. CSM - conventional Capacity Spectrum Method, Structural Behavior Type A (ATC-40). New Appr. - new approach implemented in this study. Second slope ratios, α, as indicated

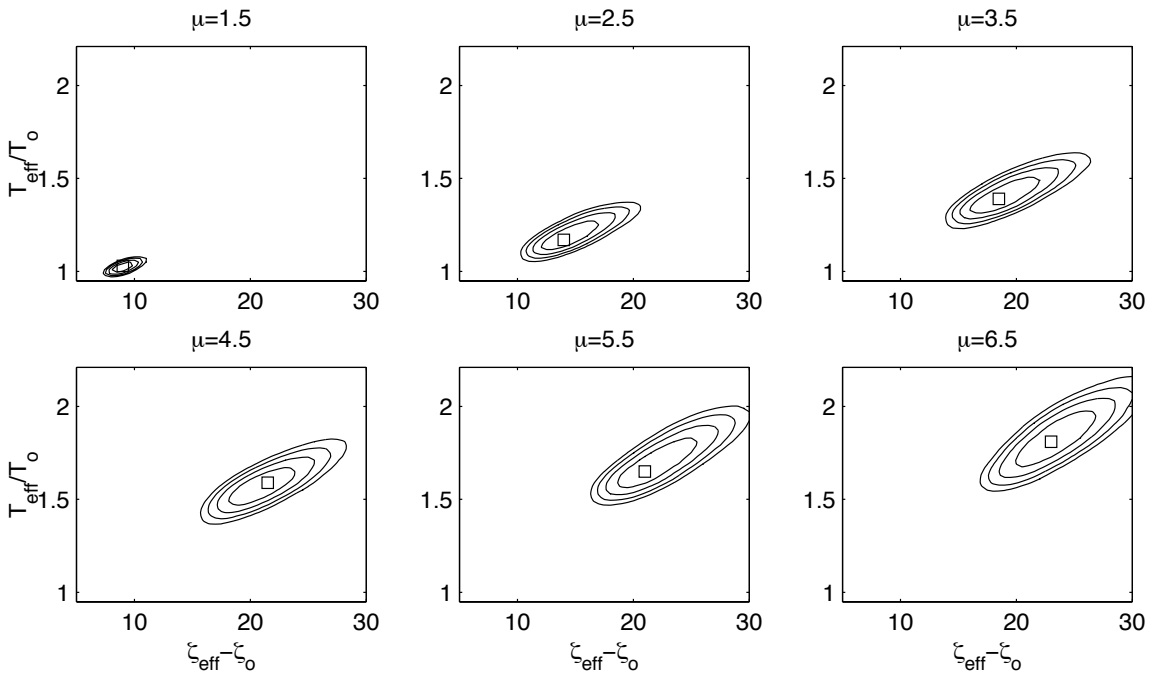

Figure 3.15: Contours of $\mathcal{F}_{EAR_{min}} + 5$, 10, 15 and 20% over a range of ductility values, μ

3.4.1 Analytical Expressions for the Modification Factor, M

Data for the modification factor (Equation 2.16) can be plotted and fit with a curve. The data fitting procedure is the same as in the previous section except that the cubic has been replaced with a quadratic and the linear trend begins at $\mu = 2$.

$$M = 1 + \mathbf{I}(\mu - 1) + \mathbf{J}(\mu - 1)^2 \text{ for } \mu < 2.0 \tag{3.13}$$

$$M = \mathbf{K} + \mathbf{L}(\mu - 1) \text{ for } 2.0 \leq \mu \leq 6.5 \tag{3.14}$$

3.5 Discussion of Effective Linear Parameters

The effective linear parameter equations can only accurately be applied to ductilities less than or equal to 6.5. This range can probably be extended to a ductility of 10 without much sacrifice in accuracy. Beyond a ductility of 10, the equations should

not be used. For application at extremely large ductilities, more analysis must be performed. The linear trend in effective parameters above a ductility of 4 will not continue at extremely large values of ductility.

The analysis has revealed that the secant period is not a good choice for the effective linear period. For each of the different models, second slope ratios and structural period groupings, the secant period clearly overestimates the effective period determined in this new methodology. As mentioned in Section 2.3, an over-prediction of the effective period means that the effective damping value should also be over-predicted.

The modified equivalent viscous damping approach employed in the Capacity Spectrum Method over-estimates the effective damping at lower ductilities in all cases. The effect of this will be seen in the error evaluation (Section 4.3) and discussed further at that time. It was revealed through personal communications that the modification factor, κ, used in the conventional Capacity Spectrum Method was introduced by the authors in an effort to "protect the innocent" from the absurdly high damping values obtained from equivalent viscous damping. For the bilinear model, Figure 3.9, the damping values are still considerably higher than the effective damping values calculated in this study. The stiffness degrading model damping is over-predicted at the lower ductilities and then under-predicted at the higher ductilities. The same is evident for the pinching hysteretic models.

The use of different ranges of initial periods, optimization criterion and nominal damping values will have an effect on the resulting optimal effective linear parameters. The bilinear and strength degrading models with $\alpha = 10\%$ were analyzed to investigate the effects of these parameters.

3.5.1 Effect of Period Range and Optimization Criterion on Effective Linear Parameters

For period ranges T_{all} and T_{short}, four optimization criterion were investigated. The criterion was set for different combinations of a and b in Equation 2.6. The central value (or average) of a and b is denoted "c" and the range of a to b is denoted

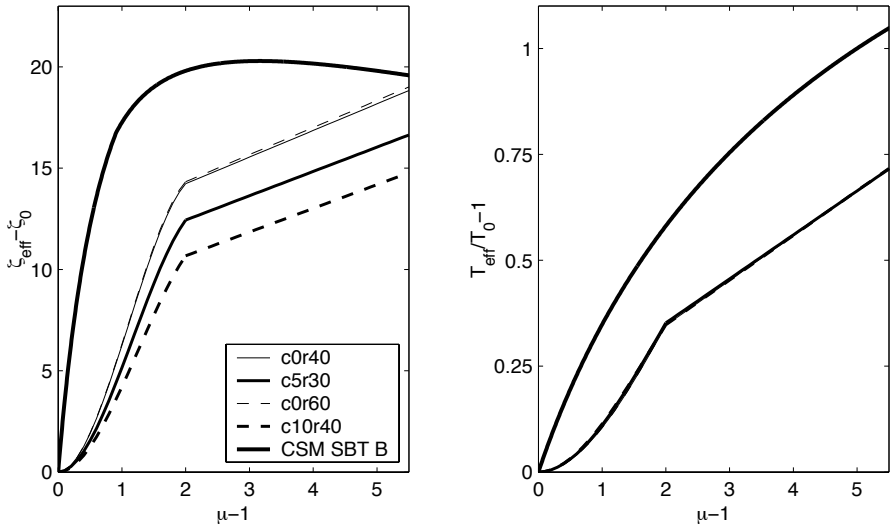

Figure 3.16: Effective parameters for bilinear model (BLH), initial period group T_{all}, second slope ratio (α) of 10% and several optimization criterion - far-field motions

"r". Hence, the combination $a = -20\%$ and $b = 20\%$ will be denoted $c0r40$. Other combinations include $c0r60$, $c10r40$ and the Engineering Acceptability Criterion is $c5r30$. Figures 3.16 and 3.17 show the results of the bilinear and stiffness degrading systems for the T_{all} period range. Figures 3.18 and 3.19 show the results for period range T_{short}.

In all cases, there is minimal change in the effective period as the minimization criteria changes. Referring back to Figure 3.7, the optimal effective period should not change for different criterion because the line of eligible points is roughly horizontal. The effective damping results do change for the different optimization criterion. Criterion with a central value of zero ($c0r40$ and $c0r60$) have higher values of effective damping than the criterion with a mean of 5% ($c5r30$) or a mean of 10% ($c10r40$). As the criterion changes from $c0$ to $c10$, the effective damping drops which reflects the increasing level of conservatism in the criterion.

In all graphs the effective damping for $c0r40$ and $c0r60$ are practically identical. Therefore, the size of the range will not effect the optimal point if the range is larger that some value. Consider the size of the range decreasing. In a limiting case, the criterion $c0r0$ forces the selection of the optimal point to be on the zero mean contour.

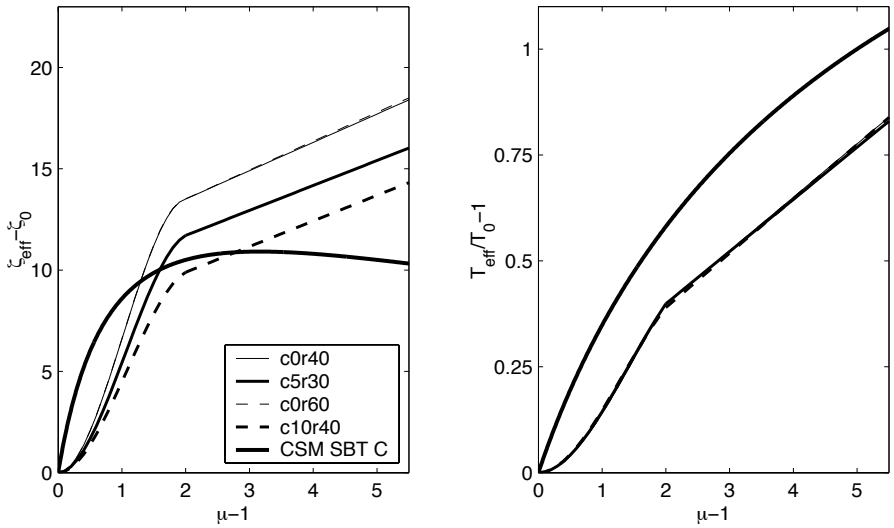

Figure 3.17: Effective parameters for stiffness degrading model (KDEG), initial period group T_{all}, second slope ratio (α) of 10% and several optimization criterion - far-field motions

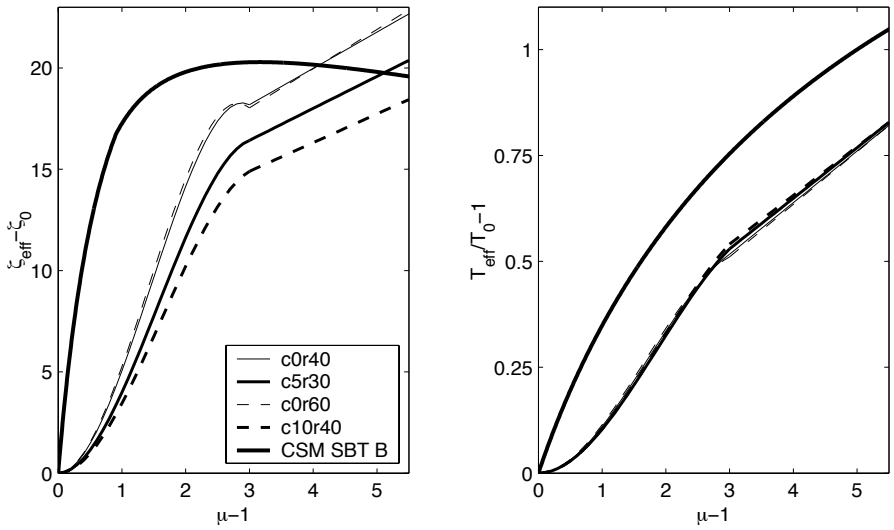

Figure 3.18: Effective parameters for bilinear model (BLH), initial period group $T_{short-low}$, second slope ratio (α) of 10% and several optimization criterion - far-field motions

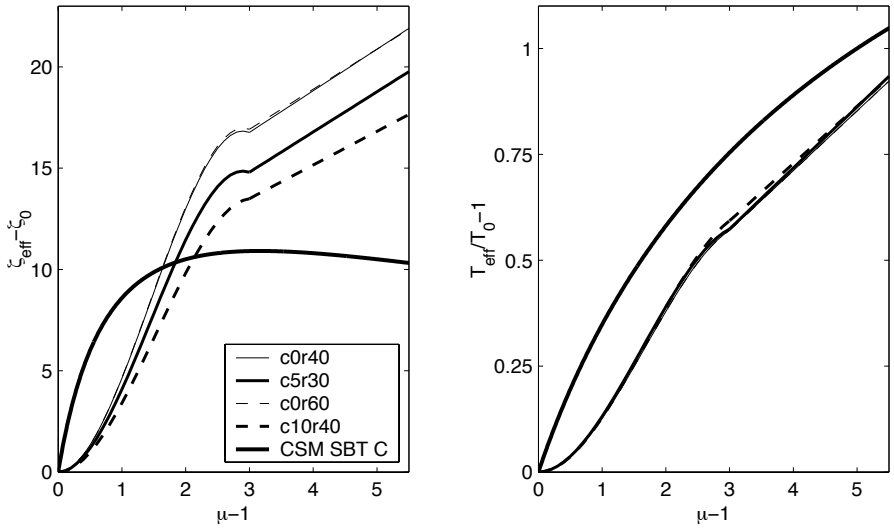

Figure 3.19: Effective parameters for stiffness degrading model (KDEG), initial period group $T_{short-low}$, second slope ratio (α) of 10% and several optimization criterion - far-field motions

Likewise, the criterion $c5r0$ forces the selection of the optimal point to be on the 5% mean contour. The approximate value of the range when it no longer influences the optimal point is about 15. The optimal point for $c5r15$ should roughly be the same as for any criteria with $c5$ and $r > 15$.

Figure 3.20 and 3.21 show the results for bilinear (BLH) and stiffness degrading systems (KDEG) for all five far-field period groupings evaluated with the $c0r40$ criteria. The effective damping is lowest at the higher ductilities for period range T_{long}. In the two figures, several curves cross each other. One observation is that in the effective damping plots, the line for T_{all} is generally between the lines for T_{long} and all the other lines for the lower period groupings. Therefore, the inclusion of longer periods decreases the effective damping.

3.5.2 Effect of Nominal Damping Values (ζ_o) on Effective Linear Parameters

The sensitivity of the analysis to the nominal viscous damping value, ζ_o, has also been explored. All results presented thus far reflect analysis with a single nominal viscous

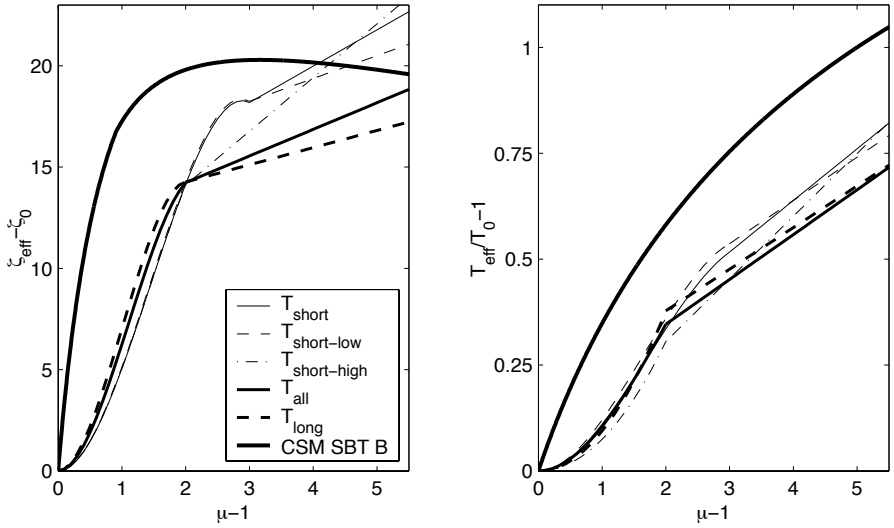

Figure 3.20: Effective parameters for bilinear model (BLH), several initial period groups and a second slope ratio (α) of 10% - far-field motions

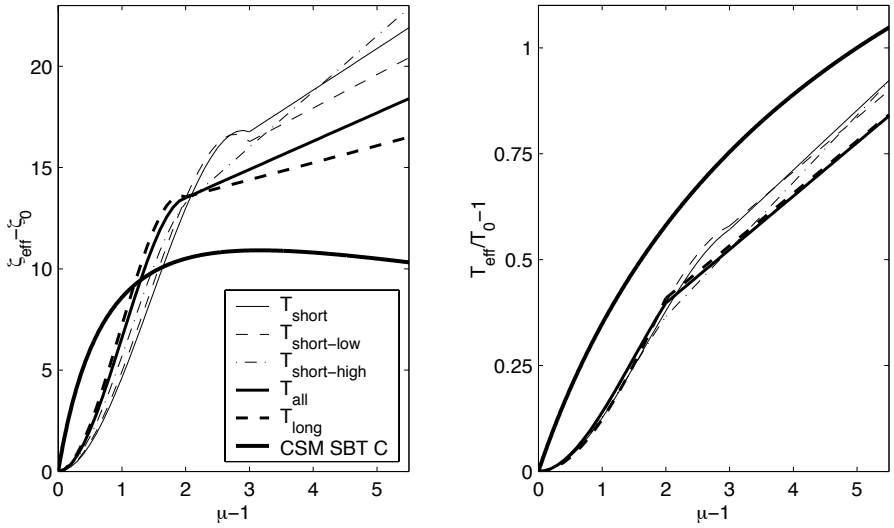

Figure 3.21: Effective parameters for stiffness degrading model (KDEG), several initial period groups and a second slope ratio (α) of 10% - far-field motions

damping value of 5%. The 5% is compared to the exact same analysis for 2% and 7% nominal damping. Figures A.3 and Figure A.4 show the results of the analysis for the bilinear (BLH) and stiffness degrading (KDEG) models. There is little difference in the BLH model while the KDEG model has only a slight difference in the effective damping with $\zeta_o = 2\%$ having a slightly lower effective damping and $\zeta_o = 7\%$ having the highest effective damping. It is concluded that the analysis with $\zeta_o = 5\%$ is a good approximation for the results that would be obtained if 2, 5, and 7% were combined together. Therefore, the effective linear parameter equations developed in this study can be used for any building with a nominal viscous damping of less than or equal to 10% ($\zeta_o \leq 10\%$).

3.6 Conclusions

Based on the procedures to determine the effective linear parameters, the following conclusions can be drawn:

1. The effective parameters obtained in this study accurately reflect the differences in the hysteretic models The effective linear period for the stiffness degrading model is longer than the bilinear model. This is expected because period elongation will occur more quickly in the stiffness degrading model. As ductility increases, less time is spent vibrating at the initial stiffness in the stiffness degrading model (Figure 3.1). A similar observation can be made about the pinching hysteretic systems. The pinching model PIN1 has equivalent parameters with smaller damping than the PIN2 model. This is expected because more energy is dissipated by a cycle of PIN2 hysteresis loop than the PIN1 hysteresis loop as seen in Figure 3.4. Accordingly, PIN2 has equivalent parameters more similar to the bilinear model than PIN1. This is expected because the hysteresis loops for PIN2 are more similar to BLH than PIN1.

2. The third order equation used to fit the lower values of ductility is reasonable. At low ductilities, the percentage difference between the effective parameters

from the new methodology and the conventional Capacity Spectrum Method is greatest. The small increment of ductility used in the present study has revealed important details about the local variations in the effective parameters, especially at the low ductilities. The sensitivity to parameter selection is greatest at the lower ductilities which validates the use of the higher order data fitting equations. Accurate predictions at low ductilities are essential in structural analysis. Unconservative displacement prediction at low ductility values can be the deciding factor to forego a building rehabilitation. The current Capacity Spectrum Method low ductility displacement predictions are unconservative as will be shown in Section 4.3.

3. The trend in the effective parameters as a function of second slope value (α) from the new methodology are different from the conventional Capacity Spectrum Method. In the conventional Capacity Spectrum Method formulation, both the effective period and effective damping decrease as α increases. The largest value of each parameter occurs at $\alpha = 0\%$. Results from the new methodology do not show this trend for low values of α. The bilinear model reflects a slight increase in effective damping as α goes from 0% to 10%. This can be explained by the wandering effect found in elasto-plastic systems (BLH with $\alpha = 0\%$) as discussed by Paparizos and Iwan [59]. Bilinear hysteretic systems with a zero second slope ratio exhibit a long period "wandering" motion when excited by earthquake motions containing frequencies near the effective natural frequency of the system. A non-zero second slope ratio works as a centering mechanism that gives the system some memory as to its original equilibrium position. The prediction for the bilinear system with small alpha values less reliable compared to increased alpha values.

   For all the hysteretic models used in this study, a fundamental requirement is that the effective linear parameters *must* approach zero as the second slope ratio, α, approaches 100% (the elastic case). Indeed that is the trend as seen in Figure 3.22. The case of $\alpha = 60\%$ is graphed for each hysteretic system.

4. For near-field motions, the difference between the effective parameters obtained for period groups $T_o/T_p \leq 0.7$ and $0.8 \leq T_o/T_p \leq 1.2$ for both the bilinear (Figures 3.13 and 3.14) and stiffness degrading models (Figures A.1 and A.2) is substantial. The effective period and effective damping values for the lower period range are higher than for the second period range. This reflects the dynamic amplification of systems with initial linear periods near the pulse period of the ground motion. Comparing bilinear to stiffness degrading for the period range $T_o/T_p \leq 0.7$ reveals similar effective period values but the stiffness degrading model has lower effective damping. Over the period range $0.8 \leq T_o/T_p \leq 1.2$, both models have similar effective damping values while the KDEG model has longer effective period values. This is expected in relation to the hysteretic properties of the bilinear and stiffness degrading systems. The stiffness degrading model should have lower effective damping which increases displacement response and a longer effective period reflects the degraded stiffness.

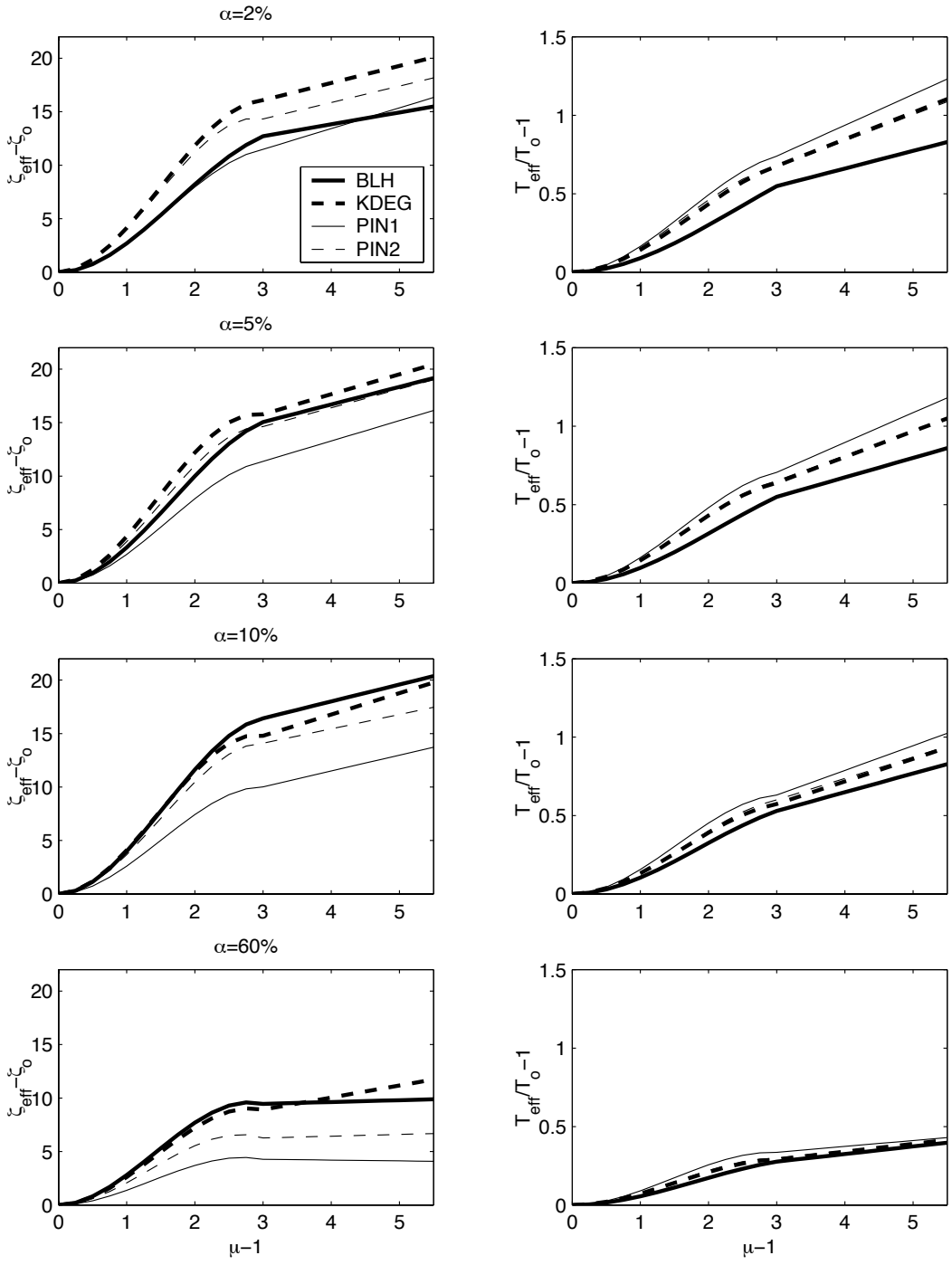

Figure 3.22: Summary of analytical expressions for effective period and damping for bilinear (BLH), stiffness degrading (KDEG) and pinching hysteretic models (PIN1 and PIN2) - far-field motions

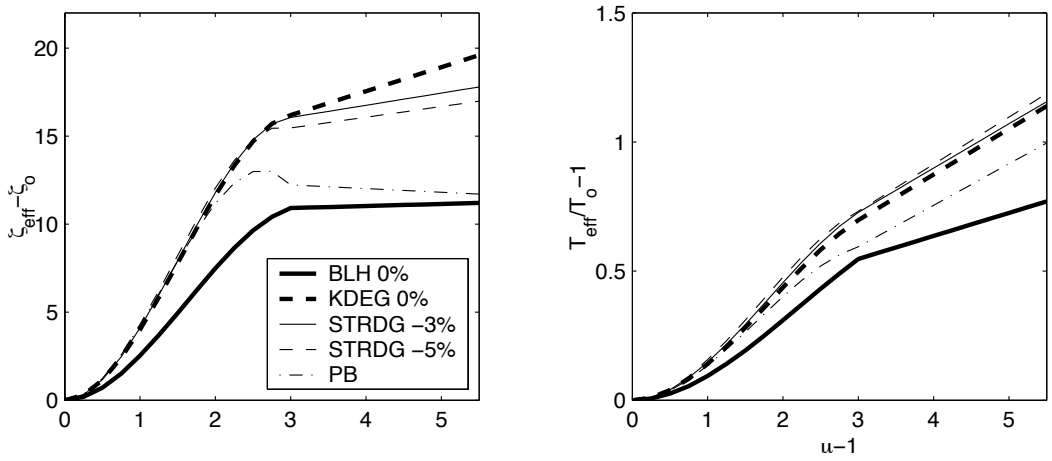

Figure 3.23: Summary of analytical expressions for effective period and damping effective for bilinear with second slope ratio of 0% (BLH 0%), stiffness degrading (KDEG 0%), strength degrading (STRDG -3% and -5%) and pushover backbone hysteretic model (PB) - far-field motions

Model	T Range	α	**A**	**B**	**C**	**D**
BLH	T_{short}	0%	3.1922	−0.6598	10.5687	0.1156
BLH	T_{short}	2%	3.3338	−0.6405	9.3792	1.1101
BLH	T_{short}	5%	4.1504	−0.8260	10.1243	1.6428
BLH	T_{short}	10%	5.0731	−1.0826	11.6899	1.5791
KDEG	T_{short}	0%	5.1261	−1.1090	12.1052	1.3622
KDEG	T_{short}	2%	5.3031	−1.1722	11.2724	1.6023
KDEG	T_{short}	5%	5.6420	−1.2962	10.1820	1.8661
KDEG	T_{short}	10%	5.3056	−1.2203	8.8425	1.9861
STRDG	T_{short}	−3%	5.2749	−1.1635	13.9824	0.6924
STRDG	T_{short}	−5%	5.6014	−1.2944	13.6407	0.6080
PIN1	T_{short}	2%	3.4226	−0.7156	5.6695	1.9379
PIN1	T_{short}	5%	3.3888	−0.7083	5.6711	1.9015
PIN1	T_{short}	10%	3.3443	−0.7438	5.5659	1.4835
PIN2	T_{short}	2%	5.2207	−1.2100	9.7038	1.5378
PIN2	T_{short}	5%	4.9926	−1.1225	9.3702	1.7518
PIN2	T_{short}	10%	4.7203	−1.0514	10.0604	1.3451
PB	T_{short}	NA	5.6683	−1.4363	12.8666	−0.2112

Model	T Range	α	**E**	**F**	**G**	**H**
BLH	T_{short}	0%	0.1108	−0.0167	0.2794	0.0892
BLH	T_{short}	2%	0.1034	−0.0142	0.2107	0.1125
BLH	T_{short}	5%	0.1145	−0.0178	0.1777	0.1240
BLH	T_{short}	10%	0.1262	−0.0224	0.1713	0.1194
KDEG	T_{short}	0%	0.1725	−0.0317	0.1673	0.1767
KDEG	T_{short}	2%	0.1756	−0.0335	0.1637	0.1708
KDEG	T_{short}	5%	0.1809	−0.0366	0.1472	0.1640
KDEG	T_{short}	10%	0.1652	−0.0338	0.1419	0.1440
STRDG	T_{short}	−3%	0.1801	−0.0331	0.2128	0.1716
STRDG	T_{short}	−5%	0.1950	−0.0379	0.1843	0.1825
PIN1	T_{short}	2%	0.2057	−0.0412	0.1507	0.1963
PIN1	T_{short}	5%	0.2034	−0.0417	0.1367	0.1898
PIN1	T_{short}	10%	0.1990	−0.0430	0.1581	0.1575
PIN2	T_{short}	2%	0.1962	−0.0405	0.1730	0.1660
PIN2	T_{short}	5%	0.1820	−0.0365	0.1704	0.1604
PIN2	T_{short}	10%	0.1680	−0.0338	0.1923	0.1361
PB	T_{short}	NA	0.1691	−0.0344	0.1115	0.1609

Table 3.2: Coefficients for effective linear parameters, Equations 3.5 through 3.8 - far-field motions

Model	T_o/T_p	α	**A**	**B**	**C**	**D**
BLH	≤ 0.7	0%	5.3509	−0.6585	14.2863	0.9247
BLH	≤ 0.7	2%	5.8839	−0.9319	13.7141	1.1830
BLH	≤ 0.7	5%	5.9374	−0.9363	13.2440	1.5075
BLH	≤ 0.7	10%	5.8275	−0.8033	14.4054	1.2391
BLH	$0.8 - 1.2$	0%	7.6765	−2.5650	8.7491	0.7183
BLH	$0.8 - 1.2$	2%	8.1399	−2.8236	8.8092	0.9407
BLH	$0.8 - 1.2$	5%	9.2608	−3.2721	7.8295	1.5184
BLH	$0.8 - 1.2$	10%	8.2566	−2.7253	7.1819	2.0212
KDEG	≤ 0.7	0%	6.0326	−1.4557	8.4089	2.0378
KDEG	≤ 0.7	2%	4.5814	−0.7036	8.7527	1.9719
KDEG	≤ 0.7	5%	4.7285	−0.7445	9.3875	1.7854
KDEG	≤ 0.7	10%	4.2641	−0.4745	10.5459	1.3574
KDEG	$0.8 - 1.2$	0%	6.3745	−1.9620	5.8949	1.9534
KDEG	$0.8 - 1.2$	2%	6.3093	−1.9220	5.8588	2.0013
KDEG	$0.8 - 1.2$	5%	6.4361	−2.0071	5.6345	2.0266
KDEG	$0.8 - 1.2$	10%	6.3825	−2.0085	5.3001	2.0809

Model	T_o/T_p	α	**E**	**F**	**G**	**H**
BLH	≤ 0.7	0%	0.1703	−0.0245	0.2391	0.1230
BLH	≤ 0.7	2%	0.1741	−0.0284	0.2170	0.1260
BLH	≤ 0.7	5%	0.1714	−0.0293	0.1887	0.1311
BLH	≤ 0.7	10%	0.1599	−0.0251	0.2010	0.1189
BLH	$0.8 - 1.2$	0%	0.3052	−0.1125	0.2616	0.0294
BLH	$0.8 - 1.2$	2%	0.3329	−0.1251	0.2586	0.0363
BLH	$0.8 - 1.2$	5%	0.3717	−0.1440	0.2215	0.0569
BLH	$0.8 - 1.2$	10%	0.3307	−0.1222	0.1497	0.0976
KDEG	≤ 0.7	0%	0.2124	−0.0484	0.1269	0.1676
KDEG	≤ 0.7	2%	0.1827	−0.0341	0.1394	0.1595
KDEG	≤ 0.7	5%	0.1834	−0.0354	0.1550	0.1475
KDEG	≤ 0.7	10%	0.1700	−0.0300	0.1941	0.1228
KDEG	$0.8 - 1.2$	0%	0.2909	−0.0918	0.1905	0.1191
KDEG	$0.8 - 1.2$	2%	0.2932	−0.0942	0.1648	0.1274
KDEG	$0.8 - 1.2$	5%	0.2844	−0.0909	0.1603	0.1249
KDEG	$0.8 - 1.2$	10%	0.2793	−0.0911	0.1500	0.1194

Table 3.3: Coefficients for effective linear parameters, Equations 3.9 through 3.12 - near-field motions

Model	T Range	α	**I**	**J**	**K**	**L**
BLH	T_{short}	0%	−0.8114	0.4133	0.6247	−0.0229
BLH	T_{short}	2%	−0.7767	0.3769	0.6028	−0.0026
BLH	T_{short}	5%	−0.7571	0.3889	0.6190	0.0127
BLH	T_{short}	10%	−0.7053	0.3612	0.6206	0.0353
KDEG	T_{short}	0%	−0.7614	0.4286	0.6557	0.0114
KDEG	T_{short}	2%	−0.7452	0.4254	0.6611	0.0192
KDEG	T_{short}	5%	−0.7208	0.4208	0.6715	0.0284
KDEG	T_{short}	10%	−0.6799	0.4124	0.6988	0.0336

Table 3.4: Coefficients for modification factors, Equations 3.13 and 3.14 **-** far-field motions

Chapter 4

Validation of the Effective Linear Parameters

4.1 Introduction

Evaluation of the errors associated with the use of effective linear parameters will be done on two levels. The first level will compare the displacement of the linear system obtained with the effective period and damping at the inelastic system response ductility to the inelastic system displacement for a given ground excitation. This will be referred to as the Displacement Response Error. The second level will compare the displacement of the linear system obtained with the effective period and damping at the Performance Point ductility to the inelastic system displacement for a given ground excitation. This will be referred to as the Performance Point Error.

The Performance Point Error is the key evaluator of the effective linear parameters within the framework of Performance-Based Engineering. In engineering design, the response ductility is an unknown quantity. Therefore, the Displacement Response Error is not directly applicable to Performance-Based Engineering. The Performance Point will be predicted by the Capacity Spectrum Method. The Performance Point Error directly evaluates the accuracy of the Performance Point prediction. All errors will be calculated for both the effective parameters developed from the new methodology and the effective parameters used in conventional Capacity Spectrum Method. The conventional Capacity Spectrum Method uses the secant period as the effective

linear period (Equation 1.25) and the effective damping from Equation 1.28.

Two procedures are proposed to calculate the Performance Point ductility for a bilinear capacity curve and given ground excitation. These procedures were developed from a research perspective. A procedure more appropriate for application in structural design is provided in Section 5.1.

4.2 Displacement Response Error

The effective linear parameter equations are evaluated by using the predicted linear displacement for the ductility of the inelastic system. Define the Displacement Response Error as the ratio of the difference between the linear displacement at the effective period and damping and the inelastic displacement to the inelastic displacement

$$\epsilon_{D_{eff}}(\alpha, \mu, \text{HYST}) = \frac{D_{lin}(T_{eff}(T_o, \alpha, \mu), \zeta_{eff}(\zeta_o, \alpha, \mu)) - D_{inel}(T_o, \zeta_o, \alpha, \mu, \text{HYST})}{D_{inel}(T_o, \zeta_o, \alpha, \mu, \text{HYST})} \tag{4.1}$$

The Displacement Response Error is graphically represented in Figure 4.1.

The maximum inelastic displacement may be rewritten as the yield displacement times ductility

$$D_{inel}(T_o, \zeta_o, \alpha, \mu, \text{HYST}) = \mu D_y(T_o, \zeta_o, \alpha, \mu, \text{HYST}) \tag{4.2}$$

Therefore, define the effective ductility as the linear displacement for the effective period and damping at the ductility of the inelastic system divided by the yield displacement

$$\mu_{eff}(T_{eff}(T_o, \alpha, \mu), T_o, \zeta_{eff}(T_o, \alpha, \mu) = \frac{D_{lin}(T_{eff}(T_o, \alpha, \mu), \zeta_{eff}(\zeta_o, \alpha, \mu))}{D_y(T_o, \zeta_o, \alpha, \mu, \text{HYST})} \tag{4.3}$$

Substituting Equations 4.3 and 4.2 into Equation 4.1, the Displacement Response Error may now be alternatively expressed as the ratio of the difference between the

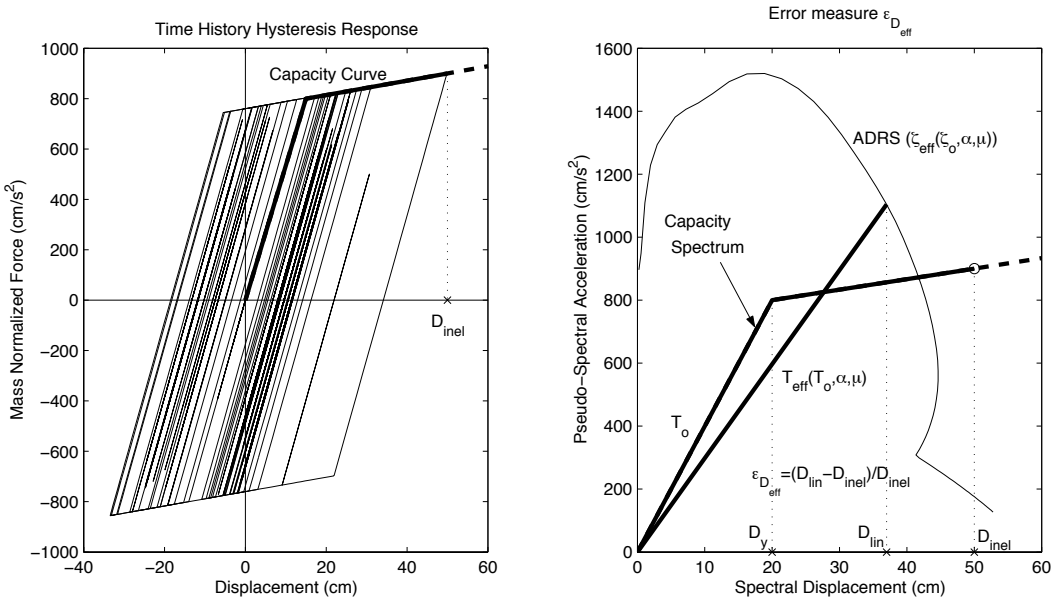

Figure 4.1: Combining the time history hysteretic response (left) with the displacement prediction from the effective linear parameters (right) to form the Displacement Response Error, $\epsilon_{D_{eff}}$

effective ductility and the response ductility to the response ductility

$$\epsilon_{D_{eff}}(\alpha, \mu, \text{HYST}) = \frac{\mu_{eff}(T_{eff}(T_o, \alpha, \mu), T_o, \zeta_{eff}(T_o, \alpha, \mu), \zeta_o, \alpha, \mu, \text{HYST}) - \mu}{\mu} \quad (4.4)$$

Results for the far-field ground motions are presented in Table 4.1 while results for the near-field ground motions are presented in Tables D.1 and D.2. These results are presented as a mean and standard deviation of the distribution over all the ductility values combined. In all cases the "NEW" effective linear parameters developed in this study have a mean value closer to zero and often substantially smaller standard deviation.

Figures B.1 through B.3 show the results for the bilinear hysteretic model (BLH) as a surface plot of ductility versus second slope ratio for both far-field and near-field ground motions. For the far-field motions, results show a big improvement in the low ductility range for all hysteretic models in the range of errors from -10% to 20% and also from -20% to 40%. At the lower ductilities is where the effective damp-

ing equations from the new methodology and the conventional Capacity Spectrum Method are most different, as mentioned in Section 3.5. This is where the biggest improvement has occurred in the Displacement Response Error. Similar observations are made for the stiffness degrading and pinching hysteretic models but their color contour plots are omitted.

4.3 Performance Point Error

The Displacement Response Error ($\epsilon_{D_{eff}}$) required the use of the time history ductility. In engineering design, the time history ductility will be an unknown quantity. Define the Performance Point Error as the ratio of the difference between the linear displacement at the effective period and damping evaluated at the Performance Point ductility and the inelastic displacement to the inelastic displacement

$$\epsilon_{D_{PP}}(\alpha, \mu, \text{HYST}) = \frac{D_{lin}(T_{eff}(T_o, \alpha, \mu_{PP}), \zeta_{eff}(\zeta_o, \alpha, \mu_{PP})) - D_{inel}(T_o, \zeta_o, \alpha, \mu, \text{HYST})}{D_{inel}(T_o, \zeta_o, \alpha, \mu, \text{HYST})} \tag{4.5}$$

Similar to the formulation of the Displacement Response Error, the Performance Point Error may be alternatively expressed as

$$\epsilon_{D_{PP}}(\alpha, \mu, \text{HYST}) = \frac{\mu_{PP}(T_{eff}(T_o, \alpha, \mu_{PP}), T_o, \zeta_{eff}(T_o, \alpha, \mu_{PP}), \zeta_o, \alpha, \mu, \text{HYST}) - \mu}{\mu} \tag{4.6}$$

where μ_{PP} is the Performance Point ductility.

The procedures used to calculate the Performance Point employ an incremental search algorithm. The search starts at a ductility of 40 and decreases at an increment of 0.1 ending at a ductility of 1.1. The capacity spectrum is assumed to have infinite ductility capacity. Although it was stated in Section 3.5 that the effective linear parameter equations should only be used for ductilities less than 10, the extension to a ductility of 40 was done in this evaluation because an inaccurate large answer is more important than a non-convergent answer. The Performance Point Errors distributions

will not be analyzed by a mean value and standard deviation because the distributions are not Normal. Extremely large values need not be accurate because they are already outside of a desired range of values near zero. In this specific evaluation, it is more important to extend the analysis to high ductilities instead of being recorded as non-convergent cases. For other evaluations, extending the equations to large values of ductility may not be acceptable.

There is no guarantee that there will be a Performance Point for a given system and ground excitation. When no Performance Point is determined, the case is recorded as non-convergent. There are several possible explanations for a non-convergent case but it is better explained within the context of the New Performance Point Solution Procedure in Section 5.1.

There is also a possibility of multiple Performance Points for a given system and ground motion. When a multi-valued case is encountered, the most conservative prediction for the Performance Point is recorded and the case is recorded as multi-valued.

4.3.1 Procedure A

Calculation of the Performance Point will be done by tracking the intersection points of the capacity curve and the family of MADRS associated with the range of ductilities from 1.1 to 40. The ductilities associated with the demand spectra will be the demand ductilities, μ_{demand}. Refer to Figure 4.2. A single demand spectrum will most likely result in one or more intersection with the capacity spectrum. These intersections occur at a displacement which when divided by the yield displacement result in the capacity ductility, $\mu_{capacity}$. For a family of demand spectra (from a range of demand ductilities), a Locus of Combinations of $\mu_{capacity}$, μ_{demand} will result. The Performance Point ductility is the ductility at which the Locus of Combinations crosses the line where the demand and capacity ductilities are equal.

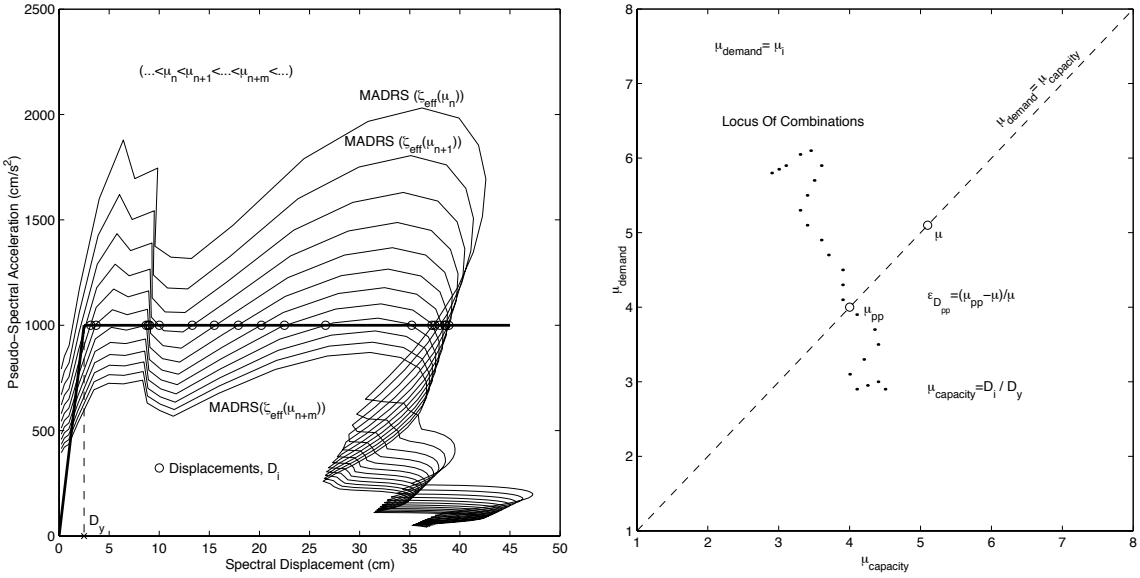

(a) Determining intersections of a capacity curve and a family of Modified Acceleration-Displacement Response Spectra (MADRS)

(b) Determining a Performance Point from a Locus of Combinations

Figure 4.2: Performance Point solution scheme - procedure A

4.3.2 Procedure B

A solution procedure that does not require the calculation of the MADRS is also available. Procedure B is shown pictorially in Figure 4.3. The demand ductilities are inserted directly into the effective parameter equations. The response of each linear system is calculated and divided by the yield displacement of the inelastic system, resulting in a range of capacity ductilities. The Performance Point ductility is the ductility at which the Locus of Combinations crosses the line where the demand and capacity ductilities are equal. In this approach the Performance Point ductility can be expressed as the solution to the following transcendental equation

$$\mu_{pp} = \frac{D_{lin}(T_{eff}(T_o, \alpha, \mu_{pp}), \zeta_{eff}(\zeta_o, \alpha, \mu_{pp}))}{D_y(T_o, \zeta_o, \alpha, \mu)} \tag{4.7}$$

The relationship between μ_{eff} (Equation 4.3) and the Locus of Combinations from this procedure is shown in Figure 4.3(b). The figure reflects a case where $\epsilon_{D_{pp}} < \epsilon_{D_{eff}}$ but this is by no means guaranteed to occur in every case.

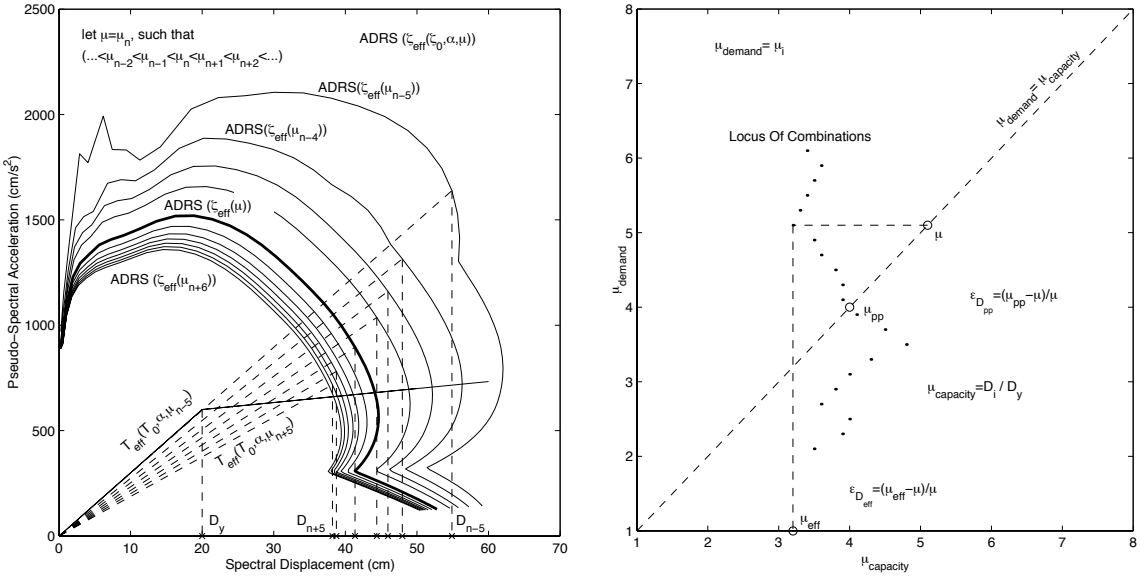

(a) Incrementally applying effective linear parameters for a capacity spectrum and earthquake time history

(b) Determining a Performance Point from a Locus of Combinations

Figure 4.3: Performance Point solution scheme - procedure B

4.3.3 Problems Associated with $\alpha < 0$

The secant period (Equation 1.25) will approach infinity for large ductilities and a negative second slope ratio, α. Consequently, the modification factor used to construct the MADRS approaches infinity (Equation 2.16). Procedure A, which uses the modification factor, is limited in the largest value of ductility at which the incremental search can begin. Procedure B, which uses the effective period, experiences this problem when evaluating the conventional Capacity Spectrum Method because the secant period is the effective period in the conventional Capacity Spectrum Method. For these cases,the incremental search began at a ductility of 20.

4.3.4 Comparing Procedure A and B

For procedures A and B, the Loci of Combinations are almost completely different. The only points the Loci have in common are the Performance Points as illustrated in Figure 4.4. However, there is another important difference between procedures

A and B relating to the Locus of Combinations. The Locus from procedure A can be multiple-valued in *both* μ_{demand} and $\mu_{capacity}$. An example of this is shown in Figure 4.5. A single μ_{demand} value can have multiple $\mu_{capacity}$ values and vice verse.

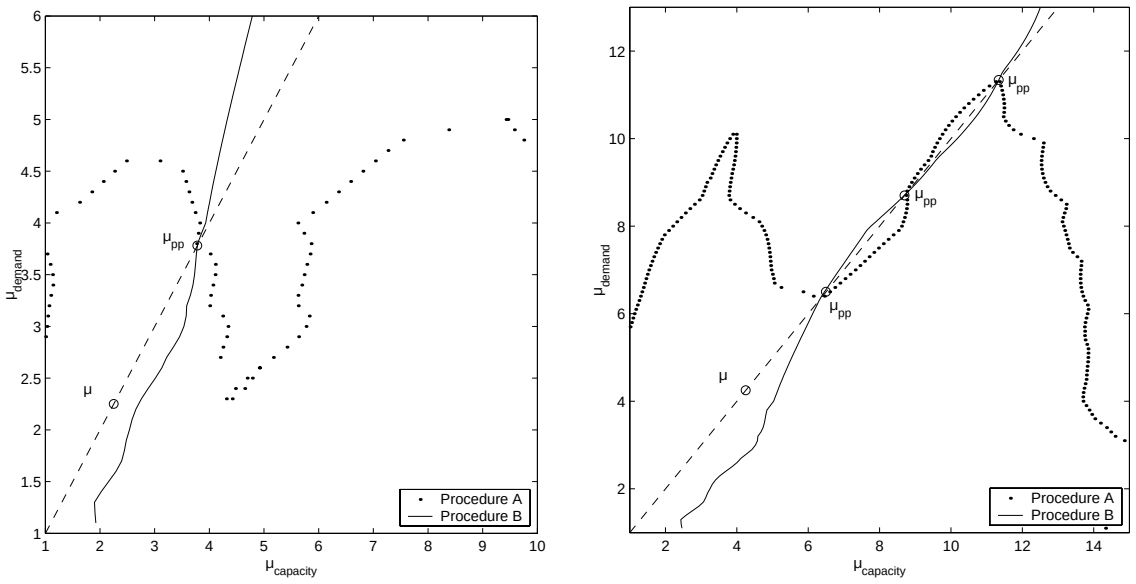

(a) Locus of Combinations from procedures A and B - single-valued case

(b) Locus of Combinations from procedures A and B - multi-valued case

Figure 4.4: Comparing Locus of Combinations - procedures A and B

Procedure B is formulated such that it is possible to be multi-valued only in $\mu_{capacity}$. Each μ_{demand} will have a single $\mu_{capacity}$ while a single value of $\mu_{capacity}$ may have several μ_{demand} values associated with it. This has implications when searching through the Locus of Combinations for the Performance Point. The double multi-valued nature of procedure A makes it difficult to implement a reliable search algorithm while procedure B requires a simple search algorithm. Procedure A creates a Locus of Combinations that cannot be sorted into ascending or descending order because of the possible double multi-valueness. The Loci from procedure A in Figure 4.5 are plotted as discrete points and not lines for this reason.

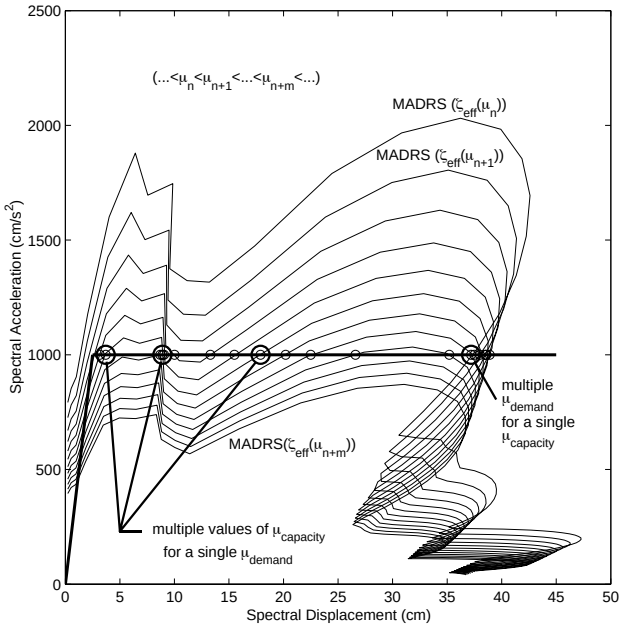

Figure 4.5: Example of the possible multi-valued nature of both μ_{demand} and $\mu_{capacity}$ for procedure A

4.4 Discussion of Performance Point Error Results

Performance Point Error results for the bilinear (BLH) model subjected to both far-field and near-field motions are shown in Figures 4.6 through 4.8. The stiffness degrading (KDEG) and pinching models (PIN1 and PIN2) far-field analysis results are shown in Figures C.1 through C.3. Results for far-field motions are also presented in Tables 4.1 through 4.3 and near-field results in Tables D.1 through D.6.

The incremental search method employed in procedures A and B started at a ductility of 40 and choosing the most conservative performance point prediction in any multi-valued case will skew the error statistics to the positive side. The distribution of the Performance Point statistics is not Normally distributed. The presentation of the results in terms of mean and standard deviation values averaged over the entire ductility range will be highly effected by the large outliers present in the study. Looking at the data in terms of errors occurring within certain ranges helps filter out the outliers and gives a better representation of the data set.

One way to limit the large outliers would have been to start the incremental search

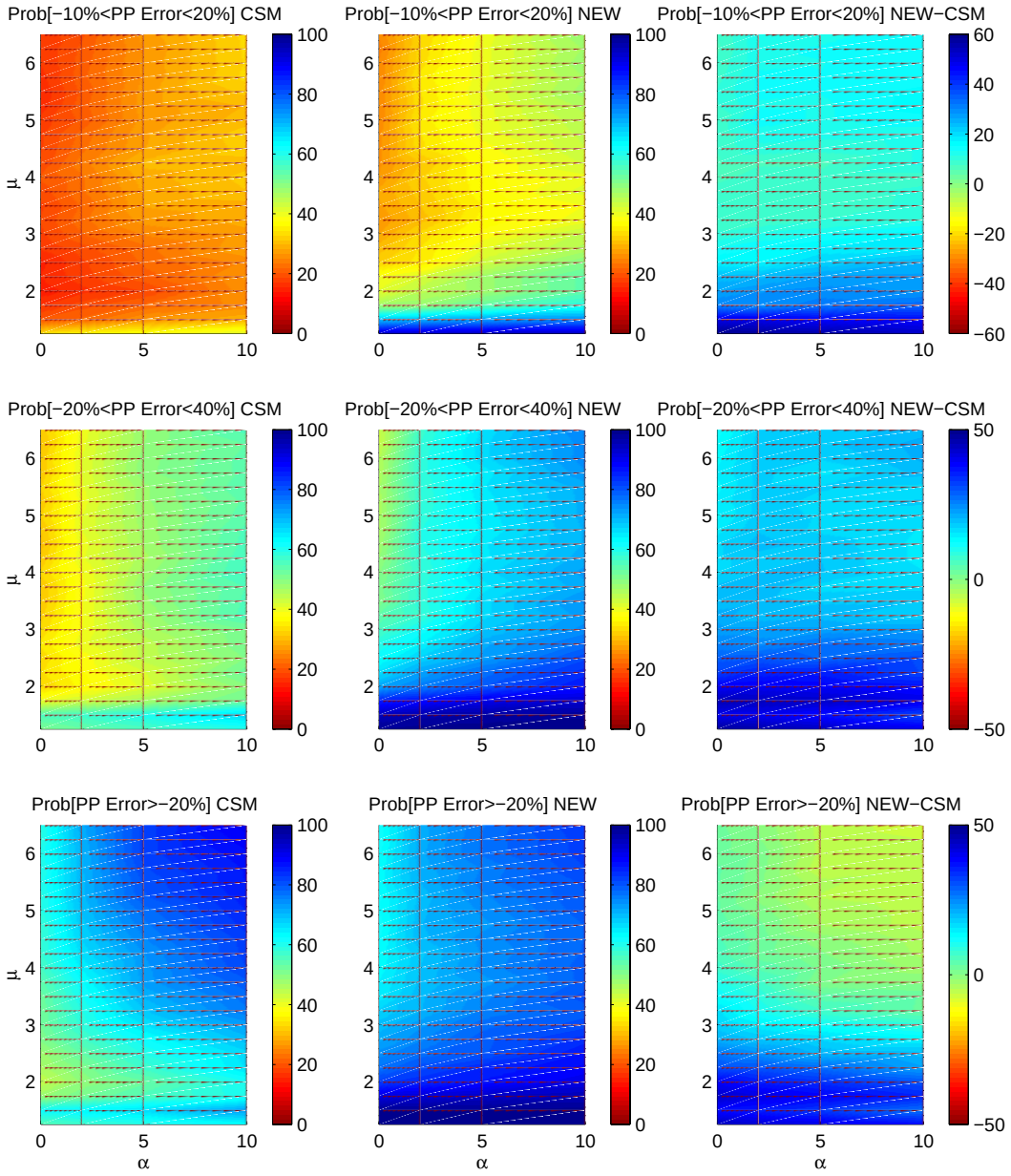

Figure 4.6: Performance Point Error results for bilinear hysteretic system (BLH) - far-field motions. CSM - conventional Capacity Spectrum Method, Structural Behavior Type B (ATC-40). NEW - new approach implemented in this study. Second slope ratios, α, as indicated

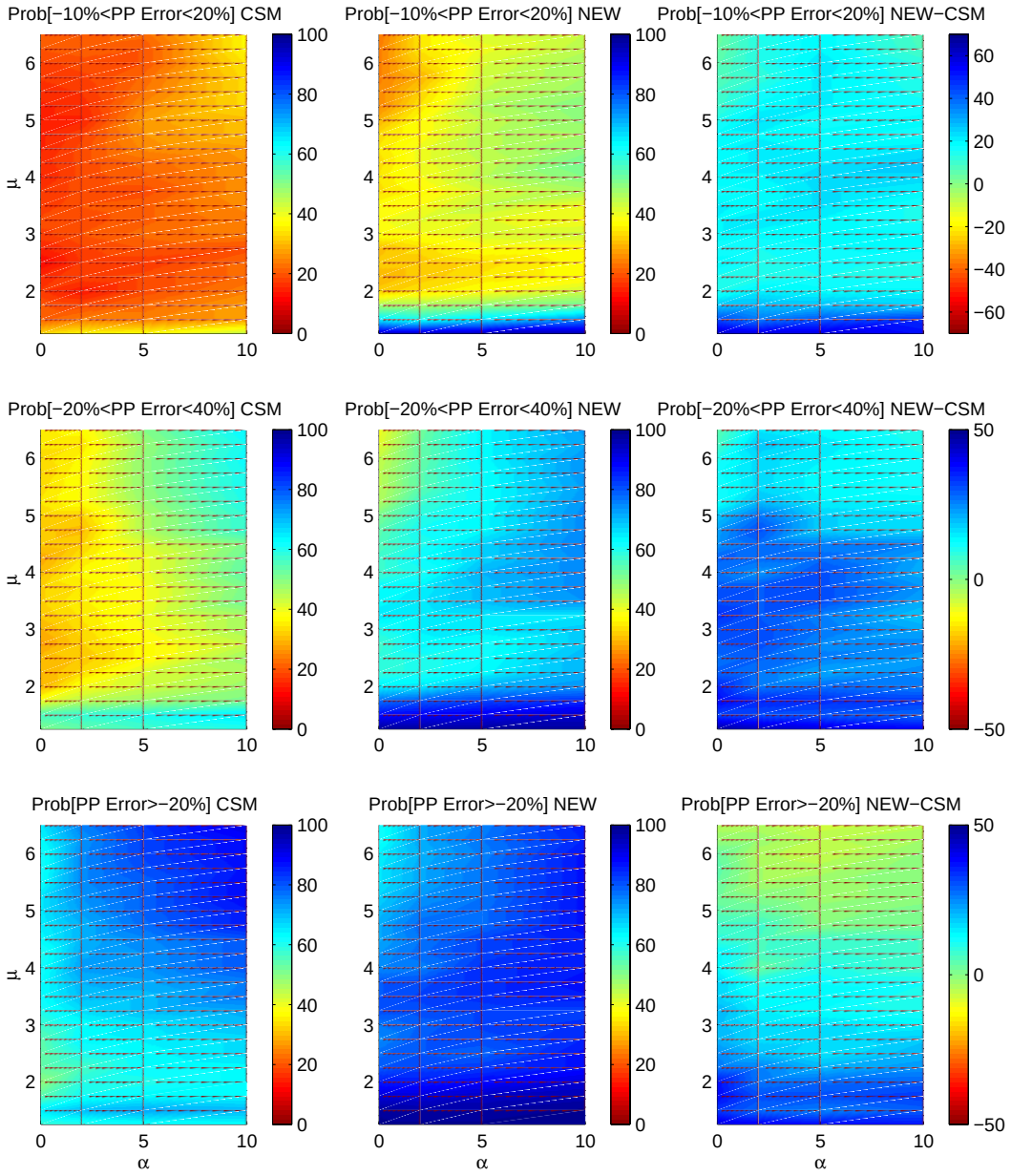

Figure 4.7: Performance Point Error results for bilinear hysteretic system (BLH) - near-field motions with $T_o/T_p \leq 0.7$. CSM - conventional Capacity Spectrum Method, Structural Behavior Type A (ATC-40). NEW - new approach implemented in this study. Second slope ratios, α, as indicated

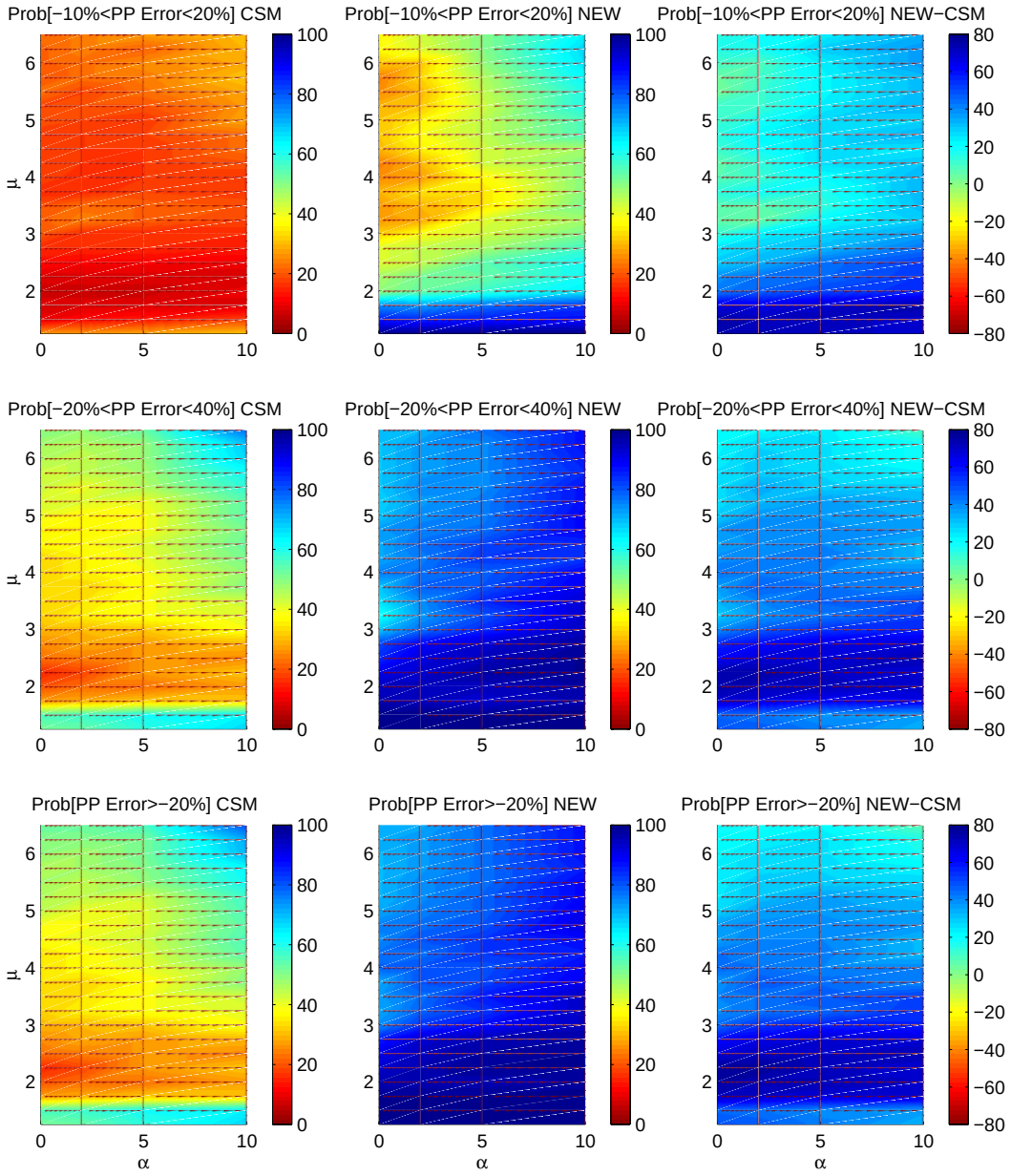

Figure 4.8: Performance Point Error results for bilinear hysteretic system (BLH) - near-field motions with $0.8 \leq T_o/T_p \leq 1.2$. CSM - conventional Capacity Spectrum Method, Structural Behavior Type A (ATC-40). NEW - new approach implemented in this study. Second slope ratios, α, as indicated

at a ductility of 12 or 15. This would essentially add some "engineering judgment" to cases with large ductility predictions. One aspect not incorporated into this study is what happens when a large ductility prediction occurs. In engineering design, a large ductility prediction may lead to the decision to rehabilitate the building. In this case, the large ductility prediction has lead to a different structure and the original structure no longer exists.

As mentioned in Section 3.6, the effective linear parameters for models PIN1 and PIN2 have the proper relationship to the BLH model. The same is true for the Performance Point Error. Results for PIN2 more closely resemble the results for BLH than do the results for PIN1 which has more degradation.

The improvement in the Performance Point Error is most evident at the lower ductility values. This agrees with the observation that the effective parameters are most different at the lower ductility values. The conventional Capacity Spectrum Method is unconservative at lower ductility values but the new effective parameters drastically improve that situation.

4.4.1 Effect of Ground Motion Database Selection on Performance Point Errors

An additional set of 80 far-field ground motions was obtained in conjunction with the ATC-55 Project (Section F.3). The motions are a conglomerate of four sets of twenty records. One set from each site class B, C, D and E as defined by UBC-97. The ATC motions were run on the bilinear and stiffness degrading models with second slope ratios of 0, 2, 5 and 10%. Results for the bilinear system are shown in Figures 4.9 and 4.10. Results for the stiffness degrading system are shown in Figures C.4 and C.5. The error results obtained from the additional ground motions show very good correlation with the 28 CIT ground motions used in the optimization procedure. The 28 CIT motions have slightly better error results, as would be expected, but not by any substantial amount. The effective parameter equations developed in this study are only slightly biased towards the data from which they came. They work equally

well over an independent set of ground motions when compared to the conventional Capacity Spectrum Method effective parameter equations.

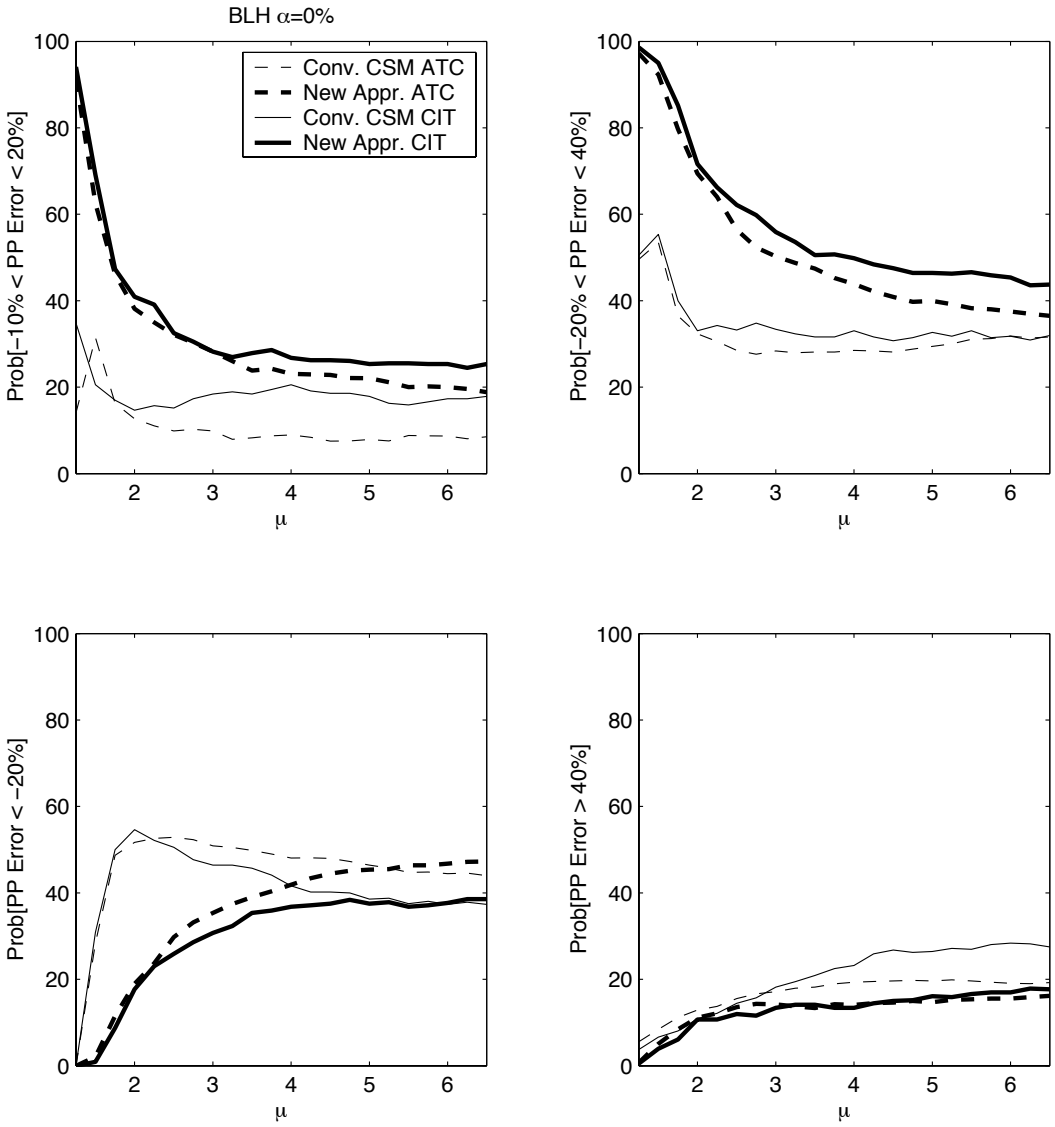

Figure 4.9: Performance Point Error results for bilinear model (BLH) with second slope ratio of 0% - two far-field ground motion databases

4.4.2 Effect of Changing the Engineering Acceptability Range

The bilinear (BLH) and stiffness degrading (KDEG) models with a second slope ratio of 2% were examined to investigate the effect of different Engineering Acceptability

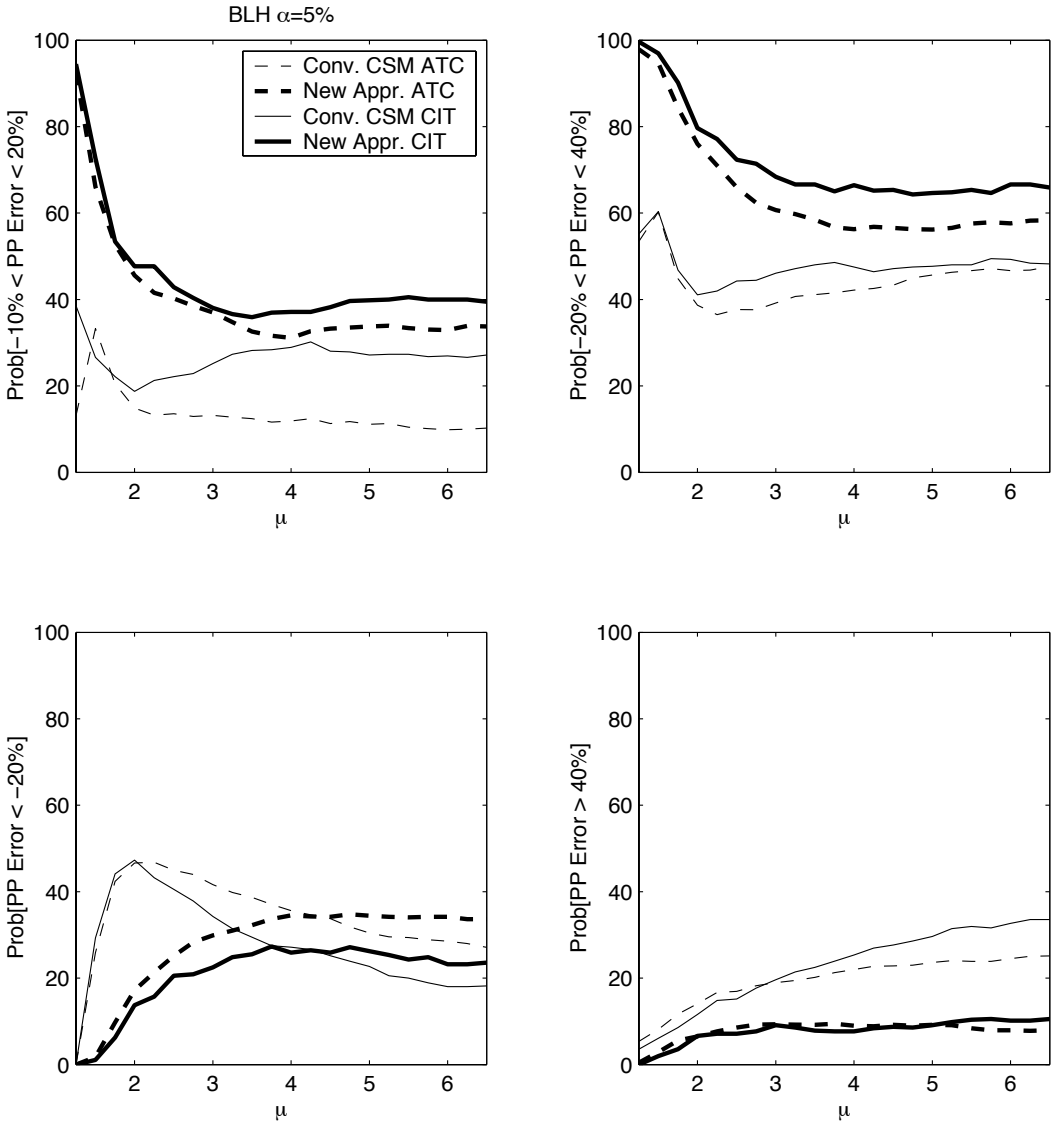

Figure 4.10: Performance Point Error results for bilinear model (BLH) with second slope ratio of 5% - two far-field ground motion databases

Ranges. The different intervals all have a range of 30 (r30) but different center values ranging from 0 (c0) to 25 (c25). Increasing the center value of the interval puts a positive bias in the parameter selection which can clearly be seen in the Performance Point Error statistics. BLH results are shown in Figure 4.11. KDEG results are shown in Figure C.6.

The bias from the conservative Engineering Acceptability Ranges cannot always be seen in the range from -10% to 20% but can definitely be seen in the extreme positive and negative ranges In the graphs of errors less than -20% or greater than 40%, the effects of changing the Engineering Acceptability Range is very apparent. The mean and standard deviation of the Performance Point Error distributions are also shown in the same figures. The mean and standard deviation of the Performance Point Errors also increase as the Engineering Acceptability Range central value increases.

4.4.3 Locus of Performance Points from the UBC Design Spectrum

Performance point displacements (D_{pp}) have been parameterized for different values of initial linear period, T_o, and second slope ratio, α, for the UBC Design Spectrum (Section F.1). The equations are [47]

$$D_{pp}(T_o, \mu_{pp}, \alpha) = \begin{cases} \dfrac{2.5}{4\pi^2}\, T_{eff}^2\, \mathrm{C_a}\, \mathrm{SR_A}(\mu_{pp}, \alpha) & T_{eff} < T_1' \\ \dfrac{T_{eff}}{4\pi^2}\, \mathrm{C_v}\, \mathrm{SR_V}(\mu_{pp}, \alpha) & T_1' < T_{eff} < T_2' \\ \dfrac{0.32}{4\pi^2}\, T_{eff}^2\, \mathrm{N_v}\, \mathrm{SR_V}(\mu_{pp}, \alpha) & T_2' < T_{eff} \end{cases}$$

where C_a, C_v, N_v, SR_A and SR_V are parameters from the UBC Spectrum.

Recall the strength reduction factor, R, from Equation 2.11. Dividing the numer-

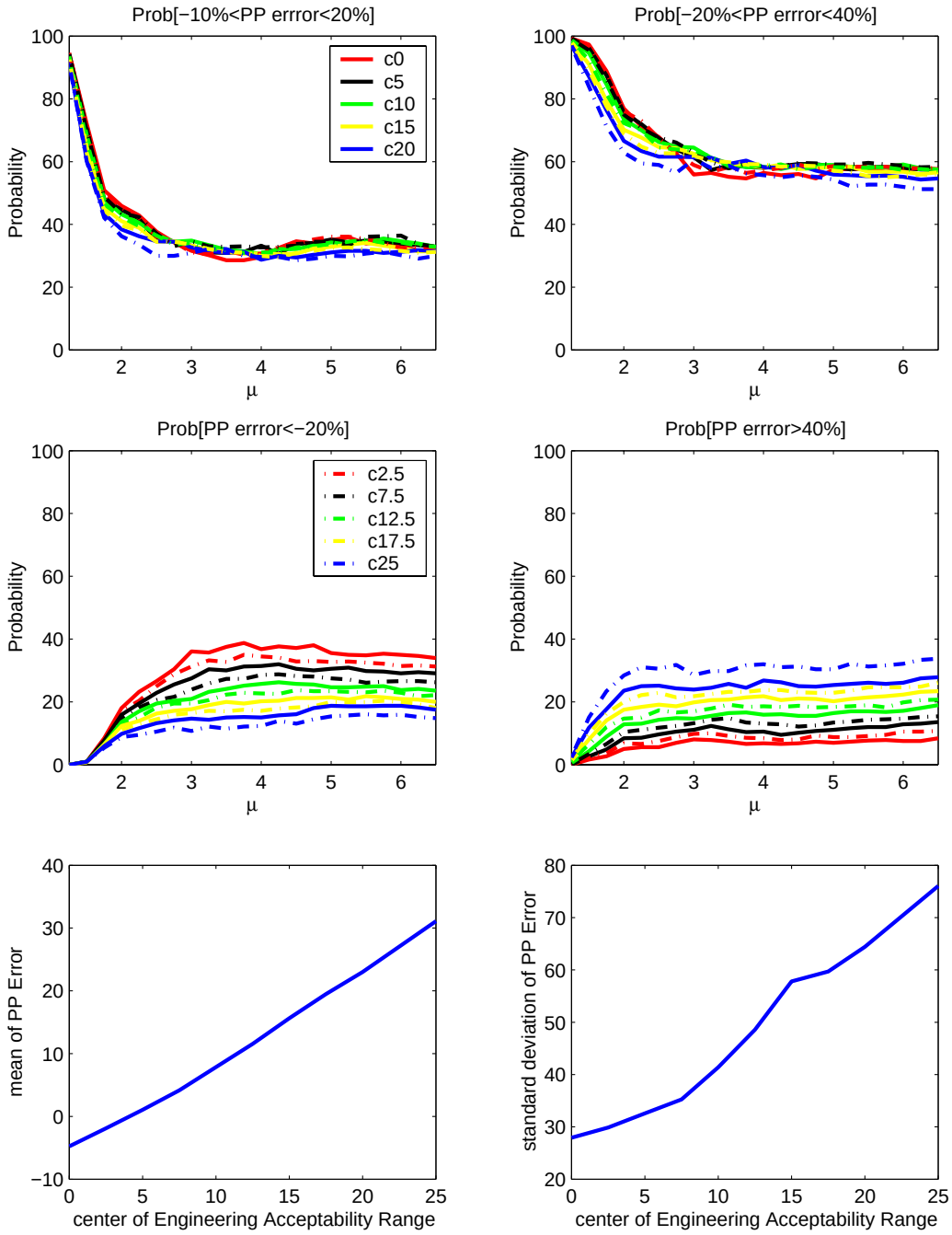

Figure 4.11: Sensitivity of Performance Point Error results to changes in Engineering Acceptability Range for bilinear model with second slope ratio of 2% - far-field motions

ator and denominator by the initial linear stiffness results in

$$R = \frac{D_{lin_{max}}}{D_y} \tag{4.8}$$

Equation 4.8 may alternatively be expressed as

$$R(\mu_{pp}, T_o, \alpha) = \frac{D_{pp}(\mu_{pp} = 1, T_o, \alpha)}{D_{pp}(\mu_{pp}, T_o, \alpha)/\mu_{pp}} \tag{4.9}$$

Figures 4.12 through 4.15 show the Loci of Performance Points for the bilinear (BLH) and stiffness degrading model (KDEG) for different values of initial linear period, T_o and a second slope ratio of 0%. The same is shown in Figures E.1 through E.4 but for $\alpha = 5\%$.

For a consistent R value, the KDEG model always has a larger Performance Point ductility than the BLH model. The stiffness degrading system displacements should be larger than the bilinear system displacements because the KDEG hysteresis loops dissipate less energy in a cycle compared to the BLH hysteresis loops.

The conventional Capacity Spectrum Method (CSM) was shown to be unconservative for both the Displacement Response Error and the Performance Point Error at lower ductilities. The Locus of Performance Points reveals that this has been corrected. The lower ductility values have an increase in the displacement predictions for the new effective parameters.

Another problem with the conventional CSM is that unrealistically large ductilities are predicted for large R values. For the ductility range from 5.25 to 6.5, the conventional CSM is extremely conservative as seen in the tabular data presentation. The Loci reveal that the new effective parameters give lower ductility predictions at these large R values.

4.5 Conclusions

Based on the analysis of the equivalent linear parameters, the following conclusions can be drawn:

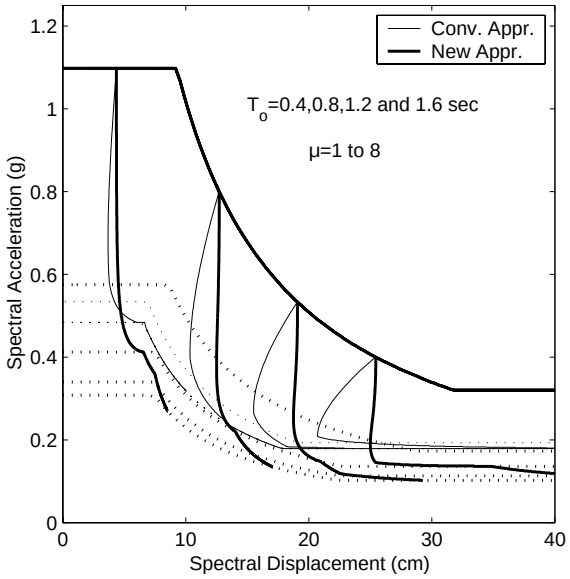

Figure 4.12: UBC Locus of Performance Points for bilinear hysteretic system (BLH) with $\alpha = 0\%$ **-** far-field motions

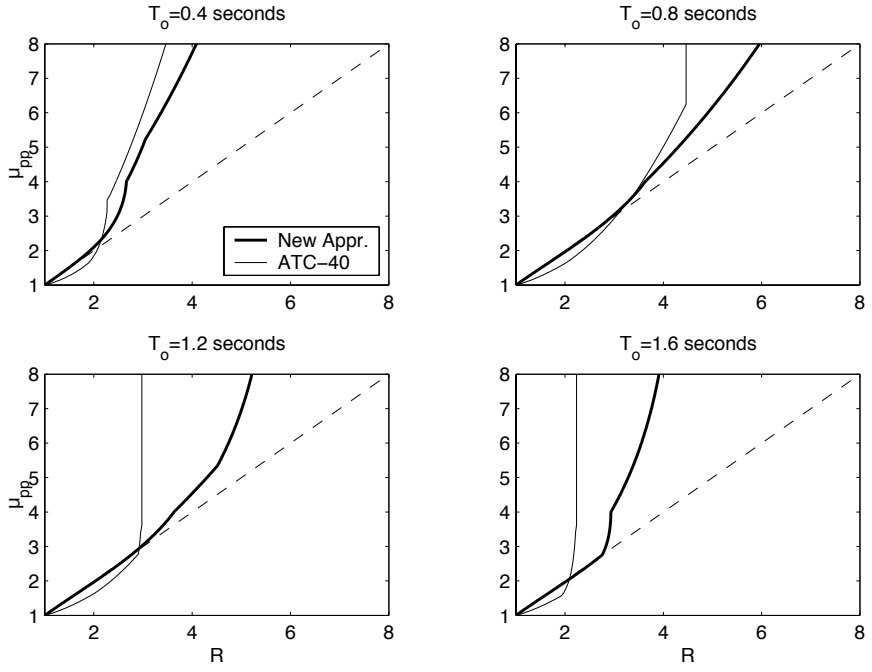

Figure 4.13: Strength reduction factor, R, versus Performance Point ductility, μ_{pp}, from Figure 4.12

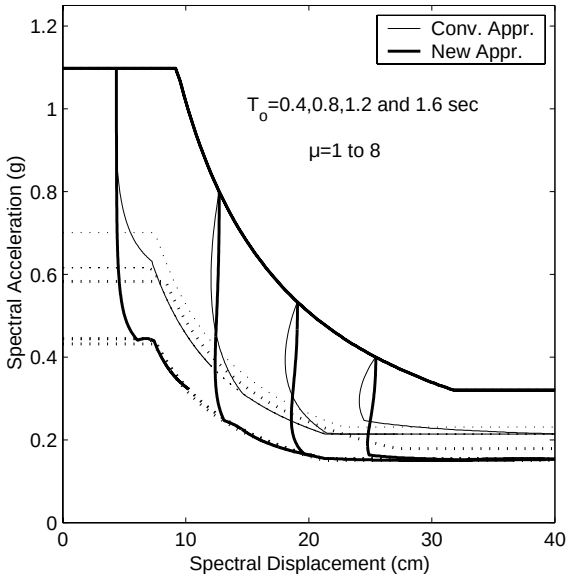

Figure 4.14: UBC Locus of Performance Points for stiffness degrading system (KDEG) with $\alpha = 0\%$ **-** far-field motions

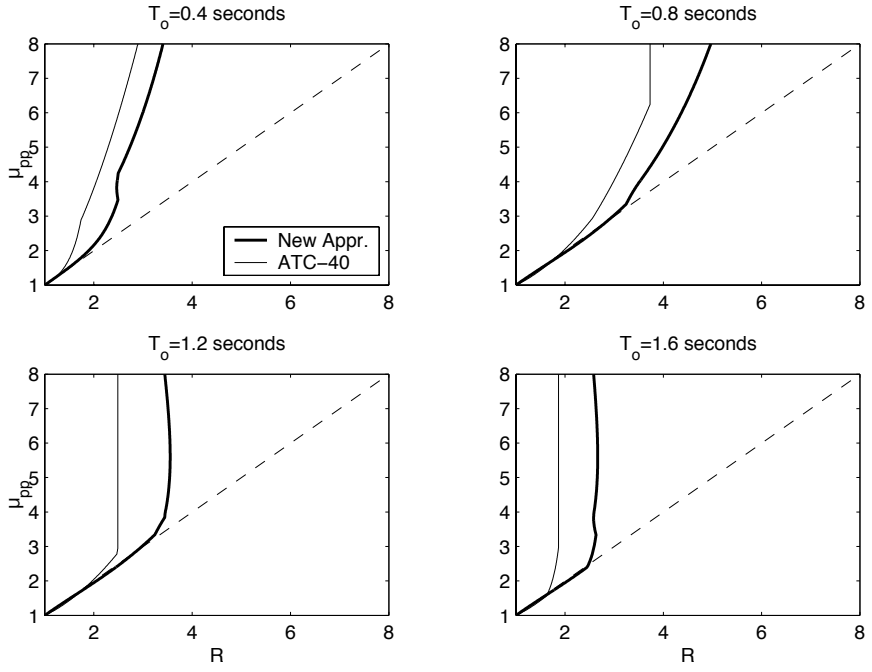

Figure 4.15: Strength reduction factor, R, versus Performance Point ductility, μ_{pp}, from Figure 4.14

1. For all models, the probability of the Performance Point Error ($\epsilon_{D_{pp}}$) lying within the Engineering Acceptability Range is much higher for the new approach than for the current Capacity Spectrum Method (CSM), especially at the lower ductilities. The sensitivity to effective parameter selection is greatest at the lower ductilities as discussed in Section 3.4. This validates the use of higher order curve fitting at the lower ductilities to help capture local variations in the effective parameters.

2. At low values of ductility, the conventional Capacity Spectrum Method approach is extremely unconservative. A building that should be rehabilitated may be determined to not need an upgrade from the conventional Capacity Spectrum Method approach. Within the framework of Performance-Based Engineering, where Performance Objectives (Section 1.4) are very precise, accurate prediction at the lower ductility values is extremely important in terms of Immediate Occupancy and Operational Building Performance Levels.

3. Solution procedures A and B are not recommended for use in engineering design. Solution procedures A and B both incorporate an incremental step method and are designed to analyze a large number of systems and ground motions. Both schemes were developed for research purposes and both are not very practical to implement on capacity curves that are not bilinear. A detailed solution procedure will be introduced in Section 5.1 that has been created for implementation as an engineering design tool.

4. The use of separate equations for different period ranges in the near-field analysis is justified by the Performance Point Errors. Breaking the analysis up onto the period ranges $T_o/T_p \leq 0.7$ and $0.8 \leq T_o/T_p \leq 1.2$ has a significant effect on the accuracy of the equations. The single equation in the conventional CSM is extremely inaccurate for both period ranges. The current CSM equations are worse for structural periods near the pulse period than for periods below the pulse period. The new approach shows great improvement in both period

ranges. This validates the use of different equations for different near-field period ranges.

5. The Performance Point Errors reveal that the equations developed in this methodology are a significant improvement over the current CSM equations currently being used. The methodology, which was formulated for minimizing the Displacement Response Error, has resulted in an improvement to the Performance Point Error. It would be best to optimize over the Performance Point Error but that is impossible. The Performance Point Error analysis requires an equation for the effective linear parameters. This would result in an optimization over an infinite number of lines, not discrete data points as was done in this methodology. The best that can be done is to change the optimization criterion and examine the error statistics as was done in Section 4.4.2.

Model	Eqn.	α	$\epsilon_{D_{eff}}$		$\epsilon_{D_{pp}}$			
			mean	**STD**	**mean**	**STD**	**N/C**	**mult**
BLH	NEW	0%	−3.23	24.61	6.02	64.37	0.04	4.89
BLH	CSMstrB	0%	−6.11	30.50	25.07	143.39	4.37	1.44
BLH	NEW	2%	−2.11	22.51	1.37	33.07	0.04	2.91
BLH	CSMstrB	2%	−3.51	28.45	26.96	124.96	2.61	0.54
BLH	NEW	5%	−1.31	20.47	1.30	27.94	0.02	1.96
BLH	CSMstrB	5%	−0.49	26.46	20.88	78.29	2.09	0.24
BLH	NEW	10%	−0.34	18.28	2.02	24.85	0.01	0.93
BLH	CSMstrB	10%	2.09	23.99	16.79	49.89	1.85	0.09
KDEG	NEW	0%	0.66	16.62	15.59	94.77	0.02	6.66
KDEG	CSMstrC	0%	17.80	27.89	80.69	174.16	2.94	4.30
KDEG	NEW	2%	0.78	16.14	12.49	80.08	0.06	5.43
KDEG	CSMstrC	2%	17.01	26.47	67.13	144.28	1.39	1.88
KDEG	NEW	5%	0.93	15.40	10.29	72.08	0.03	4.33
KDEG	CSMstrC	5%	18.22	25.93	59.97	111.76	0.58	1.39
KDEG	NEW	10%	1.23	14.42	5.94	39.71	0.06	2.72
KDEG	CSMstrC	10%	20.28	25.74	49.84	66.57	0.53	0.90
STRDG	NEW	−3%	0.42	17.37	8.14	50.38	0.17	8.30
STRDG	CSMstrC	−3%	19.56	30.72	60.69	110.27	11.01	10.34
STRDG	NEW	−5%	0.24	17.87	9.95	54.62	0.24	9.78
STRDG	CSMstrC	−5%	21.01	33.17	83.53	147.30	12.77	20.47
PIN1	NEW	2%	−0.09	17.51	14.31	94.13	0.16	10.25
PIN1	CSMstrC	2%	2.48	21.51	30.81	118.60	1.09	3.69
PIN1	NEW	5%	0.27	16.78	13.59	86.65	0.17	9.30
PIN1	CSMstrC	5%	3.16	20.55	23.06	84.04	0.83	2.82
PIN1	NEW	10%	0.67	15.82	9.91	61.89	0.16	7.68
PIN1	CSMstrC	10%	3.78	19.36	15.56	44.55	0.75	2.04
PIN2	NEW	2%	−0.03	17.14	10.92	75.50	0.09	5.75
PIN2	CSMstrC	2%	12.79	26.19	56.71	137.44	1.48	2.27
PIN2	NEW	5%	0.36	16.01	8.42	57.59	0.08	4.92
PIN2	CSMstrC	5%	14.29	25.09	50.32	104.50	0.78	1.54
PIN2	NEW	10%	0.75	14.69	6.01	39.98	0.07	3.58
PIN2	CSMstrC	10%	15.69	23.91	40.44	59.84	0.66	0.94
PB	NEW	NA	0.31	17.59	58.40	190.70	0.22	20.24

Table 4.1: Summary of Displacement Response Error ($\epsilon_{D_{eff}}$) and Performance Point Error ($\epsilon_{D_{PP}}$) over the entire range of ductilities ($1.25 : 0.25 : 6.5$) for period range T_{low} **-** far-field ground motions. CSMstrB/C **-** conventional Capacity Spectrum Method for Structural Behavior Type (str) indicated. NEW **-** new approach implemented in this study. N/C **-** Non-convergent cases. mult **-** multiple solutions

Model	**Eqn.**	α	$\epsilon_{D_{pp}}$ **Range**	$\mu =$ **1.25-3.0**	$\mu =$ **3.25-5.0**	$\mu =$ **5.25-6.5**
BLH	NEW	0%	-10% to 20%	47.72	26.76	25.27
BLH	CSMstrB	0%	-10% to 20%	19.20	18.93	16.88
BLH	NEW	5%	-10% to 20%	54.64	37.68	40.00
BLH	CSMstrB	5%	-10% to 20%	24.69	28.26	27.02
KDEG	NEW	0%	-10% to 20%	62.34	42.01	41.37
KDEG	CSMstrC	0%	-10% to 20%	32.88	22.90	22.41
KDEG	NEW	5%	-10% to 20%	65.16	45.71	47.29
KDEG	CSMstrC	5%	-10% to 20%	35.11	24.80	23.13
STRDG	NEW	-5%	-10% to 20%	59.04	34.80	32.08
STRDG	CSMstrC	-5%	-10% to 20%	28.17	16.23	14.70
PB	NEW	NA	-10% to 20%	64.13	28.26	23.54
BLH	NEW	0%	-20% to 40%	74.31	49.17	45.24
BLH	CSMstrB	0%	-20% to 40%	39.33	31.88	31.82
BLH	NEW	5%	-20% to 40%	81.96	65.51	65.65
BLH	CSMstrB	5%	-20% to 40%	47.52	47.50	48.57
KDEG	NEW	0%	-20% to 40%	86.12	67.79	66.58
KDEG	CSMstrC	0%	-20% to 40%	57.77	41.61	41.85
KDEG	NEW	5%	-20% to 40%	88.86	73.73	74.29
KDEG	CSMstrC	5%	-20% to 40%	60.47	47.92	44.49
STRDG	NEW	-5%	-20% to 40%	83.01	60.13	57.74
STRDG	CSMstrC	-5%	-20% to 40%	49.78	31.07	30.12
PB	NEW	NA	-20% to 40%	84.42	50.45	41.70

Table 4.2: Summary (in %) of Performance Point Error ($\epsilon_{D_{PP}}$) for three separate ductility ranges **-** far-field ground motions. CSMstrB/C **-** conventional Capacity Spectrum Method for Structural Behavior Type (str) indicated. NEW **-** new approach implemented in this study

Model	**Eqn.**	α	$\epsilon_{D_{pp}}$ **Range**	$\mu =$ **1.25-3.0**	$\mu =$ **3.25-5.0**	$\mu =$ **5.25-6.5**
BLH	NEW	0%	$\leq -20\%$	16.94	36.36	37.77
BLH	CSMstrB	0%	$\leq -20\%$	41.54	42.10	37.80
BLH	NEW	5%	$\leq -20\%$	12.59	26.16	24.08
BLH	CSMstrB	5%	$\leq -20\%$	34.58	26.74	18.96
KDEG	NEW	0%	$\leq -20\%$	5.89	20.31	21.70
KDEG	CSMstrC	0%	$\leq -20\%$	8.64	8.26	6.25
KDEG	NEW	5%	$\leq -20\%$	5.07	16.92	16.58
KDEG	CSMstrC	5%	$\leq -20\%$	7.05	5.67	4.40
STRDG	NEW	-5%	$\leq -20\%$	7.66	24.11	26.19
STRDG	CSMstrC	-5%	$\leq -20\%$	9.93	8.93	7.20
PB	NEW	NA	$\leq -20\%$	4.40	20.33	25.92
BLH	NEW	0%	$\geq 40\%$	8.62	14.46	16.99
BLH	CSMstrB	0%	$\geq 40\%$	11.23	23.93	27.71
BLH	NEW	5%	$\geq 40\%$	5.40	8.33	10.27
BLH	CSMstrB	5%	$\geq 40\%$	12.14	25.76	32.47
KDEG	NEW	0%	$\geq 40\%$	7.88	11.90	11.73
KDEG	CSMstrC	0%	$\geq 40\%$	30.78	47.52	48.36
KDEG	NEW	5%	$\geq 40\%$	6.00	9.33	9.14
KDEG	CSMstrC	5%	$\geq 40\%$	31.07	46.38	50.86
STRDG	NEW	-5%	$\geq 40\%$	9.17	15.60	15.48
STRDG	CSMstrC	-5%	$\geq 40\%$	32.30	46.03	45.00
PB	NEW	NA	$\geq 40\%$	11.12	29.04	31.88

Table 4.3: Summary (in %) of Performance Point Error ($\epsilon_{D_{PP}}$) for three separate ductility ranges - far-field ground motions. CSMstrB/C - conventional Capacity Spectrum Method for Structural Behavior Type (str) indicated. NEW - new approach implemented in this study

Chapter 5

New Capacity Spectrum Method of Analysis

5.1 Detailed Performance Point Solution Procedure for Application by Structural Engineers

A detailed version of the Performance Point solution procedure proposed in Section 2.8 is now provided. The solution procedure introduced in this section is intended for implementation by structural engineers. The procedures A and B presented in Section 4.3 are most suitable for an automated implementation with a bilinear capacity spectrum. Those procedures were developed from a research point of view which required the analysis of a large number of capacity spectra and ground motions. The only desired information was the Performance Point ductility value.

The new Performance Point solution procedure is designed to work for any shape of capacity spectrum. It will also give *substantially* more insight into the sensitivity of the Performance Point prediction. The procedure is intended to be a structural engineering analysis tool for building design and evaluation. Beyond just a Performance Point prediction, the procedure will reveal how changes in either the capacity or demand will effect the prediction. This new procedure also rigorously reveals cases when there are multiple Performance Point solutions and is intended for implementation in a completely graphical nature. It contains steps that can both be done by hand analysis (with paper and pencil) or implemented on a computer (Excel or

Matlab). The engineer can implement the steps in any medium desired but must understand that a hand analysis will likely be less accurate than one performed on a computer.

1. For a building designed on a specific site, a computer model of the structure is constructed as discussed in Section 1.4.2.2. A push-over analysis is performed on the computer model using the first mode shape load profile. A load-deflection curve is obtained from the push-over analysis. The building must also be classified as a hysteretic system **-** BLH, KDEG, PIN1 or PIN2. This is discussed in Section 3.1. Assume a nominal viscous damping value (ζ_o) of 5% unless other information is obtained that leads to a different value.

   Commentary: *The effective parameter equations have been developed for buildings with $\zeta_o \leq 10\%$. Buildings with supplemental damping devices or base isolation should not be analyzed by this procedure.*

2. Convert the push-over curve into a capacity spectrum using the following equations

$$\text{Spectral Acceleration} = \text{Force } \tilde{\mathbf{a}}^T\mathbf{M}\tilde{\mathbf{a}}/(\tilde{\mathbf{a}}^T\mathbf{M}\tilde{\mathbf{I}})^2 \tag{5.1}$$

$$\text{Spectral Displacement} = \text{Displacement } \tilde{\mathbf{a}}^T\mathbf{M}\tilde{\mathbf{a}}/(\tilde{\mathbf{a}}^T\mathbf{M}\tilde{\mathbf{I}}) \tag{5.2}$$

   where $\tilde{\mathbf{a}}$ is the fundamental lateral mode shape, $\mathbf{M}$ is the mass matrix for the horizontal degrees of freedom and $\tilde{\mathbf{I}}$ is the identity vector.

3. On the capacity spectrum, fit a bilinear approximation for several values of post-yield displacement, d_*. This requires the determination of a yield point (d_y, a_y) and an end point (d_*, a_*) for each bilinear approximation. Use Equations 5.3 through 5.5 to calculate the initial period, T_o, ductility, μ, and second slope ratio, α. Record these values in Table 5.1.

$$T_o = 2\pi\sqrt{a_y/d_y} \tag{5.3}$$

$$\mu = d_*/d_y \tag{5.4}$$

$$\alpha = [(a_* - a_y)d_y]/[(d_* - d_y)a_y] \tag{5.5}$$

(d_*, a_*)	(d_y, a_y)	T_o	μ	α	T_{eff}	ζ_{eff}	T_{sec}	M

Table 5.1: Table of values calculated during the solution procedure

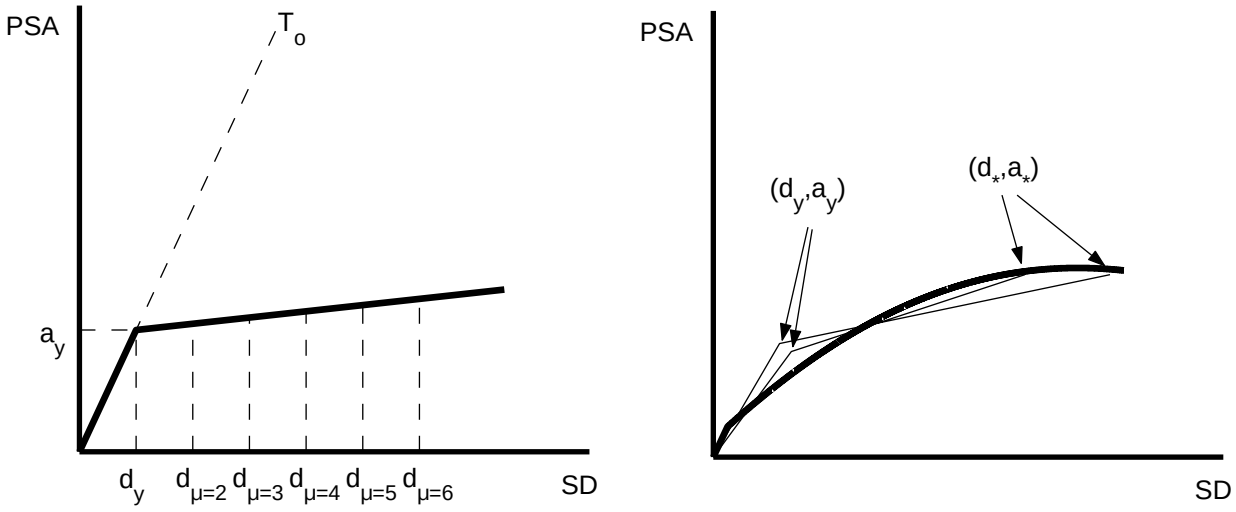

(a) Bilinear capacity spectrum

(b) Curved capacity spectrum

Figure 5.1: Capacity spectrum shapes

Commentary: *Two examples of capacity curves are shown in Figures 5.1. Figure 5.1(a) is a bilinear capacity spectrum and therefore T_o and (d_y, a_y) will not change for different levels of ductility. Figure 5.1(b) shows a rounded capacity spectrum which requires separate bilinear approximations for each point (d_*, a_*) . A bilinear approximation is necessary because the equivalent parameter equations have been developed from models with constant second slope ratios.*

4. Use the values in Table 5.1 to calculate T_{eff} and ζ_{eff} using the equations in Section 3.4. For second slope ratios, α, not equal to the discrete values in

Section 3.4, use linear interpolation. Record the values of T_{eff} and ζ_{eff} in Table 5.1.

5. Calculate the modification factor, M, for the different values of ductility and second slope ratio from the equations in Section 3.4. For second slope ratios, α, not equal to the discrete values in Section 3.4, use linear interpolation. Record the values of T_{eff} and ζ_{eff} in Table 5.1.

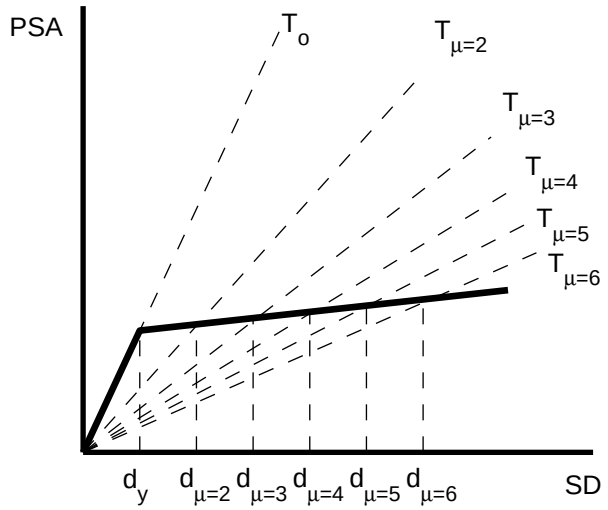

Figure 5.2: Bilinear capacity spectrum with secant period lines

Commentary: *The modification factor can also be calculated as* $M = (\frac{T_{eff}}{T_o}\frac{T_o}{T_{secant}})^2$. *The secant period ratio,* T_{secant}/T_o, *can be calculated from bilinear approximations made on the capacity spectrum using the equation* $T_{secant}/T_o = 2\pi\sqrt{a_*/d_*}$. *Figure 5.2 shows the secant period lines drawn onto the bilinear capacity spectrum.*

6. Obtain a design spectrum for the nominal amount of damping (ζ_o) and demand spectra for all ζ_{eff} values in Table 5.1.

Commentary: *The approach to this step will depend on the design spectrum. The UBC design spectrum can easily be calculated for any value of damping using the procedure presented in Section F.1. Substitute* ζ_{eff} *for* β_{eff} *in equation 1.28. A site-specific spectra from a ground motion consultant may also be*

used. The design spectrum for the nominal amount of damping (ζ_o) and other larger amounts of damping will be needed. Increments of 5% up to about 25% should be fine. An example is shown in Figure 5.3. Ductility values are associated with effective damping values in Table 5.1. Linear interpolation should be used for intermediate damping values.

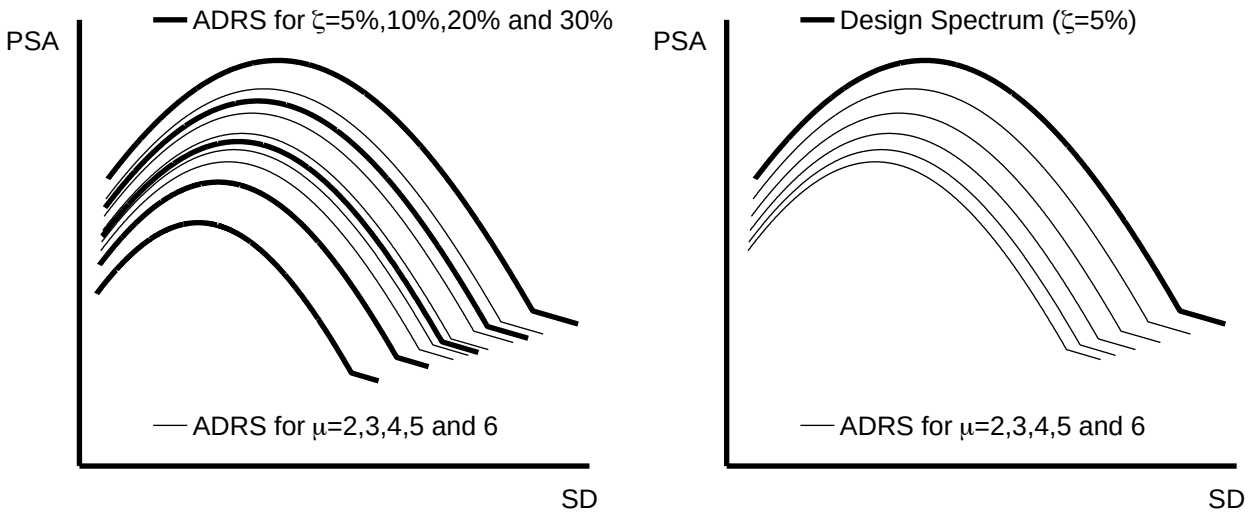

(a) ADRS for a range of ζ values and for different levels of ductility from Table 5.1

(b) ADRS for a range of ductility values

Figure 5.3: Family of Acceleration-Displacement Response Spectra (ADRS)

7. Multiply each ADRS by its corresponding modification factor. This results in the family of MADRS curves as shown in Figure 5.4.

8. Along the capacity spectrum, draw radial lines from the origin through the d_*, a_* points associated with the different values of ductility along the capacity spectrum. Each radial line represents the secant period for the corresponding ductility value. Mark the point of intersection of each radial line with the appropriate MADRS.

9. The Locus of Performance Points is obtained by connecting the points of intersection from Step 8.

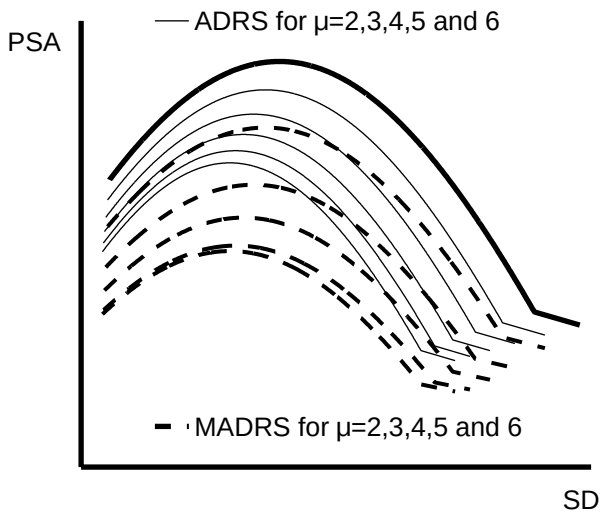

Figure 5.4: Family of Modified Acceleration-Displacement Response Spectra (MADRS) after Step 7

10. The Performance Point is the intersection of the capacity spectrum and the Locus of Performance Points as seen in Figure 5.5.

    Commentary: *If necessary, at any time go back to step 2 and choose a different end point for the capacity spectrum (d_*,a_*) and repeat the analysis. Choosing d_* to be the smallest or largest displacement in Table 5.1 will help to check if multiple solutions exist. Choosing d_* near the Performance Point predicted in Step 10 will help give a more accurate answer.*

5.2 Observations on the New Solution Procedure

Based on the New Capacity Spectrum of Analysis presented in Section 5.1 the following observations can be made:

1. The new procedure is completely graphical for extremely transparent application. Figure 5.5 shows the culmination of all the steps in the new Performance Point solution procedure. The more bilinear approximations used in step 2, the more points will make up the Locus of Performance Points. At anytime, a new line can be added to Table 5.1 and the Locus of Performance Points can be

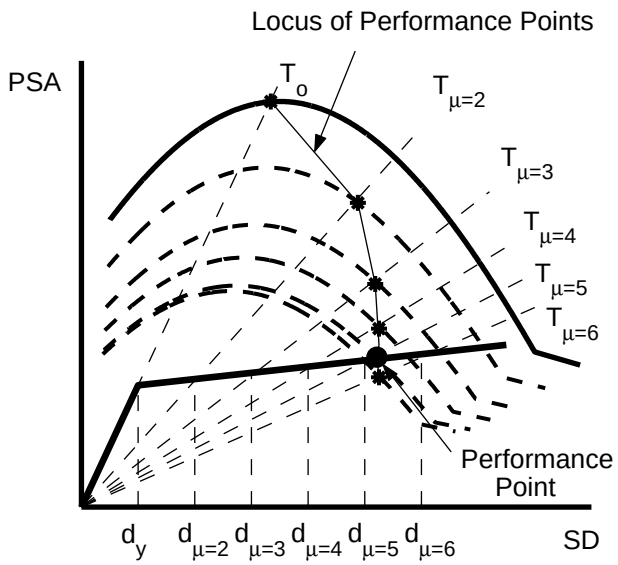

Figure 5.5: Graphically determining the Performance Point after Step 10

refined and improved.

2. The graphical nature of the new solution procedure allows the sensitivity of the Performance Point prediction to be directly observable. At the end of the analysis, the engineer should take a step back and ask the question as to what would happen to the Performance Point if the capacity spectrum changed slightly. If the strength of the capacity spectrum were increased or decreased, what would happen to the Performance Point. This issue deals with the angle of intersection of the Locus of Performance Points and the capacity spectrum. The angle of intersection is directly observable in this procedure.

3. The new solution procedure also reveals whether it would be beneficial to go back and add more lines to Table 5.1. If the Locus of Performance Points is nearly vertical, there would be no need to go back and add another iteration. Loci of Performance Points for a bilinear capacity spectra using the UBC design spectrum are graphed in Section 4.4.3.

4. While the conventional Capacity Spectrum Method solution procedures in ATC-40 make no mention of it, the possibility of multiple Performance Point solutions

can clearly be seen in the new procedure. The Performance Point is at the intersection of the capacity spectrum and the Locus of Performance Points which might occur once, several times or even not at all. Extending the Locus of Performance Points to ductilities beyond the first intersection of the Locus and the capacity spectrum can clearly reveal the possibility of another intersection point. Multiple Performance Points should require serious attention. A conservative approach is to use the Performance Point at the largest displacement. Another approach is to modify the capacity spectrum so that there are not multiple solutions. This would require performing a retrofit procedure on the structure.

5. The new procedure can clearly give insight into the effects of strengthening, stiffening and increasing ductility capacity on a case by case basis in a extremely efficient manner. The same can be said about changes in the demand spectra. A change on the demand side is perhaps less practical since the engineer generally accepts the demand side either as the UBC spectrum or from the recommendation of a ground motion specialist. If the Locus of Performance Points were slightly different, how would that effect the Performance Point solution. This deals with the angle of intersection between the capacity spectrum and the Locus of Performance Points.

6. The new solution procedure can be applied to any type of design spectrum. The only requirement is that demand spectra for the necessary values of damping are obtainable. The procedure is equally effective on any shape of design spectrum. The conventional Capacity Spectrum Method procedures were developed to be used in conjunction with the UBC design spectrum. The spectral reduction equations directly involve the UBC spectrum. The factors SR_A and SR_V are only applicable to the UBC-shaped spectrum. See Section F.1 for more details.

Bibliography

[1] Federal Emergency Management Agency. NEHRP commentary on the guidelines for the seismic rehabilitation of buildings (FEMA 274). Technical report, United States Government, October 1997.

[2] Federal Emergency Management Agency. NEHRP guidelines for the seismic rehabilitation of buildings (FEMA 273). Technical report, United States Government, October 1997.

[3] Federal Emergency Management Agency. Handbook for the seismic evaluation of buildings – a prestandard (FEMA 310). Technical report, United States Government, January 1998.

[4] Federal Emergency Management Agency. Prestandard and commentary for the seismic rehabilitation of buildings (FEMA 356). Technical report, United States Government, November 2000.

[5] Federal Emergency Management Agency. NEHRP commentary on the recommended provisions for seismic regulations for new buildings and other structures (FEMA 369). Technical report, United States Government, March 2001.

[6] Federal Emergency Management Agency. NEHRP recommended provisions for seismic regulations for new buildings and other structures (FEMA 368). Technical report, United States Government, March 2001.

[7] Babak Alavi and H. Krawinkler. Effects of near-field ground motion on building structures. Technical report, Stanford University, December 1999.

[8] Mark Ascheim and E. Black. Effects of prior earthquake damage on response of simple stiffness-degrading structures. *Earthquake Spectra*, 15(1):1–24, February 1999.

[9] Mark Ascheim and E. Black. Yield point spectra for seismic design and rehabilitation. *Earthquake Spectra*, 16(2):317–336, May 2000.

[10] Mark Ascheim, J. Maffei, and E. Black. Nonlinear static procedures and earthquake displacement demands. In *6th U.S. National Conference on Earthquake Engineering*, 1998.

[11] Mourad Attalla, T. Paret, and S. Freeman. Near-source behavior of buildings under pulse-type earthquakes. In *6th U.S. National Conference on Earthquake Engineering*, 1998.

[12] Anders Carlson. *Three-Dimensional Nonlinear Inelastic Analysis of Steel Moment-Frame Buildings Damaged by Earthquake Excitations*. PhD thesis, California Institute of Technology, 1999.

[13] Anil Chopra and R. Goel. Capacity-demand-diagram methods based on inelastic design spectrum. *Earthquake Spectra*, 15(4):637–656, November 1999.

[14] Anil Chopra and R. Goel. Capacity-demand-diagram methods for estimating seismic deformation of inelastic structures: SDF systems. Technical report, Pacific Earthquake Engineering Research Center, 1999.

[15] Anil Chopra and R. Goel. Evaluation of NSP to estimate seismic deformation: SDF systems. *ASCE Journal of Structural Engineering*, 126(4):482–490, April 2000.

[16] Anil Chopra and R. Goel. Direct displacement-based design: Use of inelastic vs. elastic design spectra. *Earthquake Spectra*, 17(1):47–64, February 2001.

[17] Anil Chopra and R. Goel. A modal pushover analysis procedure to estimate seismic demand for buildings: Theory and preliminary evaluation. Technical report, Pacific Earthquake Engineering Research Center, January 2001.

[18] Anil Chopra, R. Goel, and C. Chimtanapakdee. Statistics of SDF-system estimate of roof displacement for pushover analysis of buildings. Technical report, University of California, Berkeley, 2001.

[19] Applied Technology Council. ATC 40: Seismic evaluation and retrofit of concrete buildings. Technical report, Applied Technology Council, 1996.

[20] Applied Technology Council. ATC 55: Evaluation and improvement of inelastic seismic analysis procedures. Technical report, Applied Technology Council, in progress.

[21] E.F. Cruz, S. Cominetti, and M. Balmaceda. A validation of an approximate method to estimate inelastic seismic response to buildings. In *6th U.S. National Conference on Earthquake Engineering*, 1998.

[22] Isabel Cuesta, M. Aschheim, and P. Fajfar. Simplified R-factor relationships for strong ground motions. *Earthquake Spectra*, 2003.

[23] Craig D. Comartin et al. Seismic evaluation and retrofit of concrete buildings: A practical overview of the *ATC-40* document. *Earthquake Spectra*, 16(1):241–262, February 2000.

[24] Daniel Shapiro et al. NEHRP guidelines and commentary for the seismic rehabilitation of buildings. *Earthquake Spectra*, 16(1):227–240, February 2000.

[25] Peter Fajfar. A nonlinear analysis method for performance-based seismic design. *Earthquake Spectra*, 16(3):573–592, August 2000.

[26] Sigmund A. Freeman. Development and use of capacity spectrum method. In *6th U.S. National Conference on Earthquake Engineering*, 1998.

[27] Nathan Gates. *The Earthquake Response of Deteriorating Systems*. PhD thesis, California Institute of Technology, 1977.

[28] P. Gulkan and M. A. Sozen. Inelastic responses of reinforced concrete structures to earthquake motions. *Journal of the American Concrete Institute*, 71:604–610, 1974.

[29] Akshay Gupta and H. Krawinkler. Behavior of ductile SMRFs at various seismic hazard levels. *Journal of Structural Engineering*, 126(1):98–107, 2000.

[30] Akshay Gupta and H. Krawinkler. Estimation of seismic drift demands for frame structures. *Earthquake Engineering and Structural Dynamics*, 29:1287–1305, 2000.

[31] Akshay Gupta and Helmut Krawinkler. Dynamic p-delta effects for flexible inelastic steel structures. *Journal of Structural Engineering*, 126(1):145, January 2000.

[32] Balram Gupta and S. Kunnath. Effect of hysteretic model parameters on inelastic seismic demands. In *6th U.S. National Conference on Earthquake Engineering*, 1998.

[33] Balram Gupta and S. Kunnath. Adaptive spectra-based pushover procedure for seismic evaluation of structures. *Earthquake Spectra*, 16(2):367–392, May 2000.

[34] John F. Hall. Parameter study of the response of moment-resisting steel frame buildings to near-source ground motions. Technical report, SAC 95-05, 1995.

[35] John F. Hall. Class notes, CE108. Caltech, 1998-1999.

[36] John F. Hall, T. H. Heaton, M. W. Halling, and D. J. Wald. Near-source ground motions and its effects on flexible buildings. *Earthquake Spectra*, 11(4):569–605, 1995.

[37] Ronald Hamburger. Performance-based seismic engineering: The next generation of structural engineering practice. *EQE Review*, Fall 1996.

[38] Robert D. Hanson and Tsu T. Soong. *Seismic Design With Supplemental Energy Dissipation Devices*. Earthquake Engineering Research Institute, 2001.

[39] C. T. Huang. Considerations of multi-mode structural response for near-field earthquakes. National Taiwan University of Science and Technology, October 2001.

[40] Earthquake Engineering Research Institute, editor. *EERI Technical Seminar on Earthquake Analysis Methods: Predicting Building Behavior*, 1999.

[41] Wilfred D. Iwan. A model for the dynamic analysis of deteriorating systems. In *Fifth World Conference in Earthquake Engineering*, 1973.

[42] Wilfred D. Iwan. Estimating inelastic response spectra from elastic spectra. *Earthquake Engineering and Structural Dynamics*, 8:375–388, 1980.

[43] Wilfred D. Iwan. Class notes, CE151. Caltech, 1997-1998.

[44] Wilfred D. Iwan and N. Gates. The effective period and damping of a class of hysteretic structures. *Earthquake Engineering and Structural Dynamics*, 7:199–211, 1979.

[45] Wilfred D. Iwan and N. Gates. Estimating earthquake response of simple hysteretic structures. *Journal of the Engineering Mechanics Division*, pages 391–405, June 1979.

[46] Wilfred D. Iwan and A. C. Guyader. A study of the accuracy of the capacity spectrum method in engineering analysis. In *Proceedings of the Workshop on Performance-Based Earthquake Engineering Methodology*, August 2001.

[47] Wilfred D. Iwan, C. T. Huang, and A. Guyader. Evaluation of the effects of near-source ground motions. Technical report, California Institute of Technology, 1999.

[48] Simon Kim and E. D'Amore. Push-over analysis procedure in earthquake engineering. *Earthquake Spectra*, 15(3):417–434, August 1999.

[49] M. J. Kowalsky. Displacement-based design - a methodology for seismic design applied to reinforced concrete bridge columns. Master's thesis, University of California at San Diego, 1994.

[50] Helmut Krawinkler, R. Medina, M. Miranda, and A. Ayoub. Seismic demands for performance-based design. Stanford University.

[51] Nelson Lam, J. Wilson, and G. Hutchinson. The ductility reduction factor in the seismic design of buildings. *Earthquake Engineering and Structural Dynamics*, 27:749–769, 1998.

[52] Y. Roger Li and J. Jirsa. Parametric studies of nonlinear time history analysis. In *6th U.S. National Conference on Earthquake Engineering*, 1998.

[53] James A. Mahaney, T. Paret, B. Kehoe, and S. Freeman. The capacity spectrum method for evaluating structural response during the loma prieta earthquake. In *National Earthquake Conference*, 1993.

[54] E. Miranda. Inelastic displacement ratios for structures on firm sites. *Journal of the Structural Division, American Society of Civil Engineers*, 126:1150–1159, 2000.

[55] Eduardo Miranda and S. Akkar. Evaluation of iteration schemes in equivalent linearization methods. Stanford University, 2002.

[56] Eduardo Miranda and J. Ruiz-Garcia. Evaluation of approximate methods to estimate maximum inelastic displacement demands. *Earthquake Engineering and Structural Dynamics*, 31(3):539–560, March 2002.

[57] Nathan M. Newmark and W. J. Hall. *Earthquake Spectra and Design*. Earthquake Engineering Research Institute, 1982.

[58] International Conference of Building Officials. *1997 Uniform Building Code*, volume 1 and 2. International Conference of Building Officials, 1997.

[59] G. Paparizos and W. D. Iwan. Some observations on the random response of an elasto-plastic system. *Journal of Applied Mechanics-Transactions of the ASME*, 55(4):911–917, December 1988.

[60] M. J. N. Priestley. Displacement-based seismic assessment of reinforced concrete buildings. *Journal of Earthquake Engineering*, 1(1):157–192, 1997.

[61] Rafael Riddell, J. Garcia, and E. Garces. Inelastic deformation response of SDOF systems subjected to earthquakes. *Earthquake Engineering and Structural Dynamics*, 31:515–538, 2002.

[62] Rafael Riddell and N. M. Newmark. Statistical analysis of the response of non-linear systems subjected to earthquakes. Technical report, Department of Civil Engineering, University of Illinois at Urbana-Champaign, 1979.

[63] Kent Sasaki, S. Freeman, and T. Paret. Multi-mode pushover procedure - a method to identify the effects of higher modes in a pushover analysis. In *6th U.S. National Conference on Earthquake Engineering*, 1998.

[64] CIT Smarts. Ground motion database. Technical report, California Institute of Technology, 2001.

[65] Toshikazu Takeda, M. A. Sozen, and N. N. Nielsen. Reinforced concrete response to simulated earthquakes. *Journal of the Structural Division, American Society of Civil Engineers*, 96(ST12):2557–2573, December 1970.

[66] E. L. Wilson and A. Habibullah. Static and dynamic analysis of multi-story buildings, including p-delta effects. *Earthquake Spectra*, 3(2), 1987.

Appendix A

Effective Linear Parameters

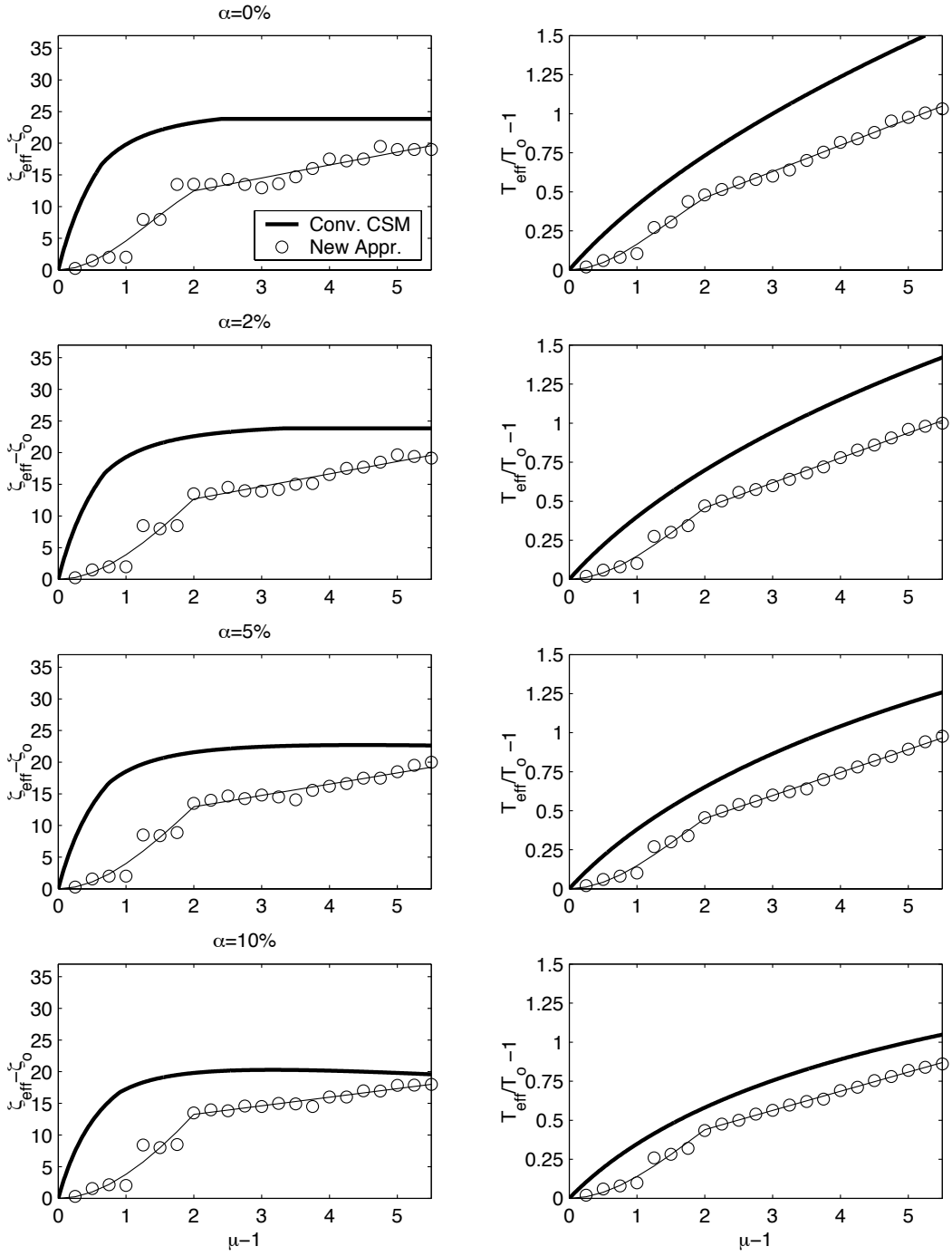

Figure A.1: Effective parameters for stiffness degrading system - near-field motions with $T_o/T_p \leq 0.7$. Conv. CSM - conventional Capacity Spectrum Method, Structural Behavior Type B (ATC-40). New Appr. - new approach implemented in this study. Second slope ratios, α, as indicated

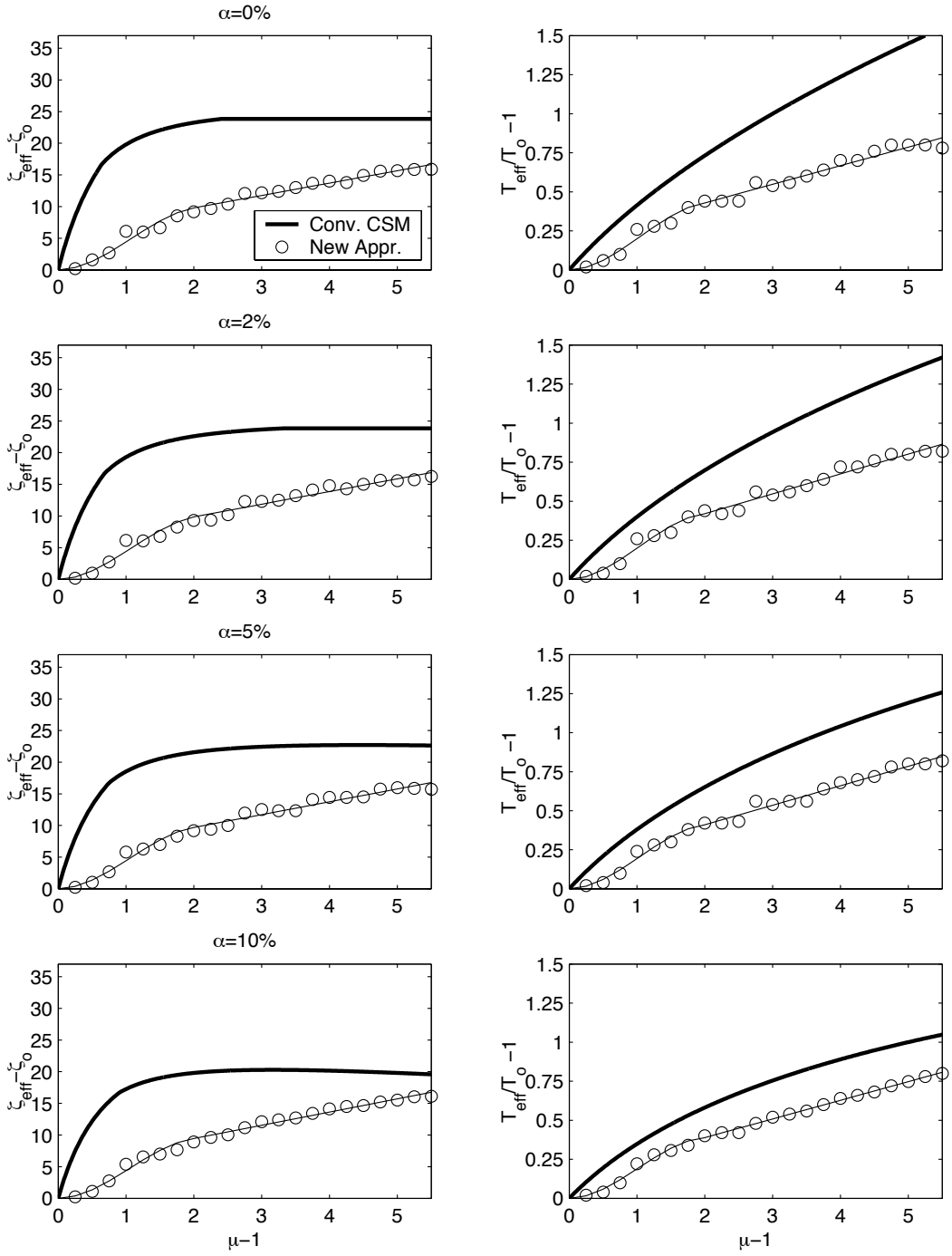

Figure A.2: Effective parameters for stiffness degrading system - near-field motions with $0.8 \leq T_o/T_p \leq 1.2$. Conv. CSM - conventional Capacity Spectrum Method, Structural Behavior Type B (ATC-40). New Appr. - new approach implemented in this study. Second slope ratios, α, as indicated

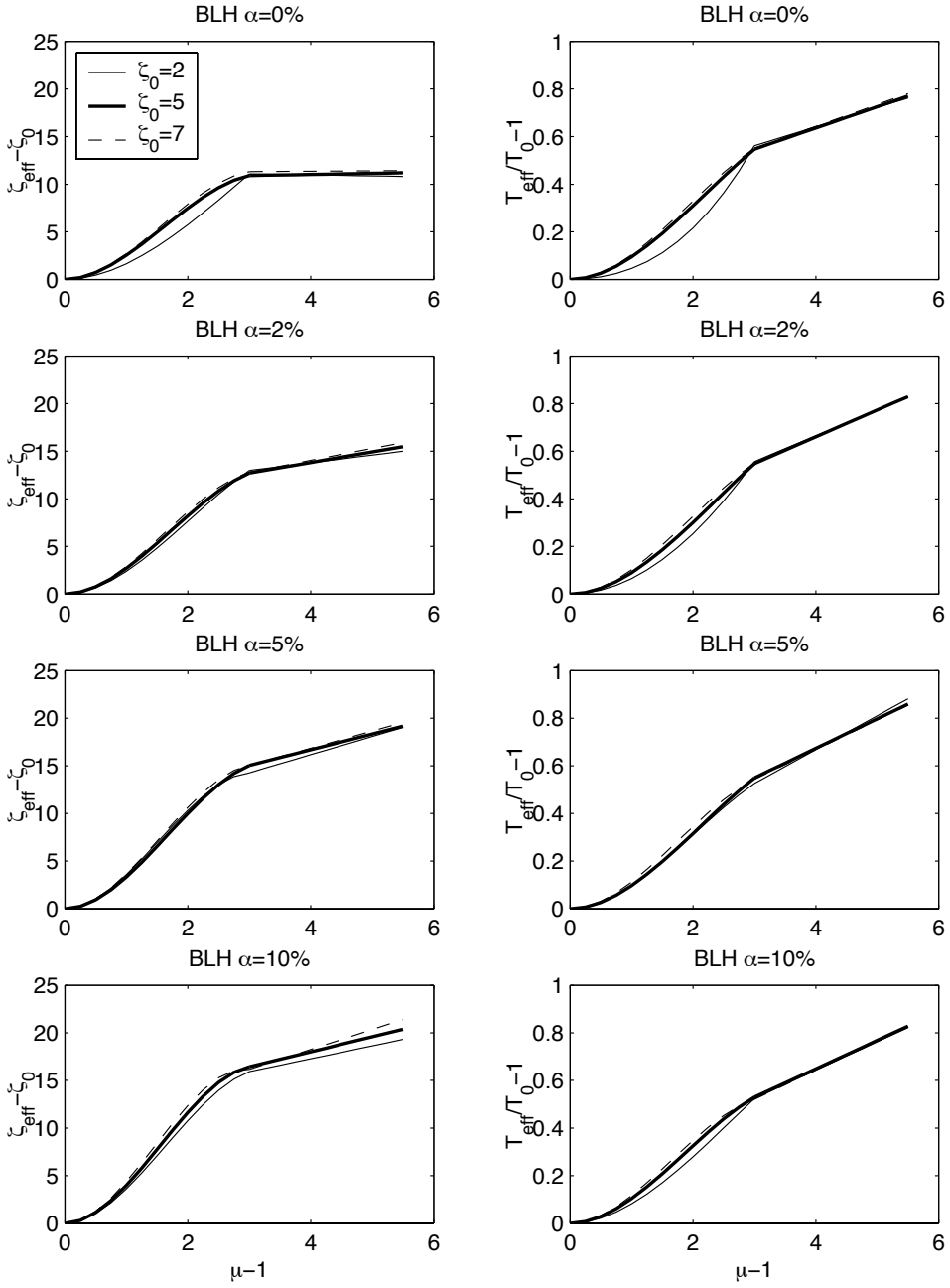

Figure A.3: Effective parameters for bilinear model (BLH) with $\zeta_0 = 2\%$, 5% and 7% and second slope ratios as indicated - far-field motions

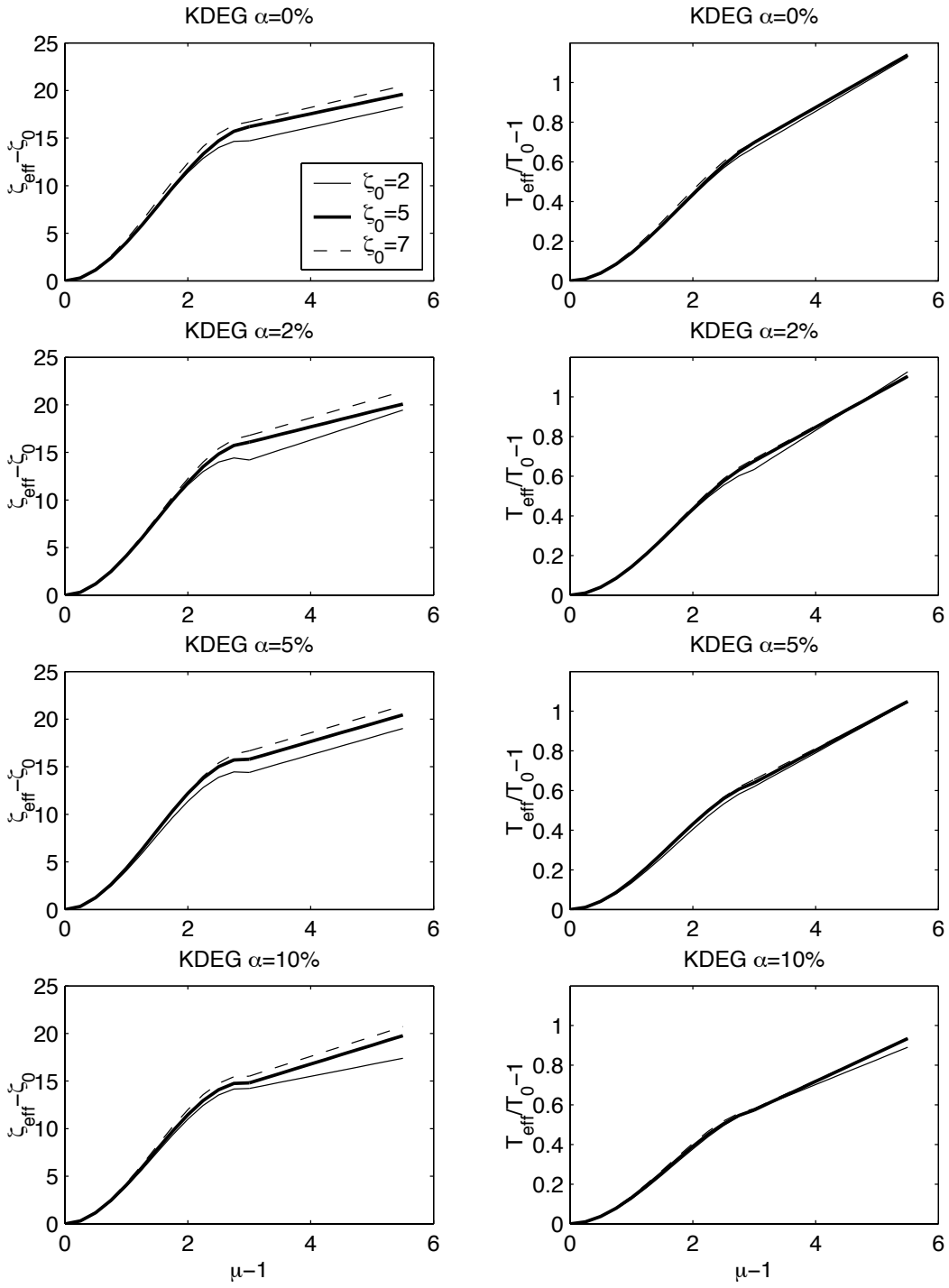

Figure A.4: Effective parameters for stiffness degrading model (KDEG) with $\zeta_0 = 2\%$, 5% and 7% and second slope ratios as indicated - far-field motions

Appendix B

Displacement Response Error Results

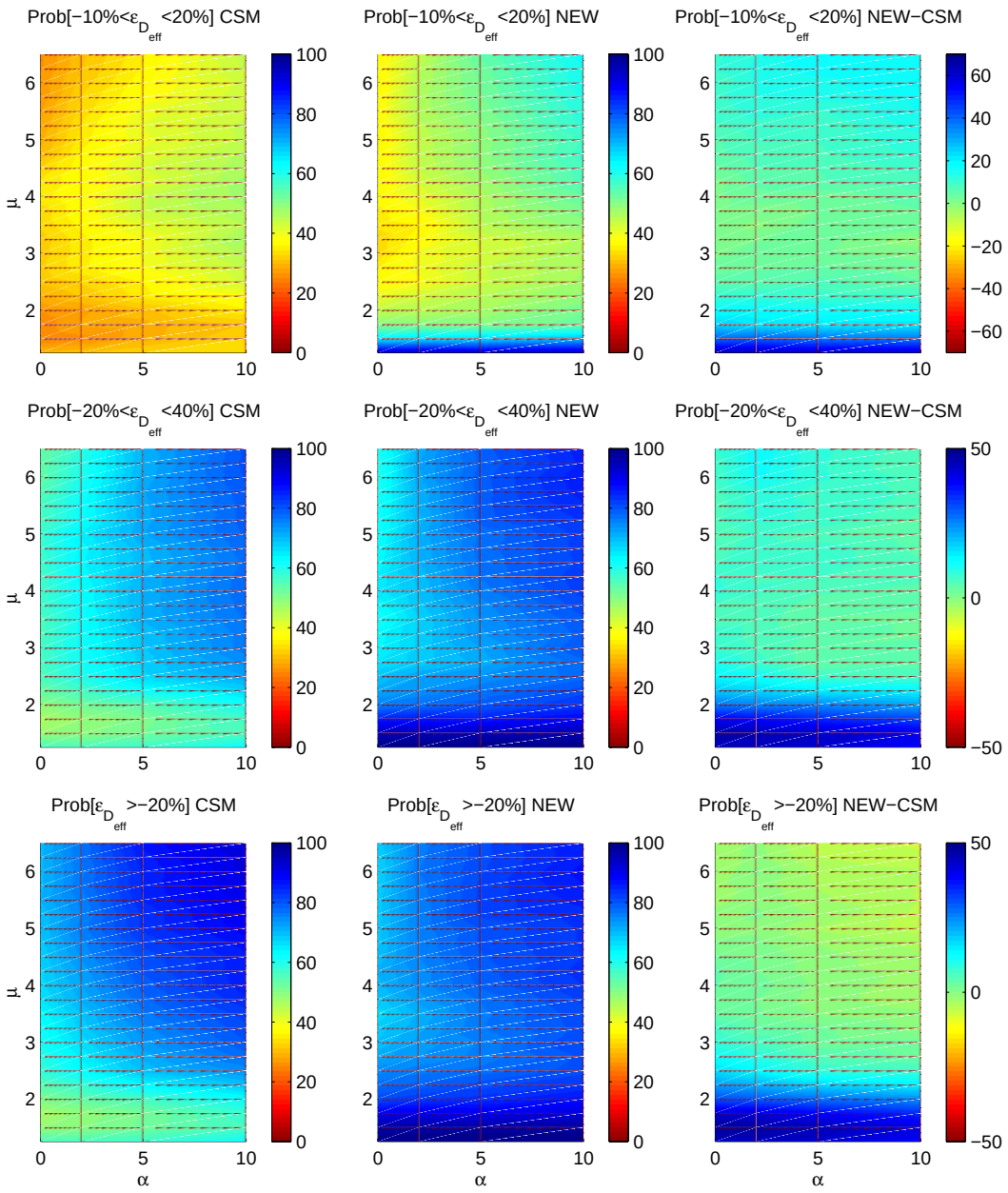

Figure B.1: Displacement Response Error results for bilinear hysteretic system (BLH) - far-field motions. CSM - conventional Capacity Spectrum Method, Structural Behavior Type B (ATC-40). NEW - new approach implemented in this study. Second slope ratios, α, as indicated

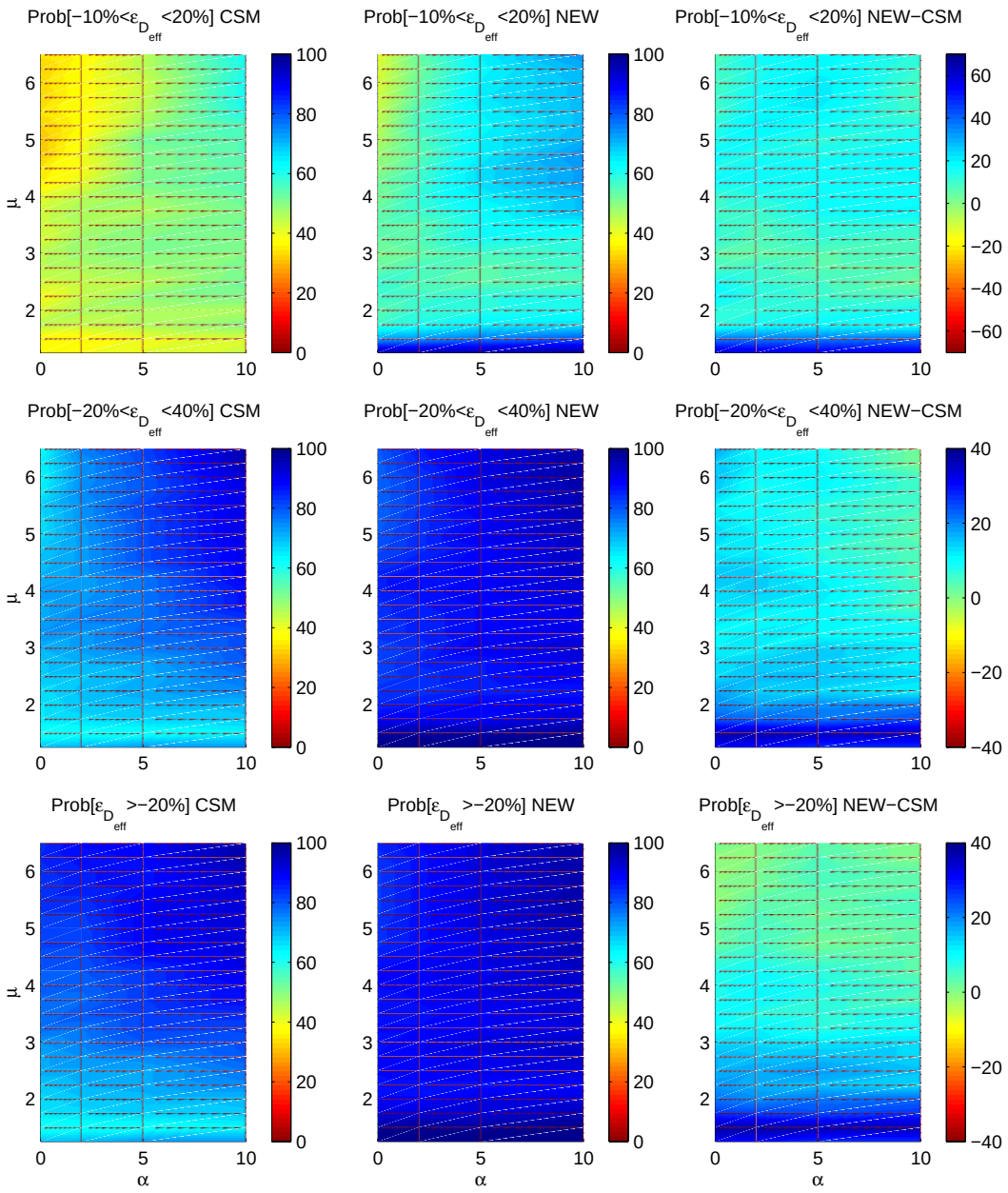

Figure B.2: Displacement Response Error results for bilinear hysteretic system (BLH) - near-field motions with $T_o/T_p \leq 0.7$. CSM - conventional Capacity Spectrum Method, Structural Behavior Type A (ATC-40). NEW - new approach implemented in this study. Second slope ratios, α, as indicated

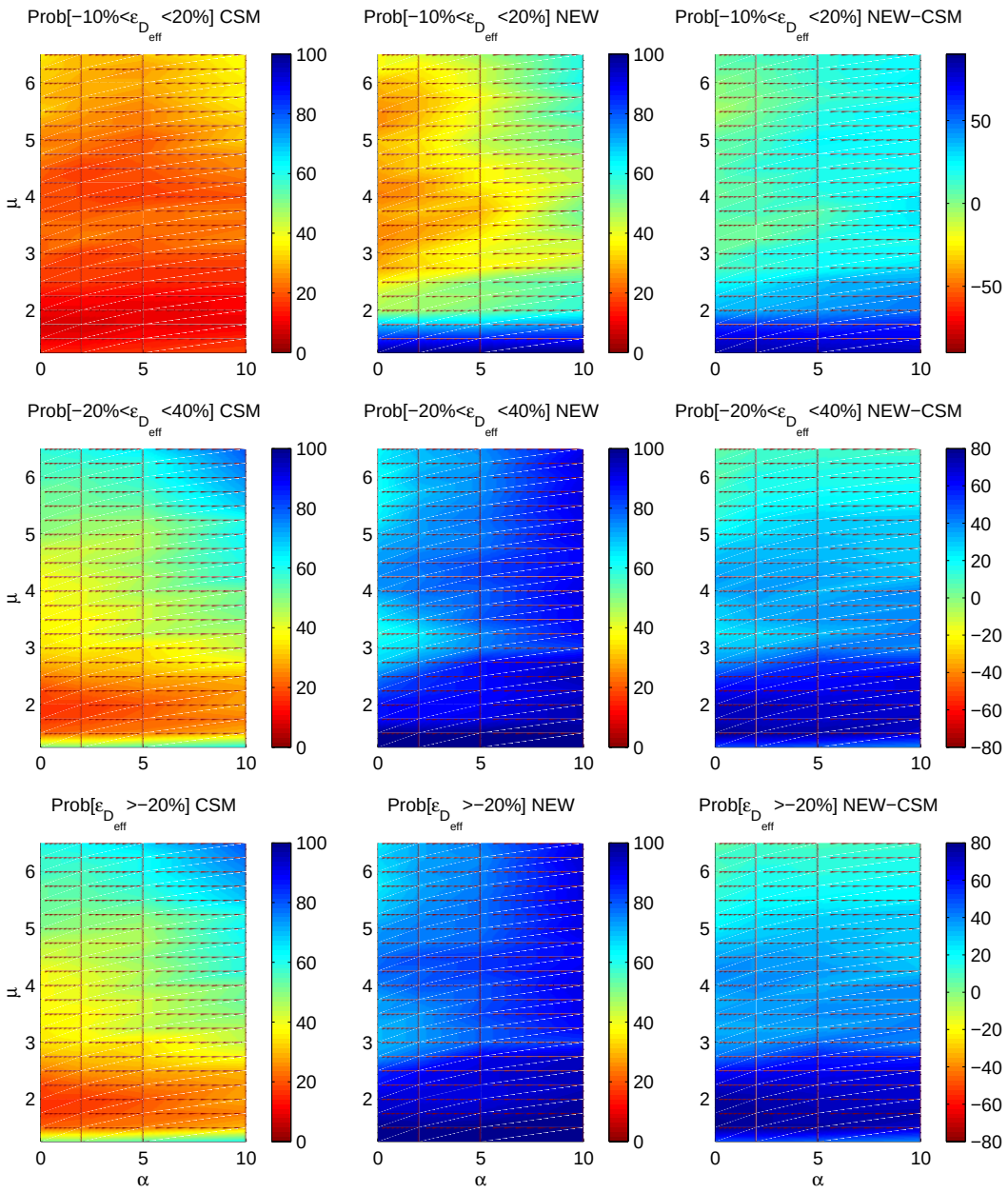

Figure B.3: Displacement Response Error results for bilinear hysteretic system (BLH) - near-field motions with $0.8 \leq T_o/T_p \leq 1.2$. CSM - conventional Capacity Spectrum Method, Structural Behavior Type A (ATC-40). NEW - new approach implemented in this study. Second slope ratios, α, as indicated

Appendix C

Performance Point Error Results

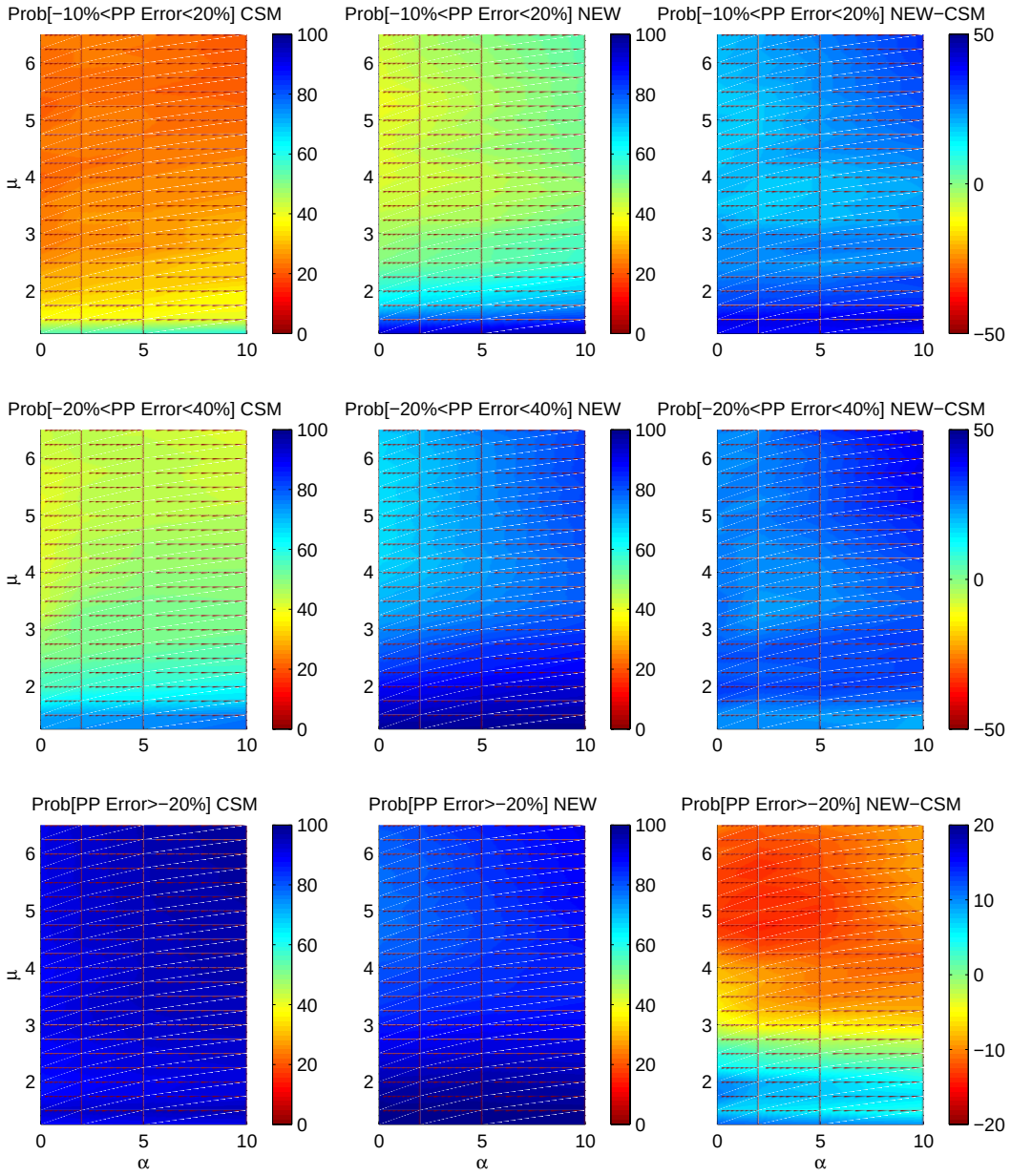

Figure C.1: Performance Point Error results for stiffness degrading system (KDEG) - far-field motions. Conv. CSM - conventional Capacity Spectrum Method, Structural Behavior Type C (ATC-40). New Appr. - new approach implemented in this study. Second slope ratios, α, as indicated

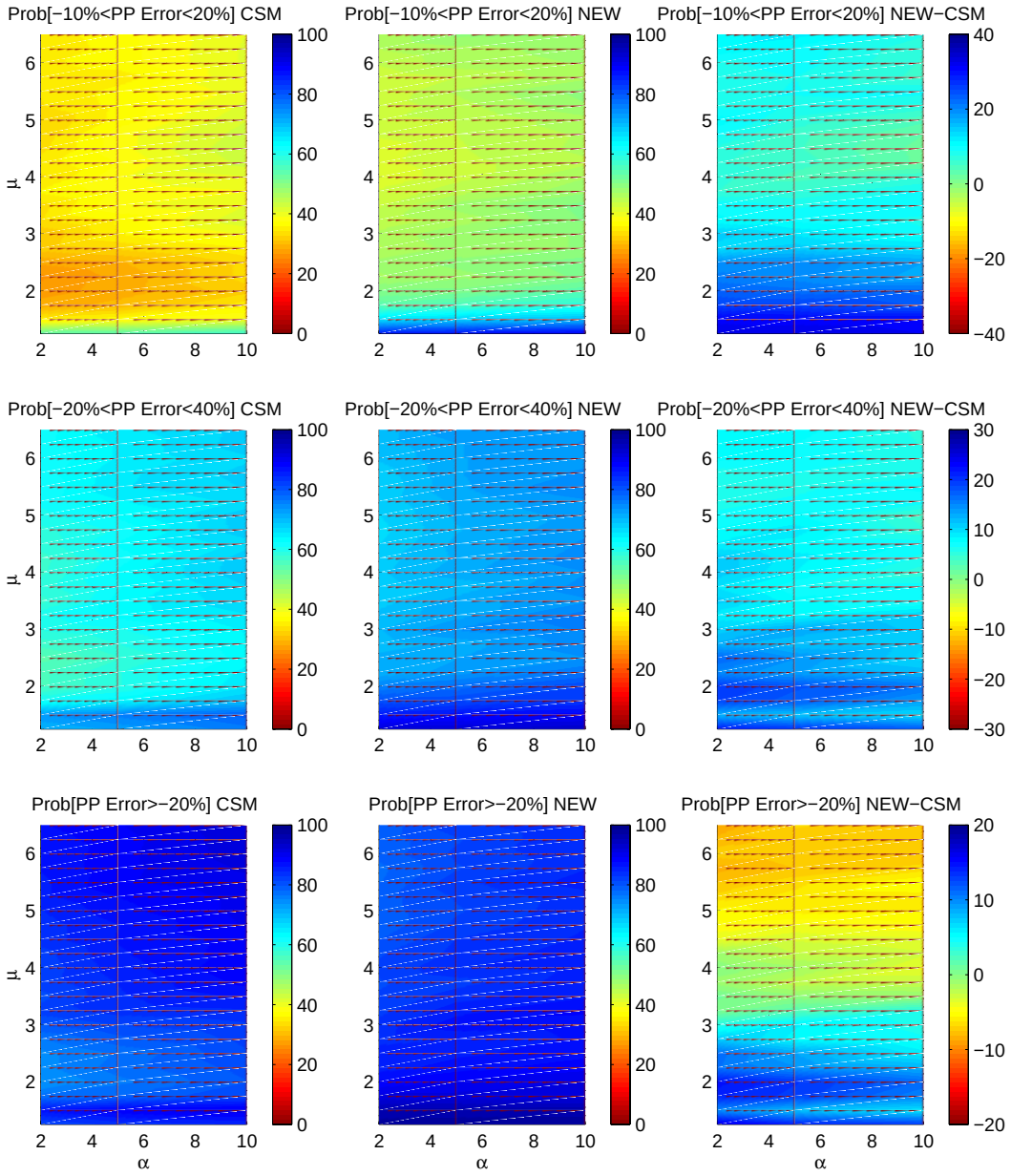

Figure C.2: Performance Point Error results for pinching hysteretic model (PIN1) - far-field motions. Conv. CSM - conventional Capacity Spectrum Method, Structural Behavior Type C (ATC-40). New Appr. - new approach implemented in this study. Second slope ratios, α, as indicated

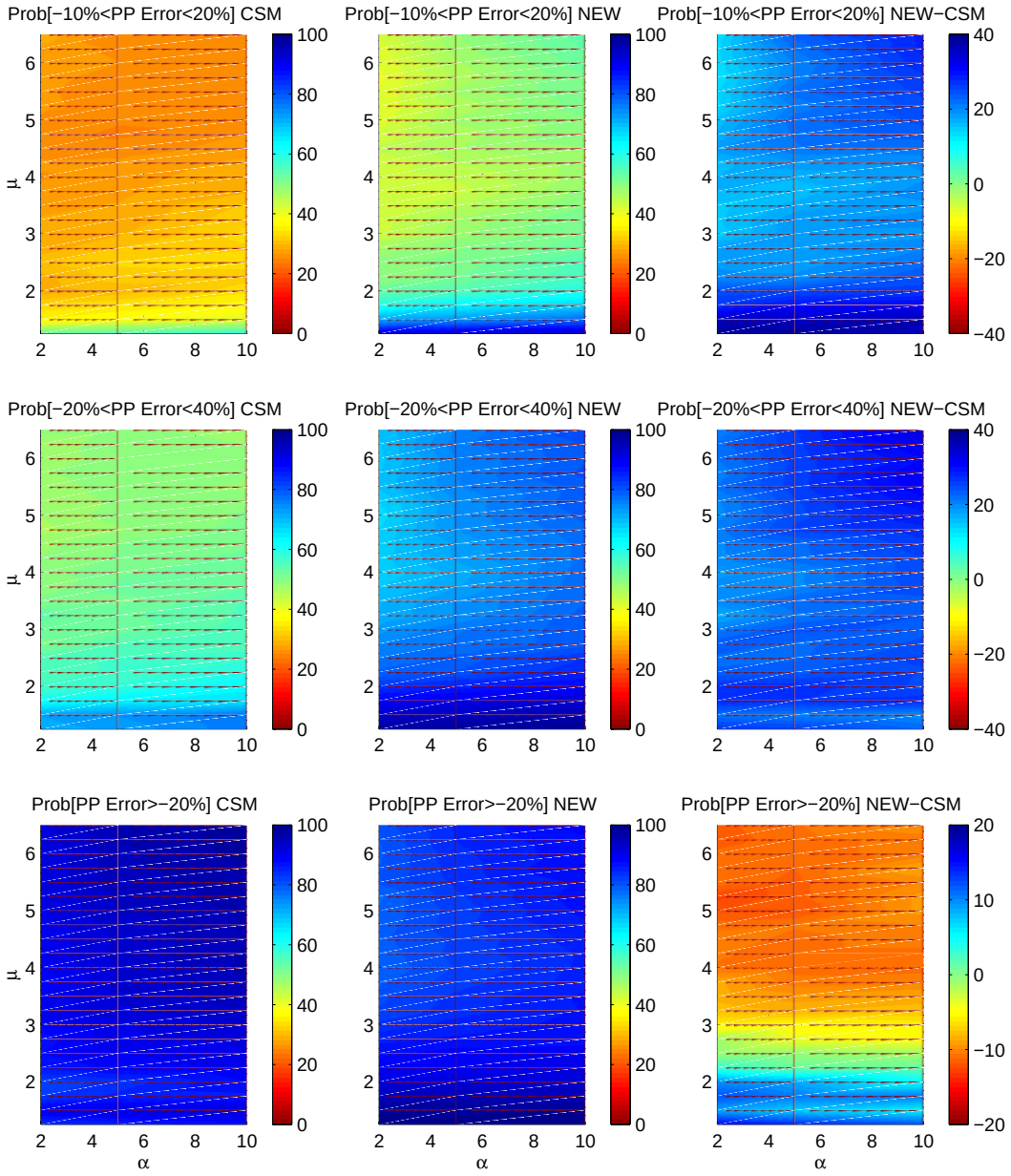

Figure C.3: Performance Point Error results for pinching hysteretic model (PIN2) - far-field motions. Conv. CSM - conventional Capacity Spectrum Method, Structural Behavior Type C (ATC-40). New Appr. - new approach implemented in this study. Second slope ratios, α, as indicated

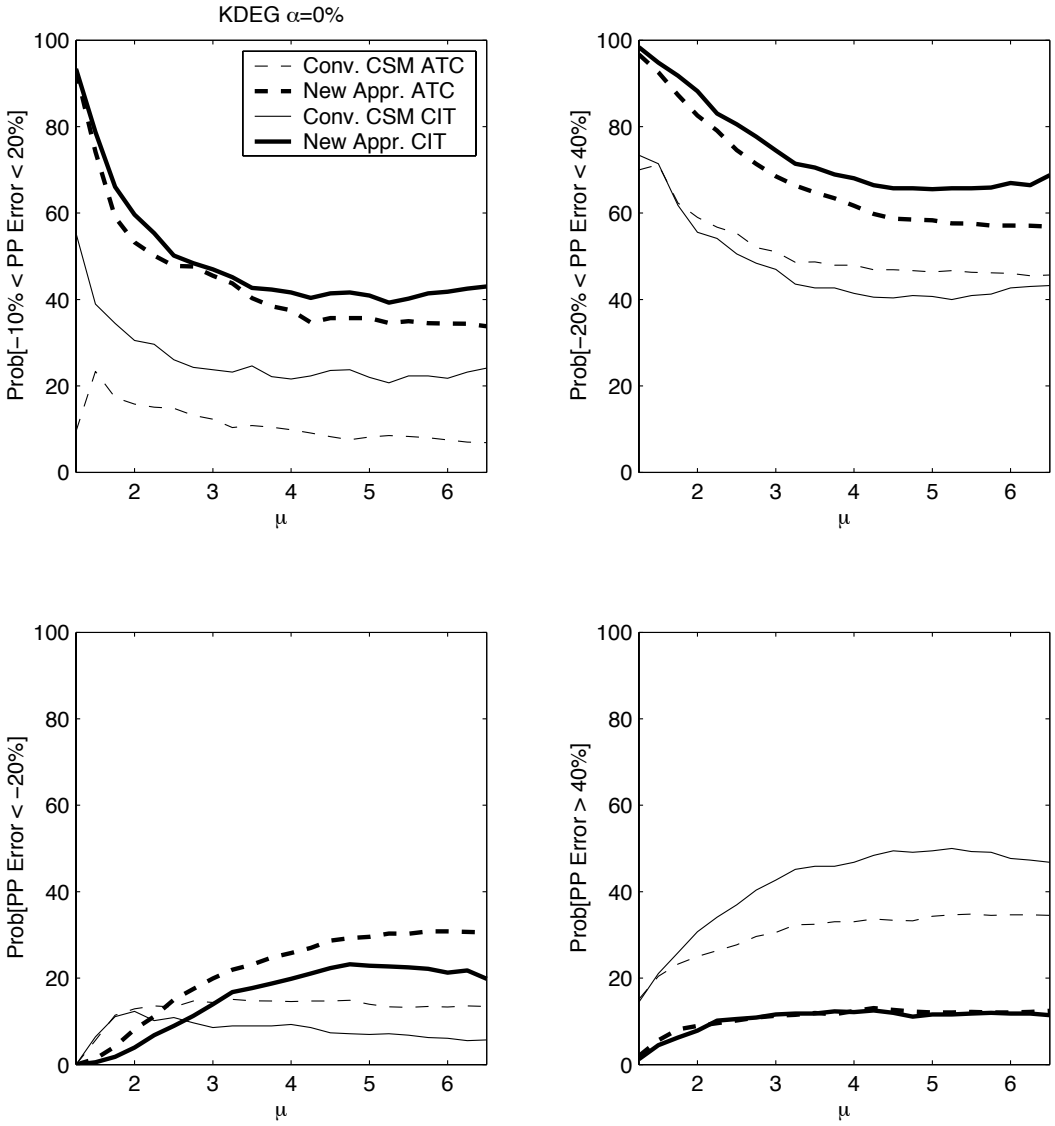

Figure C.4: Performance Point Error results for stiffness degrading model (KDEG) with second slope ratio of 0% - two far-field ground motion databases

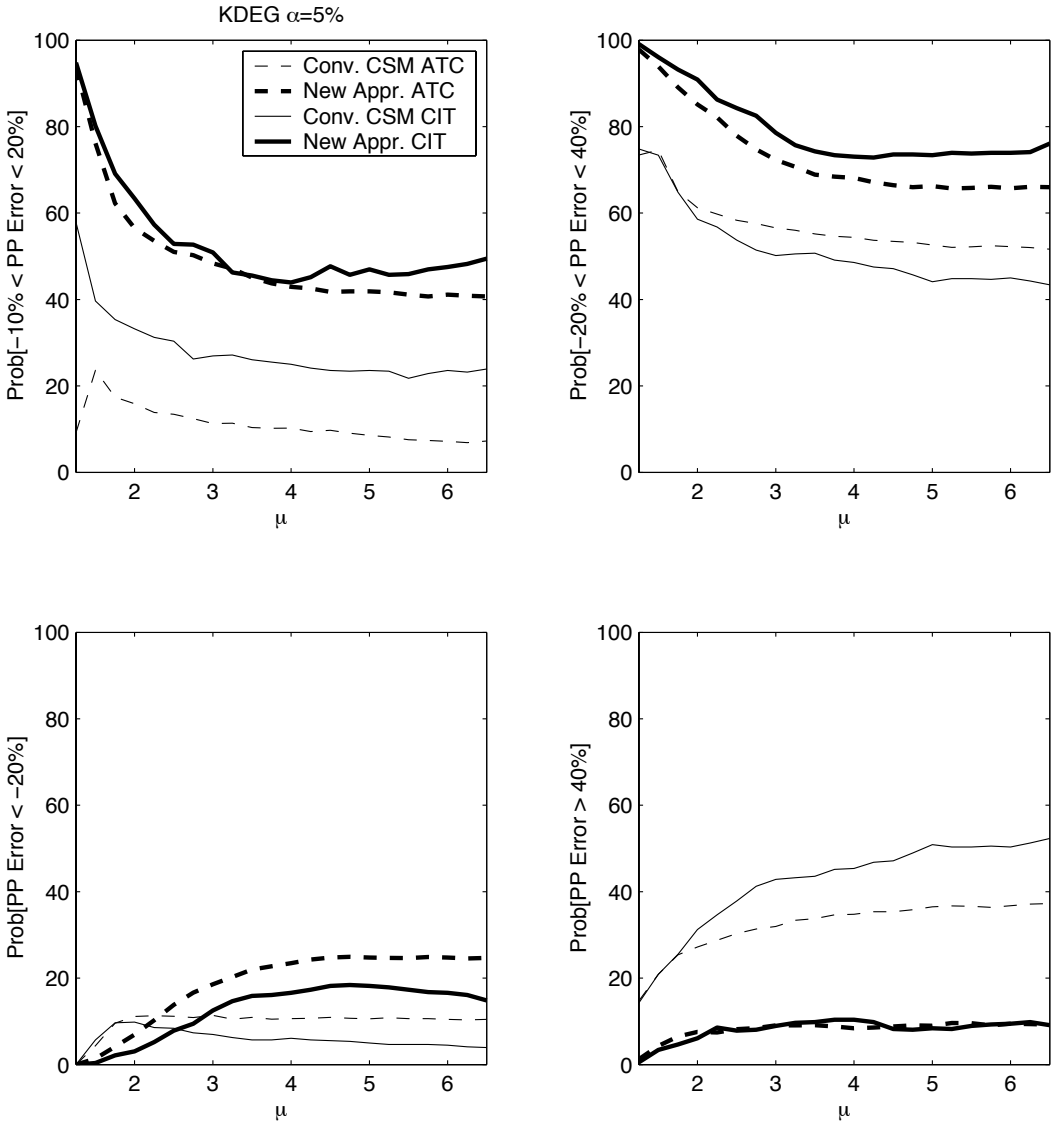

Figure C.5: Performance Point Error results for stiffness degrading model (KDEG) with second slope ratio of 5% - two far-field ground motion databases

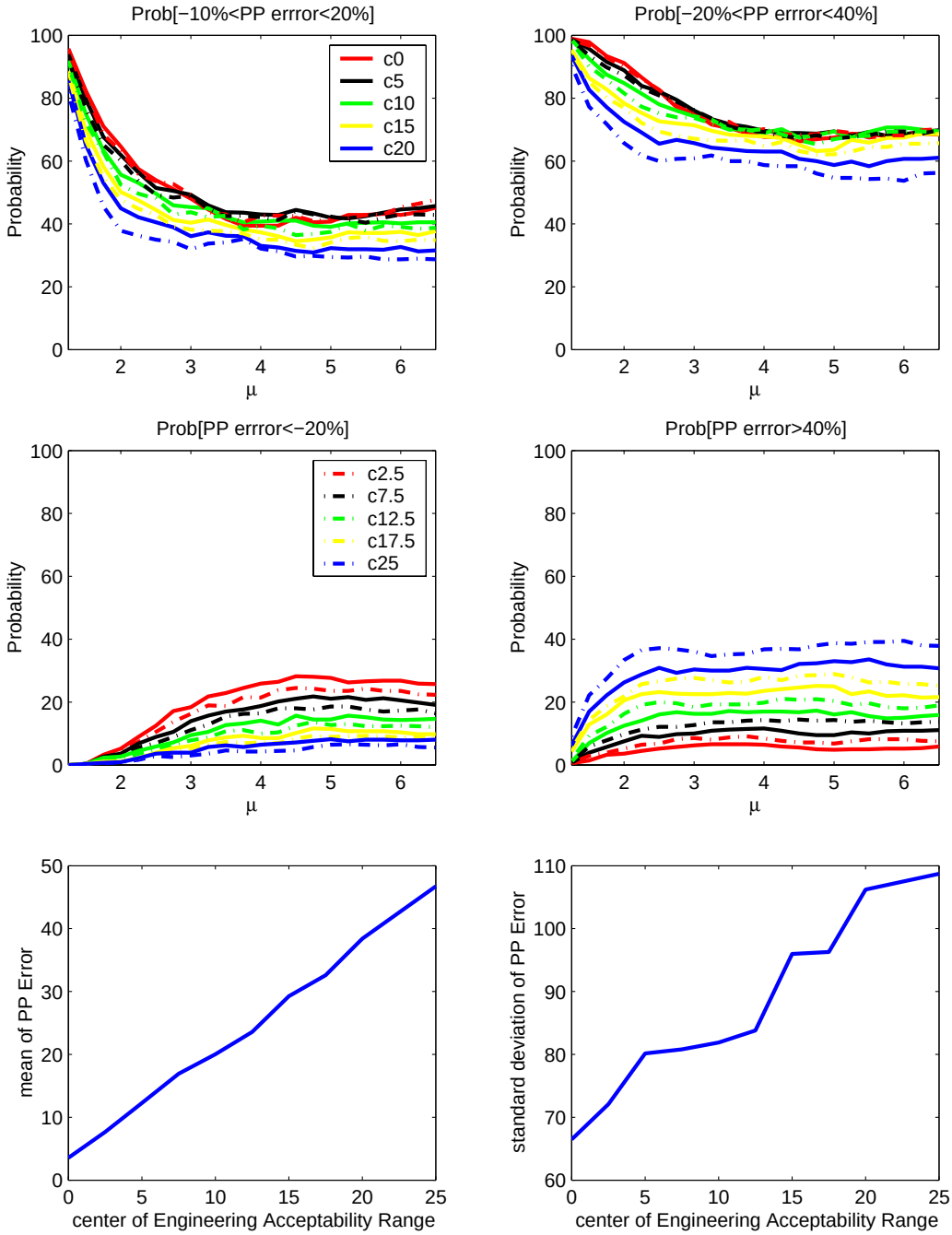

Figure C.6: Sensitivity of Performance Point Error results to changes in Engineering Acceptability Range for stiffness degrading model (KDEG) with second slope ratio of 2% - far-field motions

Appendix D

Tabular Form of Displacement Response Error and Performance Point Error Results

Model - BLH			$\epsilon_{D_{eff}}$		$\epsilon_{D_{pp}}$			
Eqn.	T_o/T_p	α	**mean**	**STD**	**mean**	**STD**	**N/C**	**mult**
NEW	< 0.7	0%	-0.46	19.14	11.10	58.72	0.14	4.92
CSMstrA	< 0.7	0%	1.76	27.39	62.25	208.72	9.23	1.35
NEW	$0.8 - 1.2$	0%	-1.52	23.53	-1.39	22.51	0.00	0.06
CSMstrA	$0.8 - 1.2$	0%	-23.61	21.61	-22.95	23.32	2.47	0.00
NEW	< 0.7	2%	0.19	17.70	9.69	49.85	0.23	3.53
CSMstrA	< 0.7	2%	0.58	24.48	57.49	150.03	2.32	0.28
NEW	$0.8 - 1.2$	2%	-0.84	21.75	-0.78	20.67	0.00	0.00
CSMstrA	$0.8 - 1.2$	2%	-23.03	20.07	-22.15	20.98	2.21	0.00
NEW	< 0.7	5%	0.71	16.20	8.61	42.64	0.14	2.78
CSMstrA	< 0.7	5%	0.19	21.63	28.76	78.21	2.13	0.14
NEW	$0.8 - 1.2$	5%	-0.12	19.40	-0.06	18.30	0.00	0.00
CSMstrA	$0.8 - 1.2$	5%	-21.21	18.51	-20.29	18.90	1.95	0.00
NEW	< 0.7	10%	1.64	14.67	9.54	40.13	0.05	2.41
CSMstrA	< 0.7	10%	0.28	18.44	16.42	49.87	1.99	0.05
NEW	$0.8 - 1.2$	10%	1.14	16.19	1.12	15.69	0.00	0.00
CSMstrA	$0.8 - 1.2$	10%	-18.19	16.02	-17.13	16.90	1.62	0.00

Table D.1: Summary (in %) of Displacement Response Error ($\epsilon_{D_{eff}}$) and Performance Point Error ($\epsilon_{D_{PP}}$) over the entire range of ductilities ($1.25 : 0.25 : 6.5$) for bilinear model (BLH) - near-field ground motions, CSMstrA - conventional Capacity Spectrum Method for Structural Behavior Type A (strA) indicated. NEW - new approach implemented in this study. N/C - Non-convergent cases. mult - multiple solutions

Model - KDEG			$\epsilon_{D_{eff}}$		$\epsilon_{D_{pp}}$			
Eqn.	T_o/T_p	α	**mean**	**STD**	**mean**	**STD**	**N/C**	**mult**
NEW	< 0.7	0%	1.05	14.60	50.22	170.57	0.0	12.11
CSMstrB	< 0.7	0%	13.03	25.43	93.76	209.49	9.28	2.50
CSMstrC	< 0.7	0%	33.14	30.41	156.17	226.93	9.55	4.22
NEW	$0.8 - 1.2$	0%	1.46	15.98	1.47	15.48	0.0	0.06
CSMstrB	$0.8 - 1.2$	0%	-12.18	17.48	-11.21	18.15	0.91	0.00
CSMstrC	$0.8 - 1.2$	0%	3.04	20.21	5.96	22.60	0.13	0.19
NEW	< 0.7	2%	1.19	14.13	41.42	144.35	0.09	11.69
CSMstrB	< 0.7	2%	10.82	23.02	98.33	216.08	2.41	1.16
CSMstrC	< 0.7	2%	30.67	27.63	146.90	256.24	5.57	2.97
NEW	$0.8 - 1.2$	2%	1.69	15.15	1.76	14.90	0.0	0.06
CSMstrB	$0.8 - 1.2$	2%	-12.31	16.64	-11.23	17.02	0.71	0.00
CSMstrC	$0.8 - 1.2$	2%	3.36	19.45	5.91	21.50	0.13	0.00
NEW	< 0.7	5%	1.38	13.46	33.00	126.48	0.09	9.32
CSMstrB	< 0.7	5%	9.05	20.48	55.12	99.29	0.79	0.56
CSMstrC	< 0.7	5%	29.51	25.22	132.03	183.53	0.88	2.55
NEW	$0.8 - 1.2$	5%	1.87	14.17	1.96	14.00	0.0	0.06
CSMstrB	$0.8 - 1.2$	5%	-11.78	15.66	-10.55	16.15	0.58	0.00
CSMstrC	$0.8 - 1.2$	5%	5.15	19.02	7.82	21.73	0.13	0.00
NEW	< 0.7	10%	1.82	12.59	17.76	69.92	0.37	7.10
CSMstrB	< 0.7	10%	7.61	17.74	33.90	60.71	0.70	0.19
CSMstrC	< 0.7	10%	28.40	22.75	91.33	106.00	0.14	1.48
NEW	$0.8 - 1.2$	10%	2.00	12.90	2.17	12.91	0.0	0.06
CSMstrB	$0.8 - 1.2$	10%	-9.90	14.83	-8.46	16.01	0.58	0.00
CSMstrC	$0.8 - 1.2$	10%	8.47	19.01	11.82	23.30	0.13	0.13

Table D.2: Summary (in %) of Displacement Response Error ($\epsilon_{D_{eff}}$) and Performance Point Error ($\epsilon_{D_{PP}}$) over the entire range of ductilities ($1.25 : 0.25 : 6.5$) for stiffness degrading model (KDEG) **-** near-field ground motions. CSMstrB/C **-** conventional Capacity Spectrum Method for Structural Behavior Type (str) indicated. NEW **-** new approach implemented in this study. N/C **-** Non-convergent cases. mult **-** multiple solutions

Model	**Eqn.**	α	$\epsilon_{D_{pp}}$ **Range**	$\mu =$ **1.25-3.0**	$\mu =$ **3.25-5.0**	$\mu =$ **5.25-6.5**
BLH	NEW	0%	-10% to 20%	46.05	34.57	24.66
BLH	CSMstrA	0%	-10% to 20%	19.39	16.45	18.03
BLH	NEW	5%	-10% to 20%	49.62	43.62	42.69
BLH	CSMstrA	5%	-10% to 20%	22.96	23.21	22.45
KDEG	NEW	0%	-10% to 20%	47.96	27.17	30.61
KDEG	CSMstrB	0%	-10% to 20%	27.17	13.27	19.56
KDEG	CSMstrC	0%	-10% to 20%	21.56	13.52	15.31
KDEG	NEW	5%	-10% to 20%	51.66	32.53	33.84
KDEG	CSMstrB	5%	-10% to 20%	27.68	21.81	27.55
KDEG	CSMstrC	5%	-10% to 20%	23.34	17.98	17.69
BLH	NEW	0%	-20% to 40%	70.15	58.16	43.37
BLH	CSMstrA	0%	-20% to 40%	36.61	31.51	34.18
BLH	NEW	5%	-20% to 40%	73.98	66.96	62.76
BLH	CSMstrA	5%	-20% to 40%	45.15	41.33	48.81
KDEG	NEW	0%	-20% to 40%	75.26	58.04	56.80
KDEG	CSMstrB	0%	-20% to 40%	58.04	30.10	36.39
KDEG	CSMstrC	0%	-20% to 40%	34.69	27.30	26.19
KDEG	NEW	5%	-20% to 40%	78.44	65.82	64.29
KDEG	CSMstrB	5%	-20% to 40%	49.87	41.58	52.89
KDEG	CSMstrC	5%	-20% to 40%	37.50	31.89	30.61

Table D.3: Summary (in %) of Displacement Response Error ($\epsilon_{D_{eff}}$) and Performance Point Error ($\epsilon_{D_{PP}}$) over three separate ductility ranges for BLH and KDEG **-** near-field motions with $T_o/T_p \leq 0.7$. CSMstrA/B/C **-** conventional Capacity Spectrum Method for Structural Behavior Type (str) indicated. NEW **-** new approach implemented in this study

Model	**Eqn.**	α	$\epsilon_{D_{pp}}$ **Range**	$\mu =$ **1.25-3.0**	$\mu =$ **3.25-5.0**	$\mu =$ **5.25-6.5**
BLH	NEW	0%	$\leq -20\%$	14.29	25.00	35.88
BLH	CSMstrA	0%	$\leq -20\%$	34.18	30.61	26.36
BLH	NEW	5%	$\leq -20\%$	12.12	18.62	23.64
BLH	CSMstrA	5%	$\leq -20\%$	30.61	26.40	19.05
KDEG	NEW	0%	$\leq -20\%$	7.27	16.84	16.33
KDEG	CSMstrB	0%	$\leq -20\%$	16.84	14.80	9.35
KDEG	CSMstrC	0%	$\leq -20\%$	3.57	0.13	0.17
KDEG	NEW	5%	$\leq -20\%$	7.27	13.65	14.29
KDEG	CSMstrB	5%	$\leq -20\%$	16.71	12.24	4.25
KDEG	CSMstrC	5%	$\leq -20\%$	3.44	0.00	0.00
BLH	NEW	0%	$\geq 40\%$	15.18	16.84	20.75
BLH	CSMstrA	0%	$\geq 40\%$	18.75	30.87	28.91
BLH	NEW	5%	$\geq 40\%$	13.56	14.41	13.44
BLH	CSMstrA	5%	$\geq 40\%$	18.75	32.14	31.80
KDEG	NEW	0%	$\geq 40\%$	17.47	27.13	26.87
KDEG	CSMstrB	0%	$\geq 40\%$	25.13	45.66	43.37
KDEG	CSMstrC	0%	$\geq 40\%$	54.21	62.24	62.42
KDEG	NEW	5%	$\geq 40\%$	14.03	20.54	21.43
KDEG	CSMstrB	5%	$\geq 40\%$	31.38	46.05	42.86
KDEG	CSMstrC	5%	$\geq 40\%$	58.67	67.35	67.69

Table D.4: Summary (in %) of Displacement Response Error ($\epsilon_{D_{eff}}$) and Performance Point Error ($\epsilon_{D_{PP}}$) over three separate ductility ranges for BLH and KDEG - near-field motions with $T_o/T_p \leq 0.7$. CSMstrA/B/C - conventional Capacity Spectrum Method for Structural Behavior Type (str) indicated. NEW - new approach implemented in this study

Model	**Eqn.**	α	$\epsilon_{D_{pp}}$ **Range**	$\mu =$ **1.25-3.0**	$\mu =$ **3.25-5.0**	$\mu =$ **5.25-6.5**
BLH	NEW	0%	-10% to 20%	58.93	28.39	30.95
BLH	CSMstrA	0%	-10% to 20%	13.75	18.75	21.19
BLH	NEW	5%	-10% to 20%	64.64	40.18	46.90
BLH	CSMstrA	5%	-10% to 20%	13.75	18.57	23.57
KDEG	NEW	0%	-10% to 20%	71.25	52.14	52.86
KDEG	CSMstrB	0%	-10% to 20%	26.61	34.82	48.81
KDEG	CSMstrC	0%	-10% to 20%	52.50	50.89	54.29
KDEG	NEW	5%	-10% to 20%	74.64	61.07	67.38
KDEG	CSMstrB	5%	-10% to 20%	28.04	39.64	50.00
KDEG	CSMstrC	5%	-10% to 20%	57.50	55.18	57.14
BLH	NEW	0%	-20% to 40%	89.28	69.46	68.57
BLH	CSMstrA	0%	-20% to 40%	31.07	34.64	45.00
BLH	NEW	5%	-20% to 40%	94.28	80.00	75.00
BLH	CSMstrA	5%	-20% to 40%	35.89	38.93	47.14
KDEG	NEW	0%	-20% to 40%	97.68	91.96	90.95
KDEG	CSMstrB	0%	-20% to 40%	54.82	58.39	73.81
KDEG	CSMstrC	0%	-20% to 40%	86.25	79.64	80.95
KDEG	NEW	5%	-20% to 40%	98.39	93.75	95.00
KDEG	CSMstrB	5%	-20% to 40%	60.36	65.18	78.57
KDEG	CSMstrC	5%	-20% to 40%	88.75	88.04	81.67

Table D.5: Summary (in %) of Displacement Response Error ($\epsilon_{D_{eff}}$) and Performance Point Error ($\epsilon_{D_{PP}}$) over three separate ductility ranges for BLH and KDEG - near-field motions with $0.8 \leq T_o/T_p \leq 1.2$. CSMstrA/B/C - conventional Capacity Spectrum Method for Structural Behavior Type (str) indicated. NEW - new approach implemented in this study

Model	**Eqn.**	α	$\epsilon_{D_{pp}}$ **Range**	$\mu =$ **1.25-3.0**	$\mu =$ **3.25-5.0**	$\mu =$ **5.25-6.5**
BLH	NEW	0%	$\leq -20\%$	7.86	25.89	29.52
BLH	CSMstrA	0%	$\leq -20\%$	62.32	63.57	51.67
BLH	NEW	5%	$\leq -20\%$	3.39	18.21	22.62
BLH	CSMstrA	5%	$\leq -20\%$	58.75	59.82	50.00
KDEG	NEW	0%	$\leq -20\%$	1.07	7.86	9.05
KDEG	CSMstrB	0%	$\leq -20\%$	42.32	39.64	23.81
KDEG	CSMstrC	0%	$\leq -20\%$	8.39	12.32	6.67
KDEG	NEW	5%	$\leq -20\%$	0.54	5.54	4.52
KDEG	CSMstrB	5%	$\leq -20\%$	37.68	33.39	19.76
KDEG	CSMstrC	5%	$\leq -20\%$	5.71	3.93	5.00
BLH	NEW	0%	$\geq 40\%$	2.86	4.64	1.90
BLH	CSMstrA	0%	$\geq 40\%$	0.00	1.61	3.33
BLH	NEW	5%	$\geq 40\%$	2.32	1.79	2.38
BLH	CSMstrA	5%	$\geq 40\%$	0.00	1.25	2.86
KDEG	NEW	0%	$\geq 40\%$	1.25	0.18	0.00
KDEG	CSMstrB	0%	$\geq 40\%$	0.36	1.96	2.38
KDEG	CSMstrC	0%	$\geq 40\%$	5.50	8.04	12.38
KDEG	NEW	5%	$\geq 40\%$	1.07	0.71	0.48
KDEG	CSMstrB	5%	$\geq 40\%$	0.36	1.43	1.67
KDEG	CSMstrC	5%	$\geq 40\%$	5.18	8.04	13.33

Table D.6: Summary (in %) of Displacement Response Error ($\epsilon_{D_{eff}}$) and Performance Point Error ($\epsilon_{D_{PP}}$) over three separate ductility ranges for BLH and KDEG - near-field motions with $0.8 \leq T_o/T_p \leq 1.2$. CSMstrA/B/C - conventional Capacity Spectrum Method for Structural Behavior Type (str) indicated. NEW - new approach implemented in this study

Appendix E

Locus of Performance Points from the UBC Spectrum

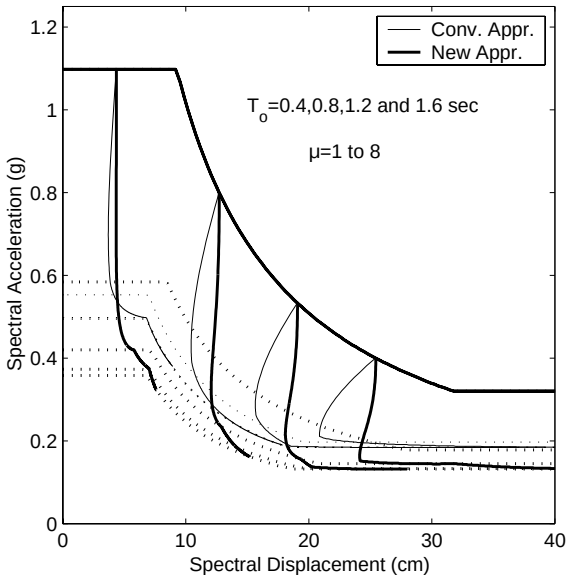

Figure E.1: UBC Locus of Performance Points for bilinear hysteretic system (BLH) with $\alpha = 5\%$ - far-field motions

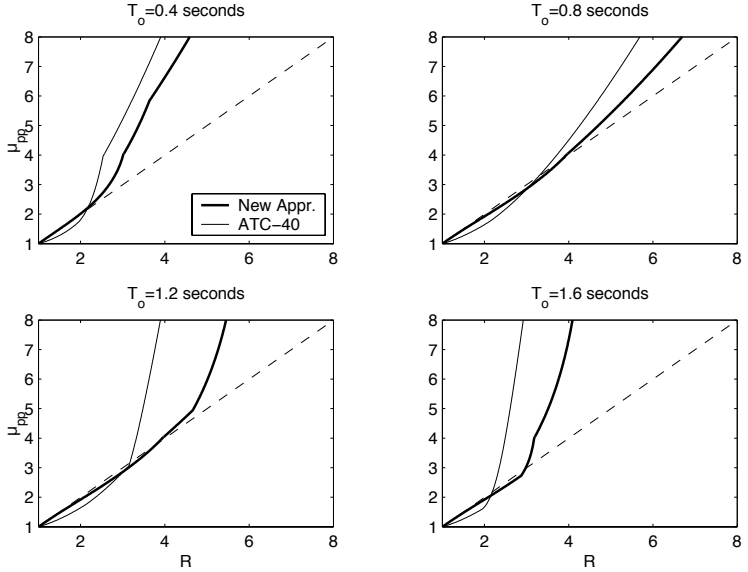

Figure E.2: Strength reduction factor, R, versus Performance Point ductility, μ_{pp}, from Figure E.1

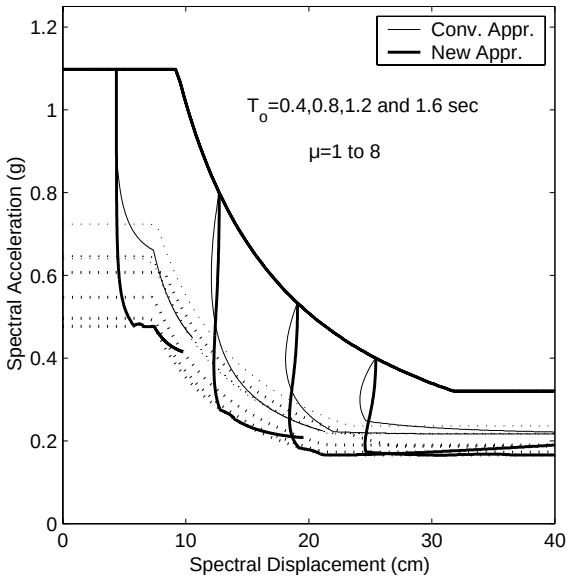

Figure E.3: UBC Locus of Performance Points for stiffness degrading system (KDEG) with $\alpha = 5\%$ - far-field motions

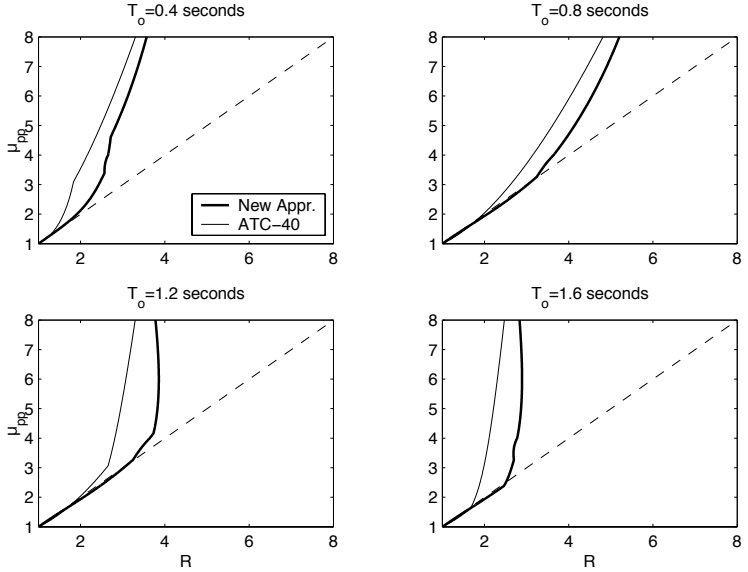

Figure E.4: Strength reduction factor, R, versus Performance Point ductility, μ_{pp}, from Figure E.3

Appendix F

Existing Nonlinear Static Procedures

F.1 Conventional Capacity Spectrum Method

The Capacity Spectrum Method as explained in ATC-40 [19] is summarized below.

1. A building designed on a specific site is obtained. A computer model of the structure is constructed as discussed in Section 1.4.2.2. A push-over analysis is performed on the computer model using the first-mode shape load profile. A load-deflection curve is obtained from the push-over analysis.

2. Convert the push-over curve into a capacity spectrum using the following equations

$$\text{Spectral Acceleration} = \text{Force } \tilde{\mathbf{a}}^T\mathbf{M}\tilde{\mathbf{a}}/(\tilde{\mathbf{a}}^T\mathbf{M}\tilde{\mathbf{I}})^2 \tag{F.1}$$

$$\text{Spectral Displacement} = \text{Displacement } \tilde{\mathbf{a}}^T\mathbf{M}\tilde{\mathbf{a}}/(\tilde{\mathbf{a}}^T\mathbf{M}\tilde{\mathbf{I}}) \tag{F.2}$$

   where $\tilde{\mathbf{a}}$ is the fundamental lateral mode shape, $\mathbf{M}$ is the mass matrix for the horizontal degrees of freedom and $\tilde{\mathbf{I}}$ is the identity vector.

3. Use Table F.1 to determine the Structural Behavior Type (SBT), which is *not independent* of the expected ground motion at the site. Structural Behavior Type depends on both engineering judgment and *shaking duration* expected on the site. Near-fault sites are categorized as short shaking duration while far-field sites are categorized as long shaking duration.

Shaking Duration[1]	**Essentially New Building**[2]	**Average Existing Building**[3]	**Poor Existing Building**[4]
Short	Type A	Type B	Type C
Long	Type B	Type C	Type C

Table F.1: Structural Behavior Type (Table 8-4 in ATC-40)

4. Determine the Seismic Source Type from Table F.2. The Seismic Source Type is a function of the Seismic Source Description and Seismic Source Definition.

Seismic Source Type	**Seismic Source Description**	**Seismic Source Definition**	
		Max Moment Magnitude, M	Slip Rate, SR(mm/yr)
A	Faults that are capable of producing large magnitude events that have a high rate of seismic activity	$M \geq 7.0$	$SR \geq 5$
B	All other faults not in type A or C	NA	NA
C	Faults that are not capable of producing large magnitude events and that have a relatively low rate of seismic activity	$M < 6.5$	$SR < 2$

Table F.2: Seismic Source Type (Table 4-6 in ATC-40)

5. Determine the Soil Profile Type from Table F.3. Formulas for calculating the average shear wave velocity, the Standard Penetration Test (SPT) coefficient $\overline{N}$ and the average undrained shear strength are provided in ATC-40.

6. Determine the Seismic Zone Factor (Z) is determined. $Z = 0.075, 0.15, 0.20, 0.30$ and 0.40 for zones 1, 2A, 2B, 3 and 4, respectively, in accordance with the California Building Code (CBSC 1995).

[1]See section 4.5.2 of ATC-40 for criteria

[2]Buildings whose primary elements make up an essentially new lateral system and little strength or stiffness is contributed by non-complying elements.

[3]Buildings whose primary elements are combinations of existing and new elements, or better than average existing systems.

[4]Buildings whose primary elements make up non-complying lateral force systems with poor or unreliable hysteretic behavior.

Soil Profile Type	**Soil Profile Name and Generic Description**	**Avg Soil Properties for top 100 feet of site**		
		Shear Wave Velocity, $\overline{v}_s$ (ft/sec) [m/s]	SPT, $\overline{N}$ (blows/ft) [or N_{CH} for cohesion-less soil layers]	Undrained Shear Strength, $\overline{s}_u$ (psf)
S_A	Hard Rock	$\overline{v}_s > 5000[1524]$	Not Applicable	
S_B	Rock	$2500[762] < \overline{v}_s \leq 5000[1524]$	Not Applicable	
S_C	Very Dense Soil and Soft Rock	$1200[366] < \overline{v}_s \leq 2500[762]$	$\overline{N} > 50$	$\overline{s}_u > 2000$
S_D	Stiff Soil	$1200[366] < \overline{v}_s \leq 2500[762]$	$15 \leq \overline{N} \leq 50$	$1000 \leq \overline{s}_u \leq 2000$
S_E	Soft Soil	$600[183] < \overline{v}_s \leq 1200[366]$	$\overline{N} < 15$	$\overline{s}_u < 1000$
S_F	Soil Requiring Site-Specific Evaluation			

Table F.3: Soil Profile Type (Table 4-3 in ATC-40)

7. Determine Near-Source Factors from Table F.4.

Seismic Source Type	**Distance to Known Seismic Source**							
	≤ 2 km		5 km		10 km		> 15 km	
	N_A	N_V	N_A	N_V	N_A	N_V	N_A	N_V
A	1.5	2.0	1.2	1.6	1.0	1.2	1.0	1.0
B	1.3	1.6	1.0	1.2	1.0	1.0	1.0	1.0
C	1.0	1.0	1.0	1.0	1.0	1.0	1.0	1.0

Table F.4: Near-Source Factors, N_A and N_V (Table 4-5 in ATC-40)

8. Compute Seismic Coefficients C_A and C_V from Tables F.5 and F.6, respectively. The factor ZEN is the multiplication of the Seismic Zone Factor (Z) and the Near-Source Factors (either N_A or N_V) and the following values for E: 0.5 for the Serviceability Earthquake, 1.0 for the Design Earthquake, 1.25 for the Maximum Earthquake in zone 4 and 1.5 for the Maximum Earthquake in zone 3.

9. Construct the 5% damped Acceleration-Displacement Response Spectrum (ADRS)

Soil Profile Type	**Shaking Intensity, ZEN**					
	$= 0.075$	$= 0.15$	$= 0.20$	$= 0.30$	$= 0.40$	> 0.40
S_B	0.08	0.15	0.20	0.30	0.40	1.0 ZEN
S_C	0.09	0.18	0.24	0.33	0.40	1.0 ZEN
S_D	0.12	0.22	0.28	0.36	0.44	1.1 ZEN
S_E	0.19	0.30	0.34	0.36	0.36	0.9 ZEN
S_F	Site-Specific Geotechnical Investigation Required					

Table F.5: Seismic Coefficient, C_A (Table 4-7 in ATC-40)

Soil Profile Type	**Shaking Intensity, ZEN**					
	$= 0.075$	$= 0.15$	$= 0.20$	$= 0.30$	$= 0.40$	> 0.40
S_B	0.08	0.15	0.20	0.30	0.40	1.0 ZEN
S_C	0.13	0.25	0.32	0.45	0.56	1.4 ZEN
S_D	0.18	0.32	0.40	0.54	0.64	1.6 ZEN
S_E	0.26	0.50	0.64	0.84	0.96	2.4 ZEN
S_F	Site-Specific Geotechnical Investigation Required					

Table F.6: Seismic Coefficient, C_V (Table 4-8 in ATC-40)

as seen in Figure F.1. This is the Design Spectrum for the analysis. This spectrum is adopted from the Uniform Building Code (UBC), so it will be referred to as the UBC Design Spectrum.

10. Using the equal displacement approximation or information from previous iterations, choose a point along the capacity spectrum to be the expected Performance Point. Fit a bilinear curve for the capacity spectrum that ends at the expected Performance Point. The bilinear curve has an initial linear stiffness up to the yield point, then a post-yield stiffness. (d_y, a_y) is the yield point and (d_{pi}, a_{pi}) is the expected Performance Point. Use Equations 1.28 through F.6 to calculate the Spectral Reduction Factors SR_A and SR_V. Apply SR_A and SR_V to the UBC Design Spectrum as seen in Figure F.1 to create a Demand Spectrum associated with a level of ductility where $\mu = d_{pi}/d_y$.

$$\beta_{eff}\ (\%) = \kappa\beta_0 + 5 \tag{F.3}$$

Structural Behavior Type	**Min** SR_A	**Min** SR_V	β_0 (%)	κ
A	0.33	0.50	$\beta_0 < 16.25$	1.0
			$16.25 < \beta_0 < 45$	$1.13 - 0.13(\beta_0/16.25)$
			$\beta_0 > 45$	0.77
B	0.44	0.56	$\beta_0 < 25$	0.67
			$25 < \beta_0 < 45$	$0.845 - 0.175(\beta_0/25)$
			$\beta_0 > 45$	0.53
C	0.56	0.67	any value	0.33

Table F.7: Damping Modification Factor, κ (Table 8-1 and 8-2 in ATC-40)

$$\beta_0 = (\frac{200}{\pi})(\frac{a_y}{a_{pi}} - \frac{d_y}{d_{pi}}) = (\frac{200}{\pi})\frac{(\mu - 1)(1 - \alpha)}{\mu + \mu\alpha(\mu - 1)} \tag{F.4}$$

$$\mathrm{SR}_A = \frac{3.21 - 0.68 \ln(\beta_{eff})}{2.12} \tag{F.5}$$

$$\mathrm{SR}_V = \frac{2.31 - 0.41 \ln(\beta_{eff})}{1.65} \tag{F.6}$$

The corner period T_1 and other important periods are calculated as follows:

$$T_1 = 0.4 C_V / C_A \tag{F.7}$$

$$T_1' = (\frac{\mathrm{SR}_V}{\mathrm{SR}_A})T_1 \tag{F.8}$$

$$T_2 = T_2' = C_V/(0.32 N_V) \tag{F.9}$$

11. The design spectrum and the capacity curve should now intersect. The Performance Point is obtained when the Design Spectrum ductility and the capacity spectrum ductility are within a tolerance of approximately 5 percent. This will be an iterative process.

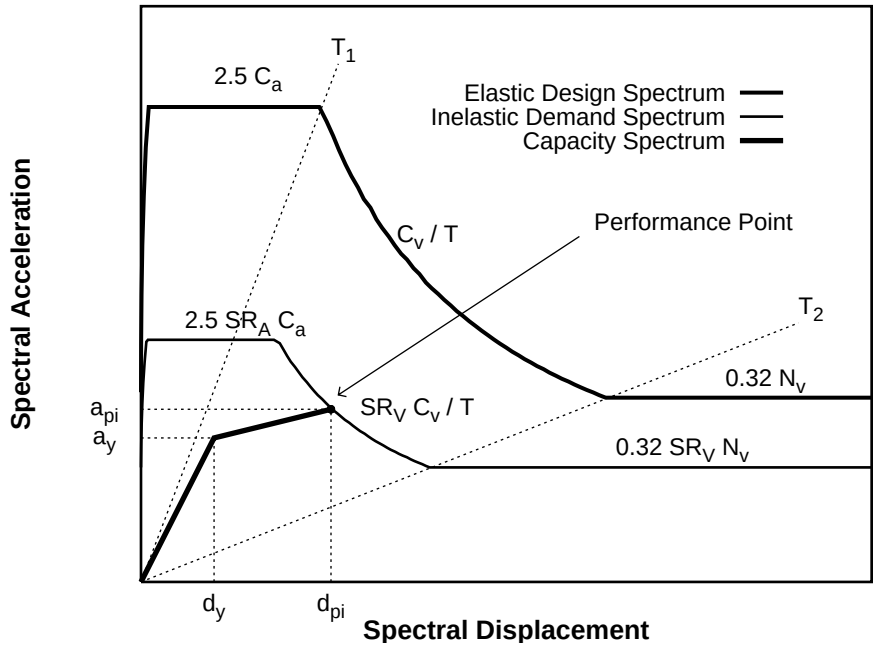

Figure F.1: Illustration of the conventional Capacity Spectrum Method

F.1.1 Observations

The Capacity Spectrum Method is based upon the linear response at the secant period. There is no secant period equation in ATC-40 but the solution procedure uses the secant period as the effective linear period as seen in Figure F.1.

The Capacity Spectrum Method, as presented in ATC-40, is based upon the use of the UBC Design Spectrum. Exchanging a site-specific spectrum in place of the UBC Design Spectrum and using the Spectral Reduction Factors, SR_A and SR_V, is not possible. The factors and the corner periods (T_1, T_1', T_2 and T_2') are designed to work for the UBC spectrum. Discontinuities occur when applied to a non-UBC spectrum.

One can think of the UBC Design Spectrum as consisting of four major parts: the plateau at low periods ($2.5C_A$), radial period line T_1 (T_1'), radial period line T_2 (T_2') and the constant acceleration line at long periods ($0.32N_V$). The C_v/T portion of the curve is guaranteed to fit due to the formulation of these four major parts. However, due to the interconnectedness of the equations for the Demand Spectra, only three

of these four major parts can be specified. In Figure F.1, it is noted that the corner period on the inelastic demand spectrum, T_1', is where the reduction factors SR_A and SR_V are joined. These two factors do not have the same value. The continuity of the reduced UBC spectrum comes from the value of the corner frequency T_1'. Applying the factors SR_A and SR_V to a non-UBC spectrum will result in a discontinuity along the radial line T_1'.

F.2 Coefficient Method

The Coefficient Method as explained in FEMA 273 [2] and FEMA 356 [4] is briefly summarized below.

Coefficients can be used to modify the linear response of a system to predict the inelastic system response. The predicted inelastic system displacement is the Target Displacement. The equation for the Target Displacement, δ_t, in FEMA 273 is

$$\delta_t = C_0 C_1 C_2 C_3 \delta_{elastic} \tag{F.10}$$

where C_0 is the factor relating Spectral Displacement to roof displacement (similar to Equation 1.35 in the Capacity Spectrum Method), C_1 is the factor to relate expected maximum inelastic displacements to displacements calculated for linear elastic response, C_2 is the factor for hysteretic shape and C_3 is the factor for P-$\triangle$ effects. The elastic displacement, $\delta_{elastic}$, is the spectral displacement at the elastic fundamental period of the building, T_e.

$$\delta_{elastic} = \mathrm{SD}(T_e) \tag{F.11}$$

T_e is equivalent to T_o in the current study. This term is equivalent to what will be called T_o in the current study. Spectral Displacement can be related to Pseudo-Spectral Acceleration by

$$\mathrm{SD}(T_e) = \mathrm{PSA}(T_e)\frac{T_e^2}{4\pi^2}g \tag{F.12}$$

Figure F.2 shows an example of the Coefficient Method. The Target Displacement, δ_t,

is directly comparable to the Performance Point in the Capacity Spectrum Method.

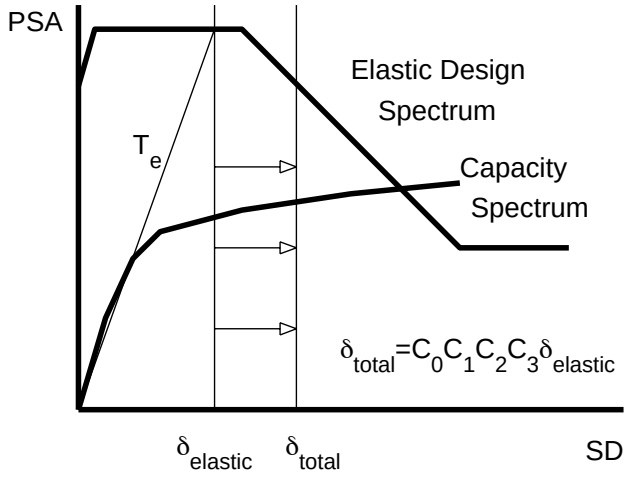

Figure F.2: Illustration of the Coefficient Method

The coefficients used in the coefficient method are functions of several variables. Most notably, the coefficients are functions of the fundamental elastic period of the building, T_e, and a parameter , R, described in FEMA 273 as the ratio of the elastic strength to the calculated yield strength coefficient. The equation for R is as follows

$$R = \frac{\text{PSA}(T_e)}{V_y/W}\frac{1}{C_o} \tag{F.13}$$

where V_y is the yield strength for a bilinear approximation to the capacity curve, W is the weight of the building. This is different from the Capacity Spectrum Method where most coefficients are a function related to ductility. A discussion about ductility versus strength reduction factor is presented in Section 2.6.

F.3 ATC-55 Project

The Applied Technology Council is currently developing the ATC-55 document: *Evaluation and Improvement of Inelastic Seismic Analysis Procedures.* This document will improve upon the current ATC-40 document: *The Seismic Evaluation and Retrofit of Concrete Buildings.* The new optimal effective linear parameters and the new

performance point solution procedure developed in this study have recently been accepted for the improved equivalent linearization procedure in ATC-55. Still to be performed is a comparison of the accuracy of the Capacity Spectrum Method to the Coefficient Method. The project management committee has proposed a procedure for this comparison which will be performed in the coming months. Recommendations about both Nonlinear Static Procedures will be made based upon the results from the comparison.

Appendix G

List of Ground Motions

G.1 Far-field Motions

Orientated to the maximum velocity direction

May 18 1940—Imperial Valley —El Centro —341.69531 —032 47 43N —115 32 55W —032 44 00N —115 27 00W — 6.5— 50— 4—S00E—A001.1 —S90W—A001.2

Jul 21 1952—Kern County —Pasadena-Caltech-Athenaeum —-52.06366 —034 08 20N —118 07 17W —035 00 00N —119 02 00W — 7.2— 50— 4—S00E—A003.1 —S90W—A003.2

Jul 21 1952—Kern County —Taft-Lincoln School Tunnel —175.94533 —035 09 00N—119 27 00W—035 00 00N—119 02 00W— 7.2— 50— 4—N21E—A004.1 —S69E—A004.2

Jul 21 1952—Kern County —Santa Barbara-Court House —128.61136 —034 25 28N—119 42 05W—035 00 00N—119 02 00W— 7.2— 50— 4—N42E—A005.1 —S48E—A005.2

Jul 21 1952—Kern County —Hollywood Storage-Basement —-54.07431 —034 05 00N —118 20 00W —035 00 00N —119 02 00W — 7.2— 50— 4—S00W—A006.1 —N90E—A006.2

Jul 21 1952—Kern County —Hollywood Storage-P.E. Lot —-58.10266 —034 05 00N—118 20 00W—035 00 00N—119 02 00W— 7.2— 50— 4—S00W—A007.1 —N90E—A007.2

Mar 22 1957—San Francisco —Golden Gate Park —-102.80478—037 46 12N—122 28 42W—037 40 00N—122 29 00W— 5.3— 50— 4—N10E—A015.1 —S80E—A015.2

Mar 10 1933—Long Beach —Vernon CMD Building —-151.51968—034 00 00N—118 12 00W—033 35 00N—117 59 00W— 6.4— 50— 4—S08W—B021.1 —N82W—B021.2

Dec 30 1934—Lower California —El Centro-Imperial Valley —-179.14079 —032 47 43N —115 32 55W —032 12 00N —115 30 00W — 7.1— 50— 4—S00W—B024.1 —S90W—B024.2

Oct 31 1935—Helena, Montana —Carrol College —143.46764 —046 35 00N—112 02 00W—046 37 00N—111 58 00W— 5.5— 50— 4—S00W—B025.1 —S90W—B025.2

Apr 13 1949—Western Washington —Seattle-Distr. Engs. Office —66.50983 —047 33 34N—122 20 31W—047 06 00N—122 42 00W— 6.5— 50— 4—S02W—B028.1 —N88W—B028.2

Apr 13 1949—Western Washington —Olympia-Hwy. Test Lab —-274.62964—047 02 00N—122 54 00W—047 06 00N—122 42 00W— 6.5— 50— 4—N04W—B029.1 —N86E—B029.2

Apr 29 1965—Puget Sound —Olympia-Hwy. Test Lab —-194.33553—047 02 00N—122 54 00W—047 24 00N—122 18 00W— 6.4— 50— 4—S04E—B032.1 —S86W—B032.2

Jun 27 1966—Parkfield —Cholame-Shandon Array No. 5 —-425.68188—035 42 00N—120 19 42W—035 54 00N—120 54 00W— 5.8— 50— 4—N05W—B034.1 —N85E—B034.2

Jun 27 1966—Parkfield —Cholame-Shandon Array No. 8 —-269.60083—035 40 18N—120 54 00W—035 54 00N—120 54 00W— 5.8— 50— 4—N50E—B035.1 —N40W—B035.2

Jun 27 1966—Parkfield —Cholame-Shandon Array No. 12 —-63.17204 —035 38 12N—120 24 12W—035 54 00N—120 54 00W— 5.8— 50— 4—N50E—B036.1 —N40W—B036.2

Jun 27 1966—Parkfield —Temblor-California No. 2 —-340.80957—035 45 07N—120 15 52W—035 54 00N—120 54 00W— 5.8— 50— 4—N65W—B037.1 —S25W—B037.2

Feb 09 1971—San Fernando —Pacoima Dam —-1148.0606—034 20 06N—118 23 48W—034 24 00N—118 23 42W—6.3— 50— 4—S16E—C041.1 —S74W—C041.2

Feb 09 1971—San Fernando —8244 Orion Blvd.-1st Floor —-249.95506—034 13 16N—118 28 16W—034 24 00N—118 23 42W— 6.3— 50— 4—N00W—C048.1 —S90W—C048.2

Feb 09 1971—San Fernando —250 E. First St.-Basement —122.73148 —034 03 01N —118 14 26W —034 24 00N —118 23 42W — 6.3— 50— 4—N36E—C051.1 —N54W—C051.2

Feb 09 1971—San Fernando —445 Figueroa St.-Sub Basement —147.09689 —034 03 12N —118 15 24W —034 24 00N —118 23 42W — 6.3— 50— 4—N52W—C054.1 —S38W—C054.2

Feb 09 1971—San Fernando —Hollywood Storage-Basement —148.24088 —034 05 00N —118 20 00W —034 24 00N —118 23 42W — 6.3— 50— 4—S00W—D057.1 —N90E—D057.2

Feb 09 1971—San Fernando —Caltech-Seismological Lab —-188.59351—034 08 55N—118 10 15W—034 24 00N—118 23 42W— 6.3— 50— 4—S00W—G106.1 —S90W—G106.2

Feb 09 1971—San Fernando —Caltech-Athenaeum —-107.25090 —034 08 20N —118 07 17W —034 24 00N —118 23 42W — 6.3— 50— 4—N00E—G107.1 —N90E—G107.2

Feb 09 1971—San Fernando —Caltech, Millikan Lib.-Basement —-197.99080—034 08 12N—118 07 30W—034 24 00N—118 23 42W— 6.3— 50— 4—N00E—G108.1 —N90E—G108.2

Feb 09 1971—San Fernando —Jet Propulsion Lab-Basement —207.76753 —034 12 01N—118 10 25W—034 24 00N—118 23 42W— 6.3— 50— 4—S82E—G110.1 —S08W—G110.2

Feb 09 1971—San Fernando —Palmdale Fire Station —136.24686 —034 34 40N—118 06 45W—034 24 00N—118 23 42W— 6.3— 50— 4—S60E—G114.1 —S30W—G114.2

Feb 09 1971—San Fernando —15250 Ventura Blvd.-Basement —220.57425 —034 09 14N—118 27 50W—034 24 00N—118 23 42W— 6.3— 50— 4—N11E—H115.1 —N79W—H115.2

G.2 Near-field Motions

T_p is the visually estimated velocity pulse period

ARL1 Jan 17 1994—Northridge —Arleta-Fire Station (CDMG)—336.3000 —034 23 60N —118 43 90W —034 21 50N —118 53 80W — 6.7— 50— 4—N90E—ARL.1 ($T_p = 1.0$)

NHL1 Jan 17 1994—Northridge —Newhall-LA County Fire Stn. (CDMG)—-583.7000 —034 38 70N —118 53 00W —034 21 50N —118 53 80W — 6.7— 50— 4—N90E—NHL.1 ($T_p = 0.75$)

PAR1 Jan 17 1994—Northridge —Pardee Station (SCE)—484.70000 —034 44 00N —118 58 00W —034 21 50N —118 53 80W — 6.7— 50— 4—S00E—PAR.1 ($T_p = 1.0$)

SCSE2 Jan 17 1994—Northridge —Sylmar Converter Stn.-East (LADWP)—807.70000 —034 31 20N —118 48 10W —034 21 50N —118 53 80W— 6.7— 50— 4—N72W—SCSE.2 ($T_p = 1.25$)

KOB 1995 Kobe Earthquake (max peak velocity direction) N35W ($T_p = 1.0$)

LUC 1992 Landers Earthquake (max peak velocity direction) N80W ($T_p = 5.0$)

RRS 1994 Northridge Earthquake (max peak velocity direction) S33W ($T_p = 1.25$)

SCH 1994 Northridge Earthquake (max peak velocity direction) S10W ($T_p = 1.5$)

TAK 1995 Kobe Earthquake (max peak velocity direction) N49W ($T_p = 1.75$)

SKR Turkey Earthquake N-S Direction ($T_p = 2.5$)

GBZ Turkey Earthquake Transverse Direction ($T_p = 5.0$)

YPT Turkey Earthquake Longitudinal Direction ($T_p = 4.0$)

T030 Chi-Chi Earthquake E-W Direction ($T_p = 4.0$)

ERZ Erzinchan Earthquake (max peak velocity direction) ($T_p = 2.0$)